UNIVERSIDADE ESTADUAL DE CAMPINAS
FACULDADE DE ENGENHARIA ELÉTRICA E DE COMPUTAÇÃO

Leandro Andrade Couto Fonseca

Application of a Discontinuous Galerkin Method for Waveguide Analysis

Aplicação do Método de Galerkin Descontínuo para a Análise de Guias Fotônicos

Campinas
2018

Leandro Andrade Couto Fonseca

Application of a Discontinuous Galerkin Method for Waveguide Analysis

Aplicação do Método de Galerkin Descontínuo para a Análise de Guias Fotônicos

Dissertation presented to the School of Electrical and Computer Engineering of the University of Campinas in partial fulfillment of the requirements for the Master Degree in Electrical Engineering in the area of Telecommunications and Telematics.

Dissertação apresentada à Faculdade de Engenharia Elétrica e de Computação da Universidade Estadual de Campinas como parte dos requisitos exigidos para a obtenção do título de Mestre em Engenharia Elétrica, na Àrea de Telecomunicações e Telemática.

Supervisor/Orientador: Prof. Dr. Hugo Enrique Hernández Figueroa

Este exemplar corresponde à versão final da dissertação defendida pelo aluno Leandro Andrade Couto Fonseca, e orientada pelo Prof. Dr. Hugo Enrique Hernández Figueroa.

Campinas
2018

Agência(s) de fomento e nº(s) de processo(s): CAPES
ORCID: https://orcid.org/0000-0001-7715-0048

Ficha catalográfica
Universidade Estadual de Campinas
Biblioteca da Área de Engenharia e Arquitetura
Rose Meire da Silva - CRB 8/5974

An24a

Andrade-Fonseca, Leandro, 1990-
Application of a discontinuous Galerkin method for waveguide analysis / Leandro Andrade Couto Fonseca. – Campinas, SP : [s.n.], 2018.

Orientador: Hugo Enrique Hernández Figueroa.
Dissertação (mestrado) – Universidade Estadual de Campinas, Faculdade de Engenharia Elétrica e de Computação.

1. Galerkin, Método de. 2. Ondas Ópticos, Guias. 3. Método dos elementos finitos. 4. Análise modal. 5. Análise de guia de ondas. I. Hernandez-Figueroa, Hugo Enrique, 1959-. II. Universidade Estadual de Campinas. Faculdade de Engenharia Elétrica e de Computação. III. Título.

Informações para Biblioteca Digital

Título em outro idioma: Aplicação do método de Galerkin descontínuo para a análise de guias fotônicos
Palavras-chave em inglês:
Galerkin methods
Optical Waveguides
Finite element method
Modal analysis
Waveguide analysis
Área de concentração: Telecomunicações e Telemática
Titulação: Mestre em Engenharia Elétrica
Banca examinadora:
Hugo Enrique Hernández Figueroa [Orientador]
Ben-Hur Viana Borges
Lucas Heitzmann Gabrielli
Data de defesa: 28-08-2018
Programa de Pós-Graduação: Engenharia Elétrica

Comissão Julgadora – Dissertação de Mestrado

Candidato: Leandro Andrade Couto Fonseca **RA:** 163667

Data da defesa: 28 de agosto de 2018

Título da Tese: "Application of a Discontinuous Galerkin Method for Waveguide Analysis (Aplicação do Método de Galerkin Descontínuo para a Análise de Guias Fotônicos)".

Prof. Dr. Prof. Dr. Hugo Enrique Hernández Figueroa (Presidente, FEEC/UNICAMP)
Prof. Dr. Ben-Hur Viana Borges (SEL-EESC /USP)
Prof. Dr. Lucas Heitzmann Gabrielli (FEEC/UNICAMP)

A ata de defesa, com as respectivas assinaturas dos membros da Comissão Julgadora, encontra-se no SIGA (Sistema de Fluxo de Dissertação/Tese) e na Secretaria de Pós-Graduação da Faculdade de Engenharia Elétrica e de Computação.

Aos meus pais.
Àqueles que se dedicam a um
sistema de ensino público
justo, ético e igualitário.

Acknowledgments

For the sake of comprehension and gratitude I'll try to express myself in other languages here.

Agradeço à minha mãe Maria das Graças Andrade e Fonseca (Dona Dath) que, com sua bondade imensurável, força, cultura, humildade e esperança, tem guiado meu caminho e é minha principal referência. Agradeço ao meu pai César Augusto da Fonseca pelo ensino da humildade e pelo seu exemplo de disciplina. Agradeço ao meu irmão Alessandro pela amizade e pelo exemplo de persistência e dedicação. Agradecimento especial também à Tia Berenice (representando a família de meu pai), à Natália (prima representando a família de minha mãe) e *in memoriam* ao meu avô materno.

Sou imensamente grato ao Prof. Dr. Hugo Enrique Hernández Figueroa pela sábia orientação e suporte na pesquisa de mestrado, e também por ter me incumbido a tarefa de solucionar problemas relevantes e desafiadores. Agradeço também às funcionárias da FEEC, especialmente Noêmia e Camila.

Obrigado também ao Prof. Dr. Elson José da Silva (UFMG) por me introduzir ao eletromagnetismo e aos métodos computacionais associados com amizade e cuidado. E não poderia esquecer de minha primeira orientadora Prof. Dra. Raquel Melo-Minardi, aos antigos chefes que tanto me ensinaram Dr. Adriano Chaves Lisboa, Prof. Dr. Diogo Batista Oliveira e Arnaud Collin. Gratidão aos companheiros de laboratório, representados por Giba, Prof. Leonardo, Dr. Luciano e Adriano. Gratidão especial também a um dos melhores engenheiros que já conheci e que tive a oportunidade de trabalhar, o Msc. Edson César dos Reis (Bradar-Embraer). Um agradecimento especial aos amigos e colegas Julían Pita e Maicon, pelo longo e intenso trabalho e por tantos códigos interessantes que temos feito juntos. Com vocês dois meu interesse por fotônica cresceu muito.

Fora da esfera profissional eu tive a sorte de encontrar amigos com quem compartilhei momentos de alegria pura. Eu acredito que vocês sabem o quão bem me sinto perto de vocês. Minha gratidão por vocês é imensa: 'Só Alegria!'. Destaco aqui aqueles que estiveram mais próximos de mim neste período de mestrado: a incrível/especial/rosiana namorada Lila Marx Nunes; os surreais Lê Cunha & Dan Piaia, Lucas Maia, Jana Tatim, Jordi Morera; o mais legal Pedrosa Rosário; o *tovarishch* Thales Venâncio Borges; a querida e forte Isabela Castro; os iluminados Leo Barbarosa & Lu Munk; os queridíssimxs e absolutamente massas Budamigos (em especial o Gabriel); às amigas da FEEC Yalena e Ruby; o velho amigo Rayner Bastos; os grandes amigos de 'Cambelol'; o mestre Marcelo Passarinho (e amigos da Capoeira); a galera do trompete na ELM. *Et aussi a mes chers amis en France, especialement François, Pauline, et Lisa & Manu. Tous les moments avec vous j'étais trop heureux et tous vous me manquez beaucoup.*

Je suis aussi très content d'avoir eu la chance de travailler chez INRIA (Sophia Antipolis) avec des très bons chercheurs et meilleures personnes en France. Merci a Dr. Stéphane Lanteri et son groupe de recherche. Merci pour votre joie et opportunité.

Por fim agradeço à CAPES e à Unicamp pelo suporte.

Abstract

A novel full-wave method to perform mode analysis on waveguides is introduced in this dissertation. The core of the method is based on an Interior Penalty Discontinuous Galerkin (IPDG) discretization of the vector wave equation. With an appropriate penalty function a spurious-free and high accuracy method is achieved. The efficiency of the proposed method was proved in several waveguides, including intricate optical waveguides with leaky modes and also on plasmonic waveguides. The obtained results were compared with the state-of-the-art mode solvers described in the literature. Also, a discussion on the importance of this new approach is presented. Moreover, the results indicate that the proposed method is more accurate than the previous approaches based on Finite Elements Methods. The main contributions of this work are: the development of a novel robust and accurate method for the analysis of arbitrary waveguides, a new penalty function for the IPDG was proposed and practical applications of the methods are discussed. In addition, in the appendix an application of modal analysis on 3D electromagnetic simulations with a Discontinuous Galerkin method is detailed.

Resumo

Um novo método de onda completo para realizar a análise modal em guias de onda é introduzido nesta dissertação. A ideia central por trás do método é baseada na discretização da equação de onda vetorial com o Método de Galerkin Descontínuo com Penalidade Interior (*IPDG*, do inglês *Interior Penalty Discontinuous Galerkin*). Com uma função de penalidade apropriada, um método de alta precisão e sem modos espúrios é obtido. A eficiência do método proposto é provada em vários guias de onda, incluindo complicados guias de ondas ópticos com modos vazantes e também em guias de onda plasmônicos. Os resultados foram comparados com os métodos do estado-da-arte descritos na literatura. Também é discutida a importância dessa nova abordagem. Além disso, os resultados indicam que o método é mais preciso do que abordagens anteriores baseadas em Elementos Finitos. As principais contribuições deste trabalho são: foi desenvolvido um novo método robusto e de alta precisão para a análise de guias de ondas arbitrários, uma nova função de penalidade para o IPDG foi proposta e aplicações práticas do método proposto são apresentadas. Adicionalmente, no apêndice é apresentado uma aplicação da análise modal em simulação eletromagnética 3D com um método de Galerkin Descontínuo.

List of Figures

List of Abbreviations

CGFEM Continuous Galerking FEM.

DG Discontinuous Galerkin.

DGTD Discontinuous Galerkin Time Domain.

FDTD Finite Difference Time Domain.

FEM Finite Element Method.

IPDG Interior Penalty Discontinuous Galerkin.

NPCGFEM Nodal Penalized Continuous Galerking FEM.

PDE Partial Differential Equation.

PEC Perfect Electric Conductor.

PMC Perfect Magnetic Conductor.

PML Perfect Matched Layer.

Contents

Chapter 1

Introduction

This dissertation is focused on the calculation of light and other electromagnetic waves propagation characteristics through guided wave devices. For doing so a new numerical method for waveguide analysis is introduced, which is inspired on recently developed mathematical methods. Overall it is expected that this new method might be useful for the electromagnetic designers community. A great part of the discussion presented in this dissertation is extracted from the paper [1].

1.1 Numerical Methods in Electromagnetics

In electromagnetics, the analysis and design of waveguides is a key step in the development of devices and systems. Specifically, recent guided wave devices in photonics include waveguides with arbitrary shapes and non-conventional properties due to the adopted materials. In such scenario, the use of analytical methods is impractical and could lead to a fallacious understanding of the underlying physics, as excessive simplifications are required. Therefore, the accurate modeling of complex electromagnetic devices relies on categorical numerical methods.

For the microwave and photonics community, essentially two main computational methods prevail to solve the Maxwell's Equations [2]: the Finite Element Method (FEM) and the Finite Difference Time Domain (FDTD). While both of these methods encompass several variants, its differences are profound. The first one consists on a tessellation of the computational domain to obtain linear algebraic equations from Partial Differential Equations (PDEs), then a discrete finite space is used to approximate the quantity of interest [3, 4]. The latter divides the domain into a cartesian grid of nodes and uses finite differences to approximate derivatives of the quantity of interest, then a time marching scheme is applied to solve the problem in the time domain [5]. On one hand, the FEM is usually used in the frequency domain, therefore simulation of devices in a wide-band are time consuming. On the other hand, the FDTD method is inherently used in the time domain, and when appropriate sources are adopted wide- band simulations are feasible.

Although the FDTD method is simple and efficient, in its standard form it suffers from well-known disadvantages. For instance, the correct approximation of complex geometries is limited to its cartesian grid, which imply in aliasing effects and affect its accuracy. Moreover, its accuracy is bounded by the finite expansion used. Additionally, the material interfaces are hard to handle in this method. On the other hand, the conventional FEMs are more appropriate for the discretization of complex geometries. However, the FEMs in the time domain are less attractive than FDTD because large systems of equations need to be solved in each time step.

1.1.1 The Discontinuous Galerkin Methods

A powerful alternative to the standard FEM and the FDTD that is under intense research is the Discontinuous Galerkin (DG) method [6–12]. The DG methods are indeed similar to the FEMs, however the approximation of the quantity of interest is intrinsically discontinuous, *i.e.* the degrees of freedom are not shared between two adjacent elements. The discontinuity property is achieved since the finite approximation space is local to each element of the tessellation. Then a discrete finite element discontinuous space is adopted to approximate the quantity of interest. Since no shared degrees of freedom are used, the linkage between the neighboring elements is achieved with the numerical flux. There is some freedom to define the numerical fluxes, and this will determine several properties of the DG approach. The discontinuous property implies in an increased memory usage, since the degrees of freedom of each element are not shared.

In Fig. 1.1 the mesh difference between the DG and the standard FEM is illustrated for a 2D domain. The degrees of freedom in the tessellation for the DG method are local to each element, and this is illustrated by the added separation between adjacent elements. As explained above, the connection between elements is done via a numerical flux. The discontinuity is consistent with the Maxwell's equations since the discontinuous nature of the electric and magnetic fields can be catch more appropriately.

The DG method and its variants are quite convenient since they enclose the properties of the conventional FEMs while adding several advantages. The DG methods are a powerful alternative to standard FEMs since they are able to mimic the discontinuous and possibly singular nature of the electromagnetic fields. Additionally, the DG methods are flexible with respect to locally varying element order, they can handle non-conforming meshes and it can lead to diagonal matrices (which results in explicit time/space stepping). In *hp*-adaptive mesh refinement schemes, the use of elements of different sizes and orders is required. Therefore, the DG is well suited for *hp*-adaptivity, time/space marching schemes and parallelization [1].

The DG method can be employed to solve the Maxwell's equations with a discretized time variable, which results in the Discontinuous Galerkin Time Domain

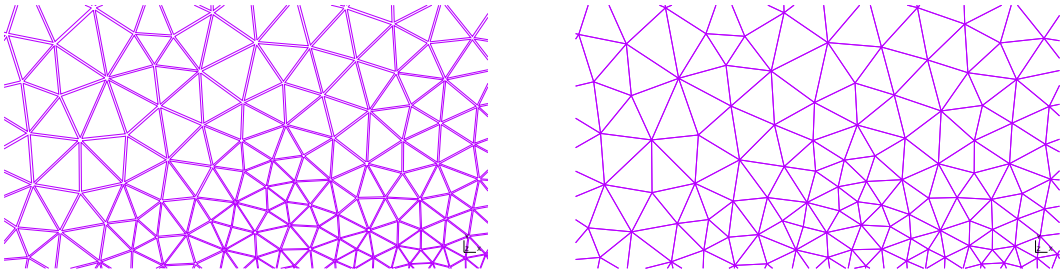

(a) (b)

Figure 1.1: A representation of the mesh difference between the DG method and the FEM. (a) A mesh with isolated triangles for a DG discretization (a small separation is added in-between neighbor elements to illustrated the discontinuity), (b) a mesh for a standard FEM. The mesh in (a) comprises elements that doesn't share its degrees of freedom to its adjacent elements.

(DGTD), a explicit time domain method that does not require the solution of linear equations in each time step [6, 13]. With the advent of the DGTD, the temporal superiority of the FDTD can be combined with the spatial advantage of the FEMs.

For the frequency domain (*i.e.* time-harmonic) Maxwell's equations the DG method is also more convenient since it is able to handle elements of different orders, unstructured meshes, non-conforming meshes and it is able to mimic the discontinuous and possibly singular nature of the electromagnetic fields [1]. Moreover, as it will be shown in this dissertation, the computational cost increment can be made subtle in the frequency domain DG when compared to the conventional continuous Galerkin FEM.

1.2 Motivations for this research

Several optical devices have been proposed recently with increasing geometrical and material complexities. Of elaborate complexity the following ones are highlighted: silicon nanobeam cavities with circular air holes [14], metasurfaces with various structures [15], sectioned tapers for optical interconnection with sandwiched materials [16], sub-wavelength gratings [17–19] and nonlinear silicon photonics components [20]. Additionally, by applying optimization techniques several non-conventional devices also have been proposed recently, interesting examples are provided in [21, 22]. These optimized devices tend to assume bizarre shapes which demand high performance numerical methods. All of these works show a tendency of increasing complexity in guided wave devices. The optical designer community certainly would be glad to explore the aforementioned advantages of the DG methods.

Furthermore, some specific waveguides that could benefit from the discontinuity, mesh handling and other convenient properties of the DG method for waveguide analysis are the following: the light confinement on plasmonic waveguides [23–25], the guidance

of light in photonic-crystal fiber waveguides [26], the guided light characteristics in void nano-structures such as in slot waveguides [27] and in planar waveguides [28], and also the guidance of light at interfaces in planar waveguides [28]. Again, the numerical simulations of the properties of light in all of these waveguides might benefit from the DG method here introduced.

Last but not least, the goal of this dissertation is not to solve all of the problems concerning the simulation of electromagnetic devices, but it does wants to introduce a novel consistent numerical method to the community. Apparently, the method can be useful for the electromagnetic designers community. This dissertation proves the efficiency of a DG method for waveguide analysis and paves the way for further research on DG applications in electromagnetics.

1.3 Contributions

The following contributions of the author related to this Master's Degree are reported:

1. Leandro Andrade-Fonseca and Hugo E. Hernandez-Figueroa, "Full-wave interior penalty discontinuous galerkin method for waveguide analysis" *Accepted for publication in the* IEEE/OSA Journal of lightwave technology. [1]

2. Leandro Andrade-Fonseca and Hugo E. Hernandez-Figueroa, "A Discontinuous Galerkin Method for Optical and Plasmonic Waveguide Analysis" *Accepted for publication in the* OSA the Latin America Optics & Photonics Conference 2018 (LAOP).

3. Leandro Andrade-Fonseca and Hugo E. Hernandez-Figueroa, "A Discontinuous Galerkin Method for Anisotropic Waveguide Analysis" *Accepted for publication in the* SPIE Photonics West, OPTO, Integrated Optics: Devices, Materials, and Technologies XXIII, 2019.

4. Leandro A. C. Fonseca, Hugo E Hernandez-Figueroa, Gilberto T. Santos-Souza, Leonardo L. Bravo-Roger. "Dielectric properties characterization: A simple inverse problem approach." Numerical Electromagnetic and Multiphysics Modeling and Optimization for RF, Microwave, and Terahertz Applications (NEMO), 2017 IEEE MTT-S International Conference on. IEEE, 2017. [29]

5. FONSECA, LEANDRO A. C.; REIS, E. C. ; HERNANDEZ-FIGUEROA, HUGO E ; OLIVEIRA, L. P. . Filtro de Micro-ondas de Alta Potência com Cavidades Ressonantes Coaxiais Compactas e Novas Estruturas de Acoplamento. 2017, Brasil. Patente: Privilégio de Inovação. Número do registro: BR10201701366, título:

‘FILTRO DE MICRO-ONDAS DE ALTA POTÊNCIA COM CAVIDADES RESSONANTES COAXIAIS’ , Instituição de registro: INPI - Instituto Nacional da Propriedade Industrial, Depositante (s): Bradar Indústria - Matriz;Fundação de Desenvolvimento da UNICAMP, Depósito: 23/06/2017

1.4 Outline

The general outline of this dissertation is:

- Chapter 2: the problem of waveguide analysis is stated and discussed. Some relevant approaches to solve it with the FEMs are detailed. The main FEMs are reviewed and the problem of non-physical solutions is examined. Then, the formulations using two different element setups are presented. The elements mathematical properties are presented and discussed. In the end of this chapter some important results are reported to test the implementations.

- Chapter 3: in this chapter the method proposed in this dissertation is introduced and all of its aspects are demonstrated. Its formulation is derived and the numerical flux is presented. The developed penalty function is stated and a simple recipe to guarantee a highly accurate waveguide analysis is presented. Additionally in the end of this chapter the proposed method is validated on a standard waveguide that have analytical solutions. Some comparative results are also shown within the method validation.

- Chapter 4: this chapter is intended to demonstrate the application and efficacy of the proposed method. Results for microwave and optical waveguides are presented. Then, some challenging waveguides, such as lossy, leaky and plasmonic ones, are analyzed. In addition, the performance of the present method is evaluated in comparison with the state-of-the-art mode solvers described in the literature and also with commercial softwares.

- Chapter 5: finally, the last chapter is dedicated to discuss what was developed and also to argue about possible future works.

While doing this Master Degree the author have worked in an additional project related to a 3D DGTD method. In the appendix this project is briefly described.

Chapter 2

Waveguide Analysis

In this chapter the waveguide analysis problem is stated and its solution with standard FEMs is discussed. The issues related to this approach are also discussed. Briefly, the implementations and results made with nodal and edge elements are reported.

2.1 The waveguide eigenvalue problem

The problem of waveguide analysis, which is of main concern in this dissertation, is stated in the following. Suppose a waveguide with an arbitrary cross-section in (x, y) and being uniform along the propagation axis $\hat{z}$. Here it is assumed that this structure is made of inhomogeneous and linear complex materials which are characterized by their tensor relative permittivity $[\epsilon_r]$ and permeability $[\mu_r]$ in (x, y). In photonics, the dielectric materials without any anisotropy are sometimes described by its refractive index n, which is given by $n = \sqrt{\epsilon_r}$. For instance, the Fig. 2.1 illustrates a waveguide with an arbitrary geometry made of three different materials and enclosed by a contour Γ.

The propagating fields at some frequency ω at a given waveguide assume specific distributions, which are in general called as modes. A waveguide can support none or several modes at a given frequency. These modes can be predicted by the solution of the full-wave Maxwell's curl-curl source-free equation:

$$\nabla \times ([\epsilon_r]^{-1} \nabla \times \mathbf{H}) - k_0^2 [\mu_r] \mathbf{H} = 0 \tag{2.1}$$

where $\mathbf{H}$ is the magnetic field (A/m) and $k_0 = \omega\sqrt{\epsilon_0 \mu_0}$ is the free-space wavenumber. Of course, the corresponding electric field $\mathbf{E}$ curl-curl equation could be used. The uniaxial anisotropy is assumed, therefore the $[\epsilon_r]$ and $[\mu_r]$ are diagonal matrices, *i.e.*:

$$[\epsilon_r] = \begin{bmatrix} \epsilon_{xx} & 0 & 0 \\ 0 & \epsilon_{yy} & 0 \\ 0 & 0 & \epsilon_{zz} \end{bmatrix} [\mu_r] = \begin{bmatrix} \mu_{xx} & 0 & 0 \\ 0 & \mu_{yy} & 0 \\ 0 & 0 & \mu_{zz} \end{bmatrix} \tag{2.2}$$

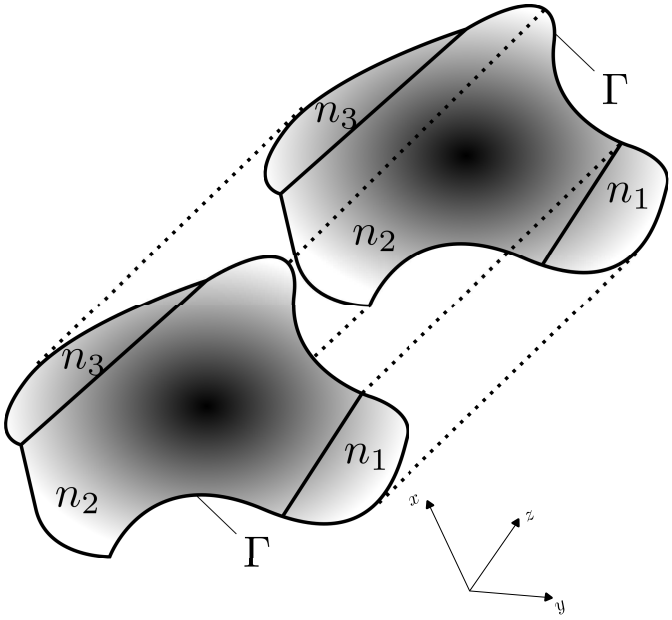

Figure 2.1: An arbitrarily shaped waveguide with 3 different materials and a contour Γ.

Any mode is characterized by its field distribution given by the equation (2.1). Concerning the fields, at material interfaces the tangential components are continuous while the normal component can be discontinuous. Such discontinuities should be considered when solving the wave equation.

In waveguides the time and propagation dependence of the fields can be expressed by $e^{j\omega t - j\beta z}$, where ω is the frequency and β is the propagation constant of the mode. Note that β is a complex value, where its imaginary part is related to the mode attenuation during the propagation. Then, a mode can be fully defined by $(\mathbf{E}, \mathbf{H})$ and β. If one uses the equation (2.1) to find the mode, $\mathbf{E}$ is given by:

$$\mathbf{E} = \frac{1}{j\omega\epsilon_0\epsilon_r}\nabla \times \mathbf{H} \tag{2.3}$$

To find the β value and the fields, one can solve the eigenvalue problem that arises from the equation (2.1). This eigenvalue problem is easier to solve if the magnetic field and the ∇ operator are expanded as:

$$\begin{aligned} \nabla &= \nabla_t + \nabla_z = \nabla_t + (-j\beta)\hat{z} \\ \mathbf{H} &= \mathbf{h}_t + (j\beta)\mathbf{h}_z \end{aligned} \tag{2.4}$$

This expansion in the transverse $\mathbf{h}_t$ and axial $\mathbf{h}_z$ components is useful to build a direct problem for β. Moreover, it allows one to employ different approximations on each one, as it is discussed in the following.

2.2 Waveguide Analysis with the FEM

Probably the most used technique to perform waveguide analysis is the FEM, which is an elegant approach and it is consolidated in the literature since the 80's [30–32]. For very simple waveguides the vectorial equation (2.1) can be solved with a scalar approach that facilitates the eigenvalue problem solution with the FEM. However, in most cases this is not the case and the correct solution requires a full-wave formulation. Then, in the full-wave approach a recurrent and hard to handle problem arises: the problem of non-physical solutions (also called as spurious solutions). The spurious modes are solutions of the discretized wave equation and a FEM waveguide analysis program should be able to eliminate this solutions elegantly.

As part of the research developed in this dissertation, several FEM programs to analyze waveguides were developed, including the scalar approach and the vectorial formulations with both nodal and edge elements. In the following a short description of the discretization of the equation (2.1) with the FEM is presented. Then, an investigation on the nodal and edge approaches is outlined. To be concise here the scalar FEM is not detailed, as this discussion is present in most of the textbooks [3, 4]. Before going into these topics, a necessary and brief discussion on the spurious modes is done.

2.2.1 Spurious Solutions

Intense effort has been made to improve the meticulous analysis of waveguides due to its relevance in basic research. A problem of main concern on the modal analysis with FEM is the spurious solutions that can hinder the analysis of waveguides and cavities [33]. In [34], the spurious solutions issue in eigenvalue problems were deeply studied and a set of conditions to characterize spurious-free FEMs were presented. A major reason for the non-physical solutions is the inaccurate approximation of the null-space in the curl-curl Maxwell equation. It is known that the edge elements are adequate to make a more precise approximation of the null-space [33–35]. Still, a correct approximation of this null-space implies in having unwanted static eigensolutions (at $\omega = 0$) or a null propagation constant ($\beta = 0$). For the time-domain propagation methods [36] and beam space propagation methods [37, 38], a FEM which efficiently eliminates the spurious solutions, including the ones at $\omega = 0$ and with $\beta = 0$, is highly desired.

Back in the 1980's, the problem of spurious solution for waveguides was elegantly handled by including a divergence penalization in the formulation using nodal elements [39]. Also, in [40, 41] the divergence condition was added to the formulation to avoid non-physical solutions. More recently, the divergence condition was again forced into the FEM formulation in [42] to avoid the static spurious solutions. In [43], the edge elements were explored to avoid spurious modes on waveguide analysis. Alternative methods to the FEM for waveguide analysis include the spectral ones [44], the finite-difference [45–47],

the boundary integral equation [48–50], and the meshless [51] methods. On all of these methods, dealing with field singularities (due to sharp corners, for instance) is hard.

2.2.2 The Weak Form

Before using the FEM a weak form of the wave equation (2.1) is required. This weak form is the one which does not contain second order derivatives (curl-curl), so that the continuity requirements for the fields under analysis are reduced. Without loss of generality the procedure here outlined is easily done for the dual electric field wave equation.

Before proceeding, some useful identities are presented:

$$\nabla \cdot (\vec{u} \times \vec{v}) = (\nabla \times \vec{u}) \cdot \vec{v} - (\nabla \times \vec{v}) \cdot \vec{u} \tag{2.5}$$

$$(\vec{u} \times \vec{v}) \cdot (\vec{p} \times \vec{t}) = (\vec{u} \cdot \vec{p})(\vec{v} \cdot \vec{t}) - (\vec{v} \cdot \vec{p})(\vec{u} \cdot \vec{t}) \tag{2.6}$$

$$\int_{\Omega} \nabla \cdot \vec{F} \, \mathrm{d}V = \oint_{\partial\Omega} \vec{F} \cdot \mathbf{n} \, \mathrm{d}S \tag{2.7}$$

where all of the terms are obvious, except for Ω which is a domain of dimension N, $\partial\Omega$ which is its contour of dimension $N-1$ and $\mathbf{n}$ which is an unitary vector normal to $\partial\Omega$ pointing to the outside of Ω.

By invoking the Galerkin method, the weak form can be obtained. First, an inner product of the wave equation with an intentionally undefined test function $\mathbf{\Phi}$ (to be defined with either nodal or edge shape functions) in the domain $\Omega \subset \mathbb{R}^2$ is performed:

$$\int_{\Omega} \mathbf{\Phi} \cdot \left(\nabla \times ([\epsilon_r]^{-1} \nabla \times \mathbf{H}) - k_0^2 [\mu_r] \mathbf{H} \right) \mathrm{d}x \, \mathrm{d}y = 0 \tag{2.8}$$

and with the above identities a weak formulation of the wave equation for the magnetic field is obtained, which is given by:

$$\begin{aligned} \int_{\Omega} (\nabla \times \mathbf{\Phi}) \cdot ([\epsilon_r]^{-1} \nabla \times \mathbf{H}) \, \mathrm{d}x \, \mathrm{d}y + \oint_{\partial\Omega} \left(([\epsilon_r]^{-1} \nabla \times \mathbf{H}) \times \mathbf{\Phi} \right) \cdot \mathbf{n} \, \mathrm{d}\ell \\ -k_0^2 \int_{\Omega^e} (\mathbf{\Phi} \cdot [\mu_r] \mathbf{H}) \, \mathrm{d}x \, \mathrm{d}y = 0 \end{aligned} \tag{2.9}$$

where $\partial\Omega$ is the contour of the domain ($\partial\Omega \in \mathbb{R}^1$ space) and $\mathrm{d}\ell$ is the line path differential in (x, y).

After the discretization with the FEM, the above line integral in the weak-form is discarded inside the domain Ω due to the shared degrees of freedoms between neighboring elements, *i.e.* this is a Continuous Galerkin approach. For now, the above equation is simplified since a Perfect Magnetic Conductor (PMC) ($\mathbf{n} \times \mathbf{H} = 0$) boundary condition is assumed on the global contour of the domain:

$$\oint_{\partial\Omega} \left(([\epsilon_r]^{-1} \nabla \times \mathbf{H}) \times \mathbf{\Phi} \right) \cdot \mathbf{n} \, dxdy = 0 \text{ on } \Gamma \tag{2.10}$$

where Γ is the global contour of the domain Ω. To handle a Perfect Electric Conductor (PEC) boundary condition ($\mathbf{n} \times \mathbf{E} = 0$) a similar approach can be applied which will end up in a quite similar problem setup.

Now, this weak form can be further simplified for treating the waveguide analysis problem stated in the Section 2.1. By applying the operator and field expansion given in (2.4) and doing the same with $\mathbf{\Phi}$:

$$\mathbf{\Phi} = \boldsymbol{\phi_t} + (j\beta)\boldsymbol{\phi_z} \tag{2.11}$$

the derivatives are re-written as:

$$\nabla \times \mathbf{H} = (j\beta)[\nabla_t \times \mathbf{h}_z + \mathbf{h}_t \times \hat{z}] + \nabla_t \times \mathbf{h}_t \tag{2.12}$$

$$\nabla \times \mathbf{\Phi} \ = (j\beta)[\nabla_t \times \boldsymbol{\phi}_z + \boldsymbol{\phi}_t \times \hat{z}] + \nabla_t \times \boldsymbol{\phi}_t \tag{2.13}$$

where $\Big(\mathbf{h}_t(x,y), \mathbf{h}_z(x,y)\Big)$ are the tangential and axial fields, respectively, and $\Big(\boldsymbol{\phi}_t(x,y), \boldsymbol{\phi}_z(x,y)\Big)$ are the test functions to be defined.

After some algebra several steps, a full-wave vectorial weak form for the wave equation is obtained, *i.e.* find $\beta \in \mathbb{C}$ and $\Big(\mathbf{h_t}(x,y), \mathbf{h_z}(x,y)\Big) \in \boldsymbol{H}(\text{curl};\Omega)\times H^1(\Omega)$ such that for all $\Big(\boldsymbol{\phi_t}(x,y), \boldsymbol{\phi_z}(x,y)\Big) \in \boldsymbol{H}(\text{curl};\Omega)\times H^1(\Omega)$:

$$\begin{gathered}
\int_\Omega (\nabla_t \times \boldsymbol{\phi_t} \cdot [\epsilon_r]^{-1} \nabla_t \times \mathbf{h_t})\, dxdy \ - \ k_0^2 \int_\Omega (\boldsymbol{\phi_t} \cdot [\mu_r]\mathbf{h_t})\, dxdy \\
= \\
\beta^2 \Big[\int_\Omega (\nabla_t \times \boldsymbol{\phi_z} \cdot [\epsilon_r]^{-1} \nabla_t \times \mathbf{h_z})\, dxdy \ + \ \int_\Omega (\boldsymbol{\phi_t} \times \hat{z} \cdot [\epsilon_r]^{-1} \nabla_t \times \mathbf{h_z})\, dxdy \\
+ \int_\Omega (\nabla_t \times \boldsymbol{\phi_z} \cdot [\epsilon_r]^{-1} \mathbf{h_t} \times \hat{z})\, dxdy \ + \ \int_\Omega (\boldsymbol{\phi_t} \times \hat{z} \cdot [\epsilon_r]^{-1} \mathbf{h_t} \times \hat{z})\, dxdy \\
- \int_\Omega k_0^2 (\boldsymbol{\phi_z} \cdot [\mu_r]\mathbf{h_z})\, dxdy \Big]
\end{gathered} \tag{2.14}$$

where $\boldsymbol{H}(\text{curl};\Omega)\times H^1(\Omega)$ is a Hilbert space.

Solution via the FEM

With the weak form given by the equation (2.14) the application of the FEM finally can be done to get a discrete version of this weak form. Following the Galerkin method, both the test functions and the unknown field are approximated with a set of functions (here either nodal or hybrid edge/nodal functions). For doing this, three steps are required:

1. The tessellation of the computational domain under analysis to perform the discretization of the weak form to get a linear system for each element;

2. Assembly the contribution of each element to get a global linear system of equations. The test functions in the Galerkin approach are exactly the same ones used to expand the fields $\Big(\mathbf{h}_t(x,y), \mathbf{h}_z(x,y)\Big)$;

3. Solve the corresponding eigenvalue problem that arises with the assembly of the elements.

All of these steps are well discussed in textbooks such as in [3, 4]. The programming of all of these steps can get complicated and to explore code reuse and other advantages all of the FEM codes here developed were programmed with an object-oriented paradigm [52]. With regards to the tessellation, the free software GMSH [53] was used to generate the meshes.

The fields $\Big(\mathbf{h}_t(x,y), \mathbf{h}_z(x,y)\Big)$ in the weak form discretized with the FEM are defined in a discrete Hilbert space, meaning that they exist in a finite dimension space, and the dimension is given by the number of parameters to be determined [54]. Of course, the test functions are defined in the same space.

If a given waveguide has its domain meshed with K triangles, then the assembly of each contribution from the equation (2.14) culminates in the following eigenvalue problem:

$$[A]\mathbf{v} = \beta^2[B]\mathbf{v} \tag{2.15}$$

where $\mathbf{v}$ are the eigenvectors (the modal fields are h_t and h_z), β^2 is the eigenvalue (the squared modal propagation constant), A is the matrix obtained from the right hand side of (2.14) and B is the matrix obtained from the left hand side of (2.14). Then, by solving this global system of equations, which is an eigenvalue problem, a full-wave waveguide analysis can be performed.

Tessellation and area coordinates

The tessellation employed in all of the problems here studied comprises a set of triangles (see for instance the mesh in Fig. 1.1). When using this kind of element, a useful mathematical tool to describe any point in a triangle are the so-called area coordinates (also known as simplex coordinates). For this a general representation of the triangular elements is shown in Fig. 2.2. The node 10 in the cubic element is located at barycenter of the triangle.

For a given point (x, y) inside a general triangle with a counter-clockwise node numbering, as shown in Fig. 2.2, the area coordinates (L_1, L_2, L_3) are:

$$\begin{bmatrix} L_1 \\ L_2 \\ L_3 \end{bmatrix} = \begin{bmatrix} x_1 & x_2 & x_3 \\ y_1 & y_2 & y_3 \\ 1 & 1 & 1 \end{bmatrix}^{-1} \begin{bmatrix} x \\ y \\ 1 \end{bmatrix} \tag{2.16}$$

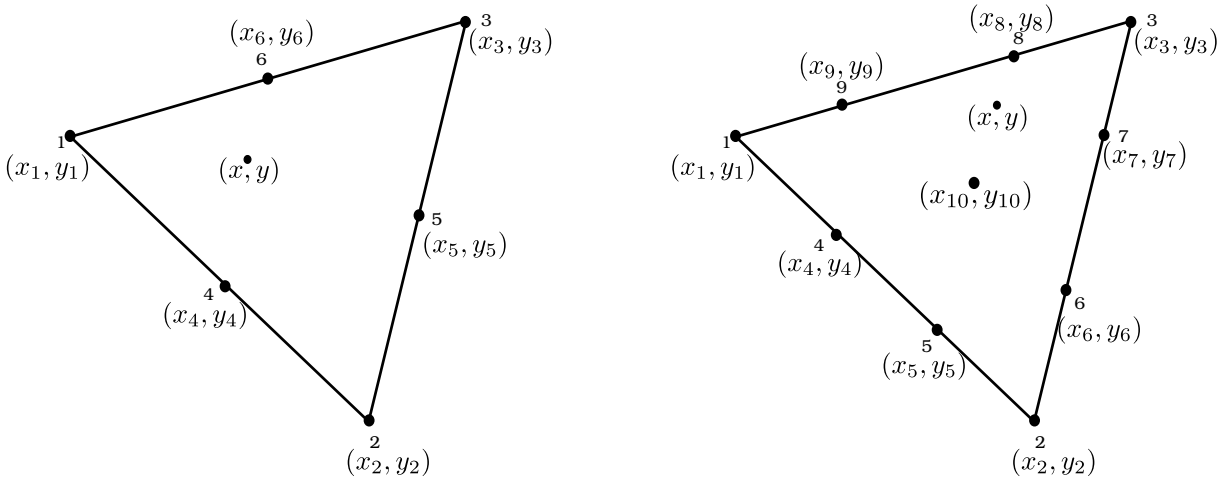

Figure 2.2: A general triangle representation with a given point (x, y). (a) linear or quadratic element, (b) cubic element.

and the area of this triangle element is given by:

$$\Delta^e = \frac{1}{2}\begin{vmatrix} 1 & x_1 & y_1 \\ 1 & x_2 & y_2 \\ 1 & x_3 & y_3 \end{vmatrix} \tag{2.17}$$

Numerical Integration

After the discretization, the contributions of each element in the global system (equation 2.15) have to be calculated. For this, one has to perform numerical integrations to solve each integral in the weak form. When using the area coordinates this can be easily accomplished [3] with:

$$\int_{\Omega^e} F(L_1, L_2, L_3)\, dxdy = \sum_i W_i F(L_{1i}, L_{2i}, L_{3i})\Delta^e \tag{2.18}$$

where Ω^e is the domain of a single element, F is any function of the are coordinates and W_i are the weights. These weights and the exact area coordinates points are performed with the quadrature rules from [55].

2.2.3 Nodal Basis

It is a standard procedure to expand a field quantity in a FEM with nodal elements. The elements here adopted are built with the Lagrangian polynomials. The Lagrangian shape functions (or basis functions) that describe these nodal elements are easy to define with the area coordinates presented in the subsection 2.2.2. The linear shape functions

that approximate a given field with first order functions are given by:

$$\begin{aligned} N_1 &= L_1 \\ N_2 &= L_2 \\ N_3 &= L_3 \end{aligned} \tag{2.19}$$

The quadratic shape functions that approximate a field with second order functions are:

$$\begin{aligned} N_1 &= L_1(2L_1 - 1) \\ N_2 &= L_2(2L_2 - 1) \\ N_3 &= L_3(2L_3 - 1) \\ N_4 &= 4L_1L_2 \\ N_5 &= 4L_2L_3 \\ N_6 &= 4L_3L_1 \end{aligned} \tag{2.20}$$

And the cubic shape functions that approximate a field with third order functions are:

$$\begin{aligned} N_1 &= (9/2)(L_1^3 - L_1^2 + 2L_1/9) \\ N_2 &= (9/2)(L_2^3 - L_2^2 + 2L_2/9) \\ N_3 &= (9/2)(L_3^3 - L_3 + 2L_3/9) \\ N_4 &= (27/2)(L_1^2L_2 - (1/3)L_1L_2) \\ N_5 &= (27/2)(L_1L_2^2 - (1/3)L_1L_2) \\ N_6 &= (27/2)(L_2^2L_3 - (1/3)L_2L_3) \\ N_7 &= (27/2)(L_2L_3^2 - (1/3)L_2L_3) \\ N_8 &= (27/2)(L_3^2L_1 - (1/3)L_3L_1) \\ N_9 &= (27/2)(L_3L_1^2 - (1/3)L_3L_1) \\ N_{10} &= 27L_1L_2L_3 \end{aligned} \tag{2.21}$$

Now, within a triangular element, as the one in Fig. 2.2, the fields exactly at the element nodes are called as $\left(\mathbf{h}_{ti}^e(x,y), \mathbf{h}_{zi}^e(x,y)\right)$, where i is the node number. Then, the fields inside element e are expanded with the shape functions as:

$$\begin{bmatrix} \mathbf{h_t}^e \\ \mathbf{h_z}^e \end{bmatrix} = \begin{bmatrix} h_x^e \\ h_y^e \\ h_z^e \end{bmatrix} = \begin{bmatrix} \sum_{i=1}^{n_p} N_i h_{xi}^e \\ \sum_{i=1}^{n_p} N_i h_{yi}^e \\ \sum_{i=1}^{n_p} N_i h_{zi}^e \end{bmatrix} \tag{2.22}$$

where n_p is the number of nodes used. For a linear nodal triangular element only the

field values at the nodes 1-3 are used, so $n_p = 3$ and the shape functions from (2.19) are necessary. Similarly, for a quadratic nodal triangular element $n_p = 6$ and the shape functions from (2.20) are used, and for a cubic nodal triangular element $n_p = 10$ and the shape functions from (2.21) are used.

An alternative and more compact matrix representation for the field expansion at element e is:

$$\begin{bmatrix} h_x^e \\ h_y^e \\ h_z^e \end{bmatrix} = \begin{bmatrix} \{N\}_{1\times n_p} & \{0\}_{1\times n_p} & \{0\}_{1\times n_p} \\ \{0\}_{1\times n_p} & \{N\}_{1\times n_p} & \{0\}_{1\times n_p} \\ \{0\}_{1\times n_p} & \{0\}_{1\times n_p} & \{N\}_{1\times n_p} \end{bmatrix} \begin{bmatrix} h_{x1}^e \\ ... \\ h_{xn_p}^e \\ h_{y1}^e \\ ... \\ h_{yn_p}^e \\ h_{z1}^e \\ ... \\ h_{zn_p}^e \end{bmatrix} \tag{2.23}$$

where $\{N\}_{1\times n_p}$ is:

$$\{N\}_{1\times n_p} = [N_1 ... N_{n_p}] \tag{2.24}$$

Finally, within the whole waveguide problem domain Ω under the tessellation of N_{elm} elements the total fields are given by:

$$h_x(x,y) = \sum_{i=1}^{N_{elm}} h_x^i \tag{2.25}$$

$$h_y(x,y) = \sum_{i=1}^{N_{elm}} h_y^i \tag{2.26}$$

$$h_z(x,y) = \sum_{i=1}^{N_{elm}} h_z^i \tag{2.27}$$

Discretization

There are many ways to solve the equation (2.14) with the FEM by using the conventional nodal elements [3]. However, solving the time-harmonic curl-curl Maxwell's equation with this kind of elements in general produces the unwanted spurious solutions. Using the three components of the field of interest $\Big(\mathbf{h}_t(x,y), \mathbf{h}_z(x,y)\Big)$ is tricky and the spurious solutions are not easily removed from the solution spectrum. The nodal elements impose strict continuity requirements in the fields at the material interfaces and for this reason they are not appropriate. Strictly speaking the nodal elements do not provide Completeness of the Discrete Kernel (CDK) [34].

To solve this issue, the approach used in the developed codes here is inspired in the famous paper by Rahman *et. al.* [39], which includes a penalization in the formulation with a divergence operator. This penalization works fine since the non-physical solutions in general do not respect the divergence condition $\nabla \cdot \mathbf{H} = 0$.

So, the divergence condition:

$$s\int_{\Omega}(\nabla\cdot\mathbf{\Phi})(\nabla\cdot\mathbf{H})dxdy = s\int_{\Omega}(\nabla_t\cdot\boldsymbol{\phi_t})(\nabla_t\cdot\mathbf{h_t})\,d\Omega + s\int_{\Omega}\beta^2(\nabla_t\cdot\boldsymbol{\phi_t}\,\mathbf{h}_z)\,d\Omega \tag{2.28}$$

was empirically inserted in the formulation. Here s is the penalization parameter, which is a waveguide-dependent and user defined parameter. Note that there is no term including $(j\beta\boldsymbol{\phi_z})$ since the test functions do not have the phase constant $e^{-j\beta z}$.

The weak form of the full-wave equation for nodal elements is then updated to include the divergence penalization from 2.28:

$$\begin{gathered}
\int_{\Omega}(\nabla_t\times\boldsymbol{\phi_t}\cdot[\epsilon_r]^{-1}\nabla_t\times\mathbf{h_t})\,dxdy \;-\; k_0^2\int_{\Omega}(\boldsymbol{\phi_t}\cdot[\mu_r]\mathbf{h_t})\,dxdy \\
+\,s\int_{\Omega}(\nabla_t\cdot\boldsymbol{\phi_t})(\nabla_t\cdot\mathbf{h_t})\,d\Omega \\
= \\
\beta^2\Big[\int_{\Omega}(\nabla_t\times\boldsymbol{\phi_z}\cdot[\epsilon_r]^{-1}\nabla_t\times\mathbf{h_z})\,dxdy \;+\; \int_{\Omega}(\boldsymbol{\phi_t}\times\hat{z}\cdot[\epsilon_r]^{-1}\nabla_t\times\mathbf{h_z})\,dxdy \\
+\int_{\Omega}(\nabla_t\times\boldsymbol{\phi_z}\cdot[\epsilon_r]^{-1}\mathbf{h_t}\times\hat{z})\,dxdy \;+\; \int_{\Omega}(\boldsymbol{\phi_t}\times\hat{z}\cdot[\epsilon_r]^{-1}\mathbf{h_t}\times\hat{z})\,dxdy \\
-\int_{\Omega}k_0^2(\boldsymbol{\phi_z}\cdot[\mu_r]\mathbf{h_z})\,dxdy \\
-\,s\int_{\Omega}(\nabla_t\cdot\boldsymbol{\phi_t})\,(\mathbf{h_z})\,d\Omega\Big]
\end{gathered} \tag{2.29}$$

And finally, with the finite-element procedure the weak form can be discretized. Suppose that Ω is partitioned in K elements, then a scalar finite element space is defined as:

$$Q^h := \{u \in L^2(\Omega)\,,\, \forall K \in \Omega,\, u_K \in \mathcal{P}(K)\} \tag{2.30}$$

$L^2(\Omega)$ being the Lebesgue space and $\mathcal{P}(K)$ being the space of Lagrangian polynomials defined on K. In the discrete version of the weak formulation (2.29) the eigenvalue problem is to find $(\mathbf{h_t}, h_z, \beta^2) \in (Q^h \times Q^h, Q^h, \mathbb{C})$ for all $(\boldsymbol{\phi_t}, \phi_z) \in (Q^h \times Q^h, Q^h)$. Then, with the above mentioned linear, quadratic or cubic nodal elements the $\boldsymbol{H}$(curl;Ω) vectorial space is approximated, while with the same nodal elements the $H^1(\Omega)$ scalar space is approximated.

2.2.4 Hybrid Edge/Nodal Basis

A hybrid element configuration that comprises an edge shape function set for the $\mathbf{h_t}$ and nodal ones for the $\mathbf{h_z}$ has been used in waveguide analysis for a while now [42,43,56]. This implies in a direct vectorial approximation for the transverse field. Then, the curl-curl null space is correctly approximated and does not pollute the solution spectrum for $\beta \neq 0$.

The edge basis presented in [57] is employed here for the $\mathbf{h_t}$ component, as this vector basis satisfy the Nédelec constraints [58]. For the $\mathbf{h_z}$ component, the conventional nodal quadratic or cubic elements is used. As explained above, this vectorial edge element guarantees the tangential field continuity while allowing for the normal field jumps, and therefore it correctly approximates the Maxwell's equation field solutions. Due to this, no spurious modes are observed when using this element setup (except for the ones at $\beta = 0$) as the vectorial field $\mathbf{h_t}$ is well expanded in this vectorial finite dimensional space.

The edge elements are also known as the linear tangential/linear normal (LT/LN) and linear tangential/quadratic normal (LT/QN) ones. They are quite convenient to the present formulation as shown next. Indeed, numerical results for two hybrid elements setup are presented: LT/LN edge functions with quadratic nodal functions and LT/QN edge functions with cubic nodal functions. From now on, these hybrid elements are referred as LT/LN/Q and LT/QN/C.

The LT/LN vectorial shape functions are given by:

$$\begin{aligned}
\mathbf{T_1} &= l_{12} L_1 \nabla L_2 \\
\mathbf{T_2} &= l_{23} L_2 \nabla L_3 \\
\mathbf{T_3} &= l_{31} L_3 \nabla L_1 \\
\mathbf{T_4} &= l_{12} L_2 \nabla L_1 \\
\mathbf{T_5} &= l_{23} L_3 \nabla L_2 \\
\mathbf{T_6} &= l_{31} L_1 \nabla L_3
\end{aligned} \tag{2.31}$$

where l_{ij} is the edge length between the nodes 1-3 of the triangle. For the LT/QN shape functions two more functions are added to form the basis:

$$\begin{aligned}
\mathbf{T_7} &= L_2 L_3 \nabla L_1 - L_1 L_2 \nabla L_3 \\
\mathbf{T_8} &= L_1 L_3 \nabla L_2 - L_1 L_2 \nabla L_3
\end{aligned} \tag{2.32}$$

Observe that $\mathbf{T_i}$ have components in $\hat{x}$ and $\hat{y}$ due to the ∇ operator, *i.e.* $\mathbf{T_i} = T_{xi}\hat{x} + T_{yi}\hat{y}$. The superposition of the LT/LN functions ensures a triangle element with a basis that has linear tangential and linear normal functions. And the superposition of the LT/QN functions provides a triangle with a basis that has linear tangential (first order) and quadratic normal functions.

For either the LT/LN or the LT/QN, the shape functions in $\hat{x}$ and $\hat{y}$ are called

as T_{xi} and T_{yi}, respectively, and N_j are the conventional nodal shape functions. Then the $\mathbf{h_t}$ and $\mathbf{h_z}$ are:

$$\mathbf{h_t}^e = \begin{bmatrix} h_x^e \\ h_y^e \end{bmatrix} = \begin{bmatrix} T_{x1} & T_{x2} & ... & T_{xn_e} \\ T_{y1} & T_{y2} & ... & T_{yn_e} \end{bmatrix} \begin{bmatrix} h_{t1}^e \\ ... \\ h_{tn_p}^e \end{bmatrix} \tag{2.33}$$

$$\mathbf{h_z} = \hat{z} \sum_{j=1}^{n_p} N_j h_{zj} \tag{2.34}$$

where h_{ti}^e are the local field variables, with $(n_e = 6, n_p = 6)$ for LT/LN/Q and $(n_e = 8, n_p = 10)$ for LT/QN/C.

Discretization

With the edge elements shape functions the curl-curl null space is nicely catch, and no explicit divergence condition needs to be imposed. Therefore, the weak formulation from (2.9) can be directly discretized with the FEM procedure.

Again, suppose that Ω is partitioned in K hybrid edge/nodal elements, then a vector and scalar finite element space are defined as:

$$\begin{aligned} \mathbf{V}^h &:= \{\mathbf{u} \in L^2(\Omega)^2, \forall K \in \Omega, \mathbf{u_K} \in \mathcal{S}(K)\}\} \\ Q^h &:= \{u \in L^2(\Omega), \forall K \in \Omega, u_K \in \mathcal{P}(K)\} \end{aligned} \tag{2.35}$$

$L^2(\Omega)$ being the Lebesgue space, $\mathcal{P}(K)$ being the space of Lagrangian polynomials defined on K and $\mathcal{S}(K)$ being the vectorial space of polynomials $\mathcal{P}(K)^2$ defined on K. In the discrete version of the weak formulation (2.14) the eigenvalue problem consists is finding $(\mathbf{h_t}, h_z, \beta^2) \in (\mathbf{V}^h, Q^h, \mathbb{C})$ for all $(\boldsymbol{\phi_t}, \phi_z) \in (\mathbf{V}^h, Q^h)$. Then, with the above mentioned LT/LN/Q or LT/QN/C elements the $\boldsymbol{H}$(curl;Ω) vectorial space is approximated, while with the nodal elements the $H^1(\Omega)$ scalar space is approximated.

2.2.5 Perfect Matched Layers

To handle an open waveguide the Perfect Matched Layer (PML) materials [59] are added at the outermost regions of the domain backed by either PEC or PMC walls. Here the PMLs are implemented in the same fashion as in [60]. Following this approach, the above defined weak formulation is kept the same, except for the modified $[\epsilon_r]$ and $[\mu_r]$

matrices, *i.e.*:

$$[\epsilon_{rPML}] = \epsilon_r \begin{bmatrix} c_x & 0 & 0 \\ 0 & c_y & 0 \\ 0 & 0 & c_z \end{bmatrix} \tag{2.36}$$

$$[\mu_{rPML}] = \mu_r \begin{bmatrix} c_x & 0 & 0 \\ 0 & c_y & 0 \\ 0 & 0 & c_z \end{bmatrix} \tag{2.37}$$

where ϵ_r and μ_r are the parameters for the material adjacent to the PML and c is given by:

$$c = \theta - j\frac{\sigma}{\omega\epsilon_r} \tag{2.38}$$

σ being the PML material conductivity profile, and by default set $\theta = 1$. σ is changed throughout the depth of the PML layer as follows:

$$\sigma = \sigma_{max}\left(\frac{\rho}{d}\right)^m \tag{2.39}$$

where σ_{max} is a user-defined constant, ρ is the distance from the PML layer start, and d is the PML layer thickness.

The properties (c_x, c_y, c_z) at this absorbing layer are defined differently depending on the PML-domain interface region. For a PML-material interface located in a region with constant x, the PML parameters are set as $c_x = 1/c$, $c_y = c$ and $c_z = c$. When it is located in a region with constant y, $c_x = c$, $c_y = 1/c$ and $c_z = c$. And at the corner regions $c_x = 1$, $c_y = 1$ and $c_z = c^2$.

At open waveguides the PMLs bounded by PEC/PMC conditions are used, therefore "Berenger" modes, also known as box modes, tend to appear for very large domains [61]. Fortunately, these modes are easily recognized and discarded.

2.3 Results with the FEM

In this section some key simulations are presented to evaluate the implementations of the above described FEM formulations on benchmark waveguides. First, some results for the FEM with nodal elements are shown with discussions and exposing its problems. Then, the advantages of the FEM with edge elements are explored and discussed through simulations. The methods are designated as:

- Nodal Penalized Continuous Galerking FEM (NPCGFEM): the discrete version of the weak formulation given in (2.29) using nodal elements;
- Continuous Galerking FEM (CGFEM): the discrete version of the weak formulation

given in (2.14) using edge elements;

Concerning the code, the following commentaries about the implementations can be made:

- All of the FEM codes were programmed with Object-oriented programming [52] in Matlab [62];
- The complex eigenvalue problem is solved with sparse matrices solvers from the numpy/scipy libraries in Python or the Matlab (eigs function);
- All waveguides were modeled and meshed with the GMSH free software [53];
- The meshing is automatically done and imported with some Python programs developed;
- The data processing and parsing related to the mesh is also programmed in Python;
- The most critical part of the code, the assembly, is optimized with sparse matrices, such that the matrix filling process is as fast as possible.

In addition to the results here present, in the Appendix A an application of mode sources for light propagation in very long silicon photonics Bragg Gratings is shown. The research presented in this appendix used the NPCGFEM code to provide the mode solutions for 3D DGTD simulations.

2.3.1 Rectangular Waveguide

The most basic waveguide is the rectangular one with either PEC or PMC walls. It is a square structure filled with air. Although it is a simple waveguide, it is quite useful to assess the accuracy of a method since its analytical solutions are easily obtained. Such a waveguide bounded by PMC walls and with a cross-section of $10.16\,\text{mm} \times 22.86\,\text{mm}$ was analyzed and compared to its analytical solutions. Here a mesh of 304 quadratic triangles was used.

Nodal

The penalization was set to either $s = 0$ or $s = 1$ to evaluate the eigensolutions in a wide spectrum with the NPCGFEM. In the Fig. 2.3 it is seem that the analytical solutions in each frequency were well captured.

All of the solutions that do not match with the analytical one in Fig. 2.3(a) are indeed the infamous spurious modes. When $s = 1$ these unwanted modes are removed from the solution spectrum, as depicted in Fig. 2.3(b). The $\beta = 0$ solutions are intentionally left in these figures. They are easily recognized and discarded in the waveguide analysis

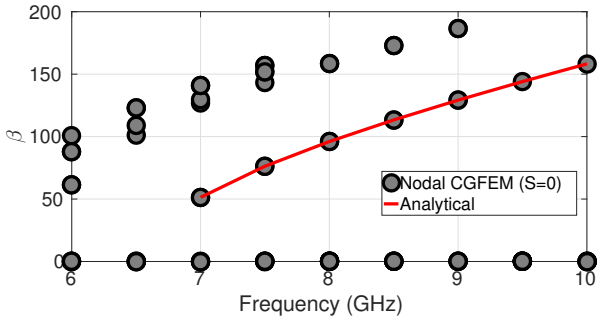

(a)

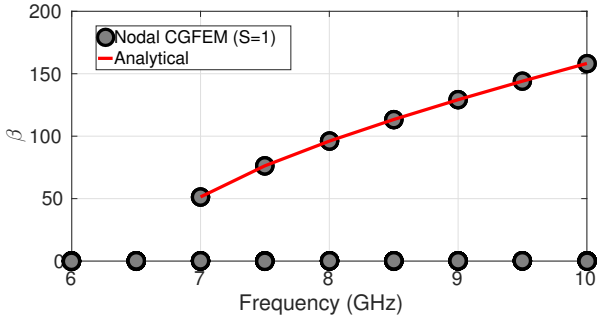

(b)

Figure 2.3: Waveguide analysis of the standard X-band rectangular waveguide with the NPCGFEM using quadratic shape functions. (a) penalty parameter set to 0 and (b) penalty parameter set to 1.

since its β values are usually tiny (real part in the order of 10^{-10}). Of course, cleaning these $\beta = 0$ values for waveguides operating close to the cut-off is harder, but in most of the cases the waveguides operate far from the cut-off. Alternatively, the $\beta = 0$ modes can also be avoided by setting a suitable eigenvalue search. For a frequency of 9 GHz, the correct and a spurious solution are shown in Fig. 2.4. In the spurious solution the divergence condition violation is visually appreciated.

Edge

When using the CGFEM, no spurious modes were found. The results are shown in Fig. 2.5. This time the $\beta = 0$ modes were filtered at the eigenvalue search, such that they are not present in the solution.

2.3.2 Rectangular Waveguide with a hole

Even though the spurious modes problem is partially solved with the divergence penalty, an important drawback of the NPCGFEM is that it can't naturally handle non-convex domains. *i.e.*, no conforming nodal FEM can treat domains with reentrant corners. Among others, this is one of the reasons for the electromagnetics community to use the

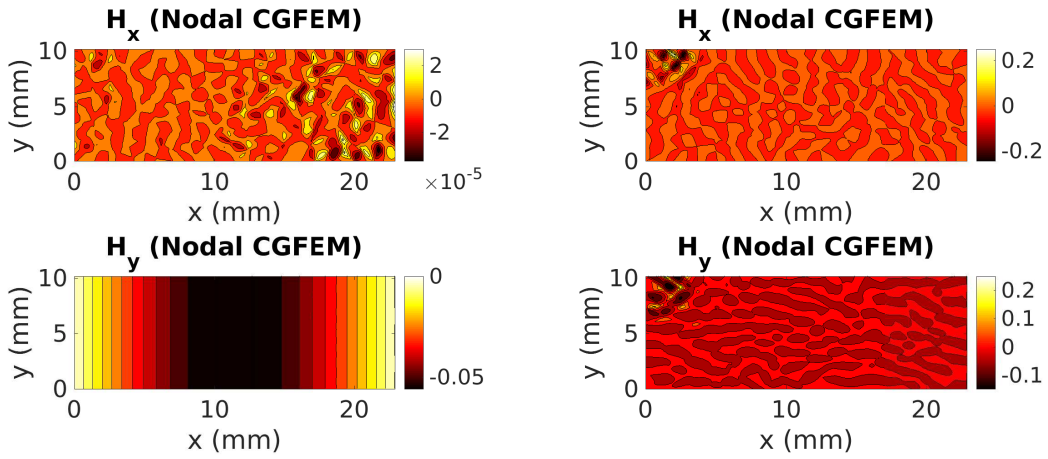

(a) (b)

Figure 2.4: Transverse magnetic field $\mathbf{h}_t$ of a correct and a spurious solution of the standard X-band rectangular waveguide operating at 9 GHz, analyzed with the NPCGFEM. (a) a correct solution and (b) a spurious solution.

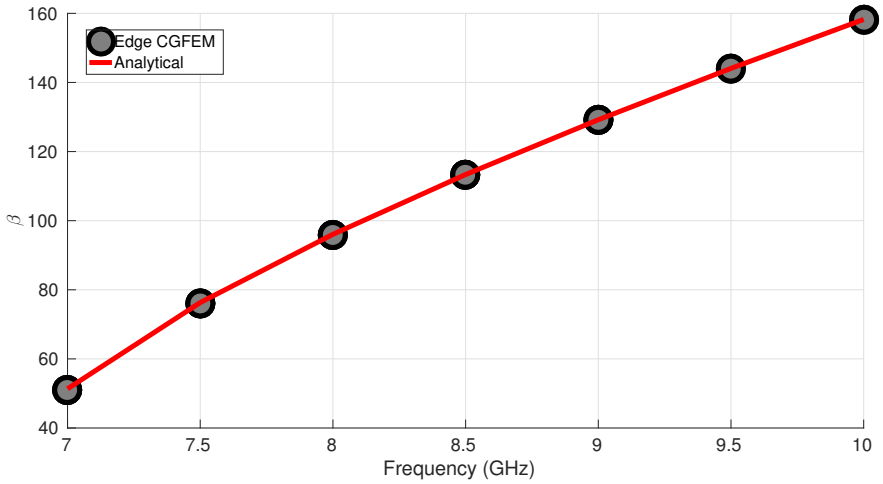

Figure 2.5: Waveguide analysis of the standard X-band rectangular waveguide with the CGFEM employing the LT/LN/Q hybrid elements.

edge elements instead of the nodal ones. This aspect of the nodal elements was clarified and studied in [35]. To check this property the PMC bounded rectangular waveguide with a hole shown in Fig. 2.6 was analyzed. This time the mesh comprised 1104 quadratic elements (not shown in this figure), to better capture the field singularities

Nodal

With the NPCGFEM no correct mode was found for several penalty parameters and meshes setups (at $f = 12$ GHz). This was expected and confirms the theory from [35].

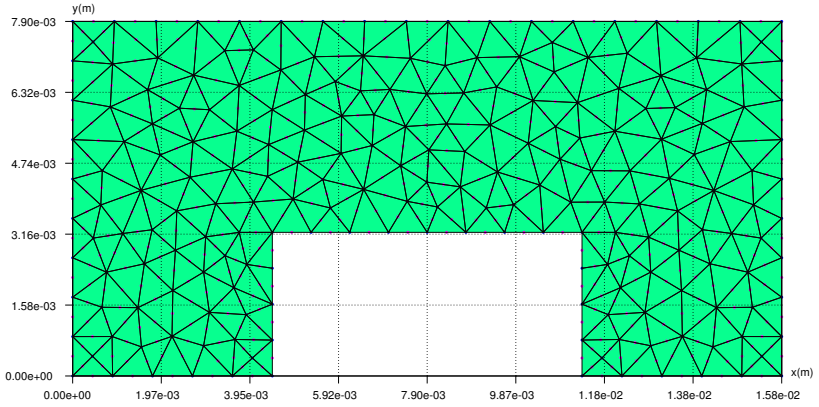

Figure 2.6: Rectangular Waveguide with a hole (non-convex domain) shown with its mesh. Its correct solutions can't be calculated with the NPCGFEM.

Edge

This tricky holed waveguide was again analyzed at $f = 12\,\text{GHz}$ with the CGFEM yielding good results in comparison a commercial software, the Ansys HFSS [63]. In the commercial software the dominant mode propagation constant was found to be $\beta = 197.37$ when using the port modes solution with the default setup. In the CGFEM code it was found to be $\beta = 198.48$ with the 1104 elements mesh. Apparently, the latter is more precise due to the use of this refined mesh with high order elements (LT/QN/C). This can be appreciated in the comparison of the fields from both solvers, presented in Fig. 2.7.

To get a more fair comparison with the HFSS software, the commercial software setup was modified to do an adaptive mesh refinement with 19 passes and a Delta S value of 10^{-6}. In this case, the basis was set to second order instead of the default first order basis used above. The port results for β were evaluated through the refinement process and the values are shown in Fig. 2.8(b). Then, a non-adaptive mesh refinement with the CGFEM was performed. In the CGFEM the mesh was changed by modifying the elements sides with a linear variation between 5 mm and 0.45 mm. The mesh having element sides of 0.45 mm comprised 1746 elements. The results for the convergence of β for the CGFEM code are shown in Fig. 2.8(a). It can be seen that as the mesh is increased (smaller elements sides), the β values match well with the converged one from the HFSS using second order elements.

2.3.3 Strip Waveguide (photonic wire)

In Fig. 2.9 a conventional photonic waveguide is illustrated, the outermost boxes are the PMLs used to mimic its open waveguide characteristics. It usually comprises a high index core (n_c, commonly silicon), patterned above a substrate layer (n_b, commonly silica

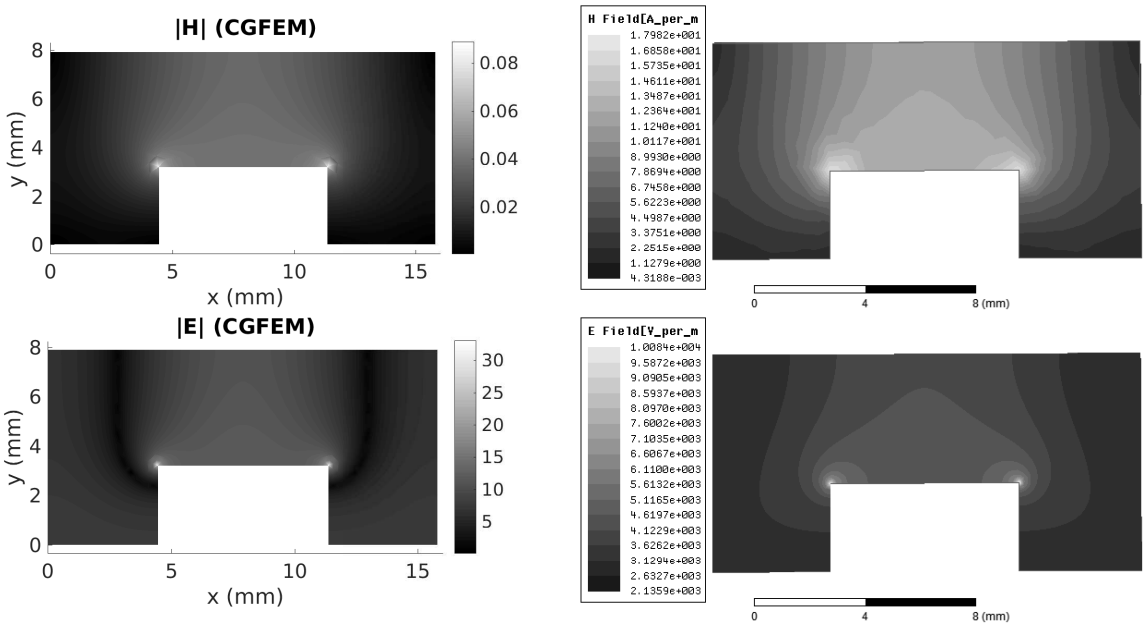

(a) CGFEM (b) HFSS

Figure 2.7: Absolute electric and magnetic fields of rectangular waveguide with a hole (non-convex domain) operating at 12 GHz. (a) the solution with the CGFEM (b) the solution with the HFSS commercial software.

- SiO_2) and a cladding (n_{air}, commonly air or silica) above the silicon and silica. Also, there is a thick silicon layer below the silica (n_s, commonly silicon or silica).

In the case of the strip waveguide, the layer of height h_1 and width w is made of silicon ($n_c = 3.5$) mounted on a SiO_2 ($n_b = 1.45$) buffer of height h_2, both above an underlying layer of height S also made of silicon ($n_s = 3.5$), in which the air cladding is kept. For this waveguide w can vary from about 300 nm up to 600 nm for single mode operation around 1500 nm. Typically, photonic devices operate under single-mode condition, where the adopted light is either TE or TM polarized. The nomenclature TE/TM comes from 1D slab waveguides theory. For real optical waveguides TE/TM modes are just an inherited naming and it does not mean that the longitudinal components or any other component of either the electric or magnetic fields are null. Instead, it separates the mode fields which have electric fields components rather aligned (TM) or perpendicular (TE) to the plane of incidence. Therefore, from now on a different naming for those modes is chosen: Quasi-TE and Quasi-TM.

Here the conventional strip waveguide (photonic wire) was analyzed operating at $\lambda_0 = 1.55\,\mu$m under a leaky mode condition. When the underlying silicon layer is included in the modal analysis, it is known that the fundamental mode is leaky, as shown in the work [64], and the correct calculation of n_{eff} is cumbersome due to its imaginary part. This waveguide is a nice benchmark to evaluate mode solvers (which can handle leaky modes) and it was rigorously studied in [65], [64] and [66]. In the present analysis, the

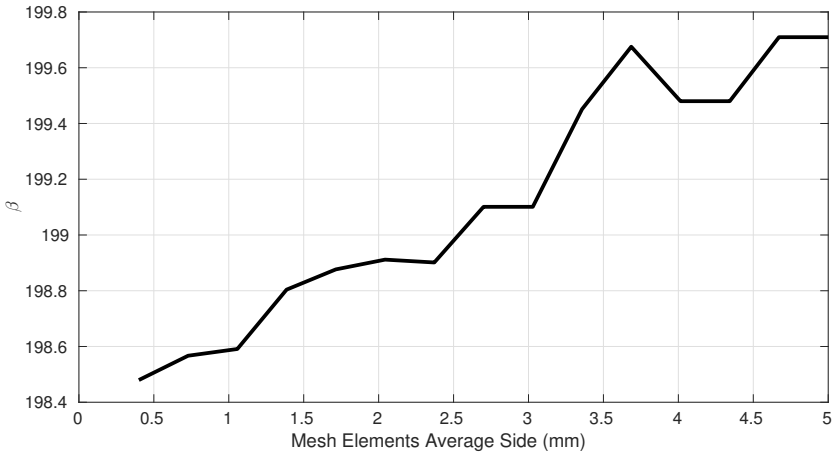

(a) CGFEM

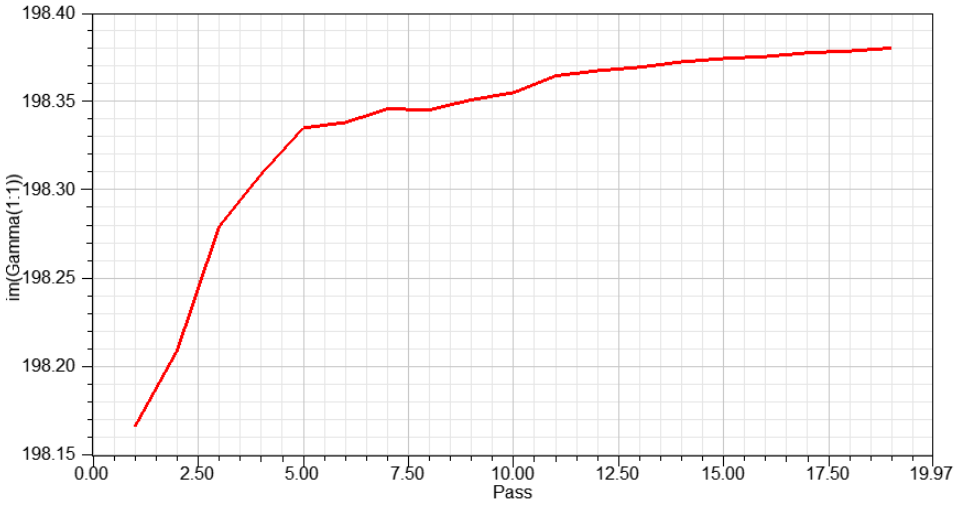

(b) HFSS

Figure 2.8: Mesh refinement for computing the β of the holed waveguide. (a) the solution with the CGFEM as the mesh is refined (b) the solution with the HFSS commercial software using its adaptive mesh refinement.

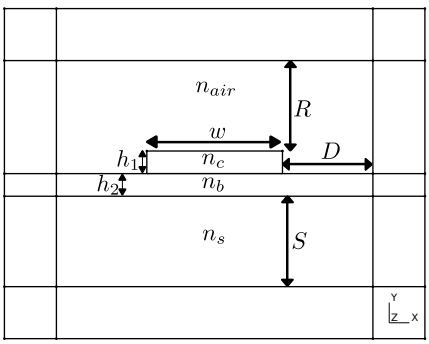

Figure 2.9: Typical photonic waveguide cross-section with its dimensions. The outer rectangles are the PML layers.

dimensions were set to $S = D = R = h_2 = 1\,\mu$m, $w = 500\,$nm, $h_1 = 220\,$nm to aim for the same leaky mode as in those references. The PML thickness in this case was set to λ_0, and

after a convergence analysis on Imag$\{n_{eff}\}$ its parameters were set to $\sigma_{max} = 10^{16}$ with a cubic conductivity profile ($m = 3$). The mesh consists of 8158 quadratic elements the core having elements with side lengths of about 40 nm. For this scenario, the best known reported index is $n_{eff} = 2.412372 - j2.9135 \times 10^{-8}$ [65].

Nodal

This device was again analyzed with the NPCGFEM code. Now the penalty parameter was set to $s = 1/n_c^2$ for removing the spurious solutions. In this case some 'Berenger' modes were found and recognized due to their large loss. In the wavelength under analysis only the fundamental Quasi-TE mode was found with an index of $n_{eff} = 2.405 - j2.9 \times 10^{-7}$. This value is not too far from the ones reported in the references. However, the leaky mode condition was not well captured since the mode index loss is about 10 times bigger than expected. The electric field of the three components is shown in Fig. 2.10(a). It can be seen that the nodal elements are not capable of capturing the singular fields at the corners.

Edge

Finally, this waveguide was evaluated with the CGFEM. In this case, the LT/QN/C higher order elements were used to improve the solution precision. No spurious modes were found, but the same 'Berenger' modes appeared and were discarded. With this setup the Quasi-TE fundamental mode was found to have $n_{eff} = 2.412352 - 2.934526 \times 10^{-8}$, which is quite close to the references. Observe that the imaginary part is now more accurate and it complies with the reference values. Additionally, the field solution, detailed in Fig. 2.10(b), is much more accurate and the corners singularities are nicely captured.

2.4 Commentaries

Overall in this chapter the waveguide analysis problem was studied. The FEM approach was discussed and some results with different elements setups were presented. From the results it is clear that the hybrid elements outperform the nodal ones due to the better approximation of the $\boldsymbol{H}(\text{curl};\Omega)$ vectorial space achieved with the edge shape functions.

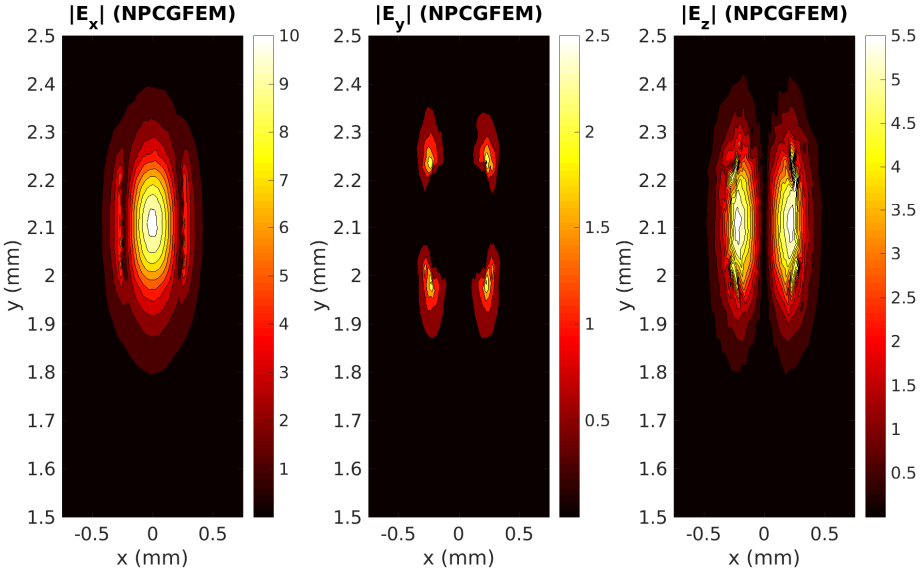

(a) NPCGFEM

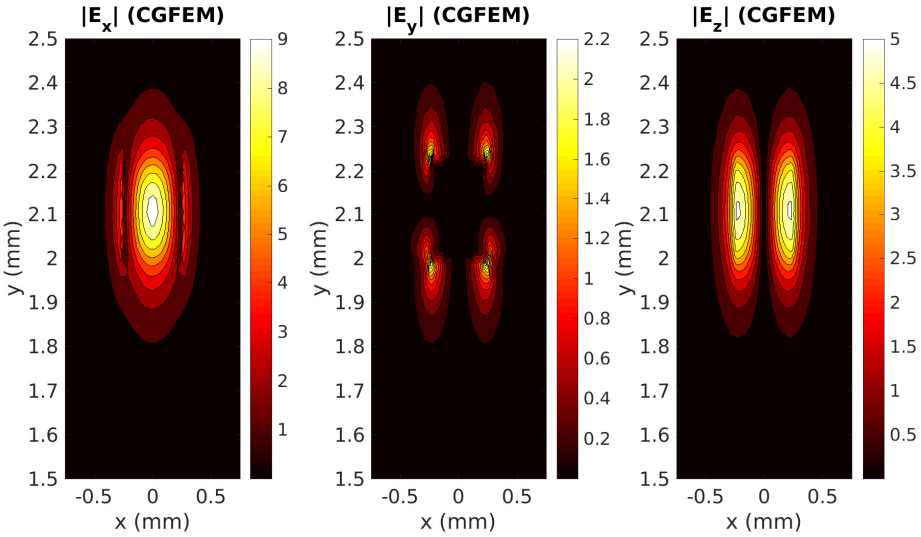

(b) CGFEM

Figure 2.10: Electric fields profile for the photonic wire with a 500 nm × 220 nm obtained from: (a) the NPCGFEM; (b) from the CGFEM. Fields are zoomed at the core region.

Chapter 3

Interior Penalty Discontinuos Galerkin for Waveguide Analysis

Finally, in this chapter the method proposed in this dissertation is introduced. The proposed novel method is a combination of the the Interior Penalty Discontinuous Galerkin (IPDG) method with the standard FEM to perform waveguide analysis with high accuracy. From now this combined method is cas IPDG/FEM. Before introducing the IPDG/FEM some topics to clarify the present method are discussed, namely the non-physical solutions, the reason for using the IPDG and the DG flux.

3.1 The spurious-free property and the IPDG choice

For the second order (curl-curl) time-harmonic Maxwell's equation, some spurious-free DG methods have been studied in the literature: [67–71]. A local DG method with nodal elements was used in [67, 68], and it was shown that a sufficiently large penalty function is useful to remove the spurious modes from the solution spectrum. In essence this penalization shifts the non-physical solutions out of the discrete solution spectrum. In [68] the authors argue that this conclusion can be extended to other DG techniques, such as the IPDG. Alternatively, the first order time-harmonic Maxwell's equation solution with the DG is discussed in [72].

The IPDG method was applied in [69, 70] for the analysis of resonant cavities. This approach yields a symmetric system with a penalization in the numerical flux to eliminate the spurious modes. A penalty function, if well defined, can be employed to eliminate the spurious solutions in a consistent manner in the IPDG method. Indeed, it has been shown by Buffa and Perugia in [71] that the IPDG methods on eigenvalue problems are spurious-free in the sense of [34].

Then, if one seeks to exploit the advantages of the DG for the waveguide analysis problem the IPDG can be viewed as a promising approach. A waveguide analysis with this

method would also be spurious-free and suitable for intricate optical waveguides. Moreover, on specific complex waveguides, such as a plasmonic one, the advantages of the DG might come handy.

Therefore, in this research the IPDG formulation from [69–71] was considered. The Nédelec conforming elements were used combined to the nodal conventional FEM. This approach results in a robust novel method to compute waveguide modes with high accuracy and which eliminates non-physical solutions in a controlled manner with a penalty term. In order to make a precise analysis of intricate optical waveguides the Perfect Matched Layers (PML) [59] were included in the computation of open waveguides in the same fashion as in the Sub-Section 2.2.5. With an adequate penalty function, a spurious-free method in the sense of [34] was observed, as expected from the theory presented in [71]. The proposed method was tested in several waveguides yielding excellent results.

In the IPDG/FEM approach the unwanted null-space (related to the eigenvalues with $\beta = 0$ or $\omega = 0$) is still present since no divergence condition is explicitly imposed. These eigenvalues are easily filtered out of the solution spectrum by means of using limits on the eigenvalues search. Additionally, in [73] and in [74] the IPDG method was successfully extended to the time domain, producing stable explicit time-stepping numerical schemes, indicating that contrary to what was expected from [75] the unwanted null-space solutions do not affect the stability of those time domain numerical schemes. These results justify the analysis here presented. Moreover, these works indicate that the present method could be directly associated with time/space marching schemes for mode propagation.

3.2 DG Penalized Flux: tangential jump and average

As in all DG methods, a numerical flux between adjacent elements must be defined and applied to couple the local-element basis at faces or edges. The flux definition is not unique and its choice will dictate the convergence and stability of the method [6, 7, 76]. In this work the flux is the same as the one shown in [71] and [69], which is built with the tangential jump and average, defined hereafter. For now, this definitions might seem vague, but they are presented for later usage.

Suppose a general domain Ω meshed with a set of elements K and the faces set $\mathcal{F}$ (edges in a 2D domain). $\mathcal{F}$ consists of the interior faces $\mathcal{F}_i$ and the boundary faces $\mathcal{F}_b$. Let $\mathbf{n}$ be the unit outward normal vector of a face in $\mathcal{F}$. Each face in $\mathcal{F}_i$ is shared by two elements. K_L and K_R are the adjacent elements (left and right) sharing a given face in $\mathcal{F}_i$ (obviously $\hat{n}_L = -\hat{n}_R$). Now, suppose a discontinuous vectorial quantity $\mathbf{u}$ at Ω, where $\mathbf{u}_L$ and $\mathbf{u}_R$ are the traces of $\mathbf{u}$ in a given face of $\mathcal{F}$. The trace is the local value of $\mathbf{u}$ at the

face. The tangential jump $[\![\mathbf{u}]\!]$ and average $\{\mathbf{u}\}$ can finally be defined as:

$$\begin{aligned} [\![\mathbf{u}]\!] &= \mathbf{n}_L \times \mathbf{u}_L + \mathbf{n}_R \times \mathbf{u}_R \\ \{\mathbf{u}\} &= (\mathbf{u}_L + \mathbf{u}_R)/2 \end{aligned} \tag{3.1}$$

for a face in $\mathcal{F}_i$. And for a face in $\mathcal{F}_b$, which has no adjacent element:

$$\begin{aligned} [\![\mathbf{u}]\!] &= \mathbf{n}_L \times \mathbf{u}_L \\ \{\mathbf{u}\} &= \mathbf{u}_L \end{aligned} \tag{3.2}$$

In Fig. 3.1 two LT/LN elements sharing an edge are shown and the quantities that will contribute to $[\![\mathbf{u}]\!]$ and $\{\mathbf{u}\}$ are detailed. Note that the edge numbering must be consistent.

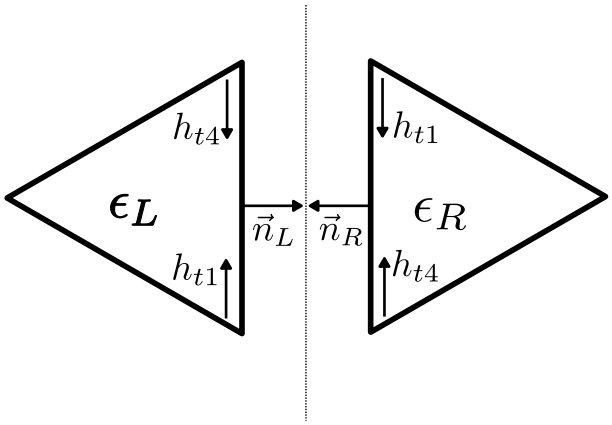

Figure 3.1: Shared edge between two elements with materials ϵ_L and ϵ_R to illustrate the flux contributions on a given edge.

It is interesting to note that if the LT/QN elements are used the numerical flux is kept unchanged, since the enrichment functions ($\mathbf{T_7} = T_{x7}\hat{x} + T_{y7}\hat{y}$ and $\mathbf{T_8} = T_{x8}\hat{y} + T_{y8}\hat{y}$ from equations (2.32)) do not present tangential components along the edges. This is illustrated in Fig. 3.2 for a given triangle. This is quite advantageous since the approximation order is increased without requiring additional terms in the global matrices related to the flux terms.

With $[\![\mathbf{u}]\!]$ and $\{\mathbf{u}\}$, the DG numerical flux that is applied to the wave equation (2.1) can be defined. As this discussion is out of the scope of this dissertation no further details are presented. The excellent papers by Houston *et al* [69], A. Buffa and I. Perugia [71] and Sármány *et al* [77] bring more details on this topic. Specifically, [77] brings details on how to insert $[\![\mathbf{u}]\!]$ and $\{\mathbf{u}\}$ into the equation (2.1) with two distinct fluxes.

In this work the flux adopted is the interior penalty one [77], which introduces a penalization to the tangential jump at the faces. The penalization is controlled by a penalty parameter. While this parameter can assume large values, it is a powerful and simple feature to eliminate spurious solutions [68, 77]. A discussion on the penalty value

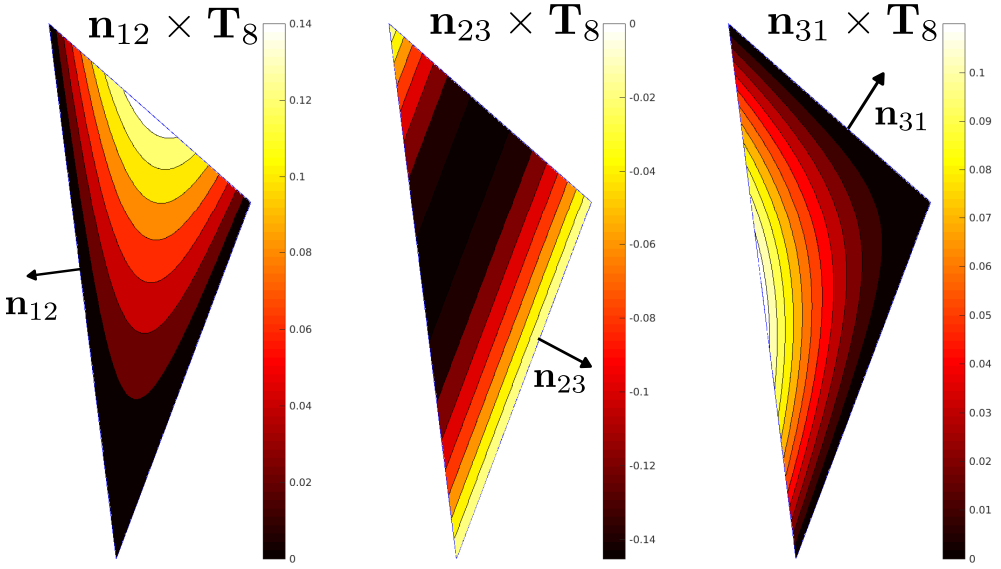

Figure 3.2: LT/QN shape function T_8 cross each edge normal showing that the LTQN enrichment functions contributions to the flux terms are null.

for different problems is given in the following.

3.3 The combined DG/FEM method

First, the discrete inner product on Ω in a 2D finite element space is given by:

$$\int_{\Omega} \mathbf{u} \cdot \mathbf{v} \, dS = (\mathbf{u}, \mathbf{v}) \tag{3.3}$$

for the elementwise area integrals. And:

$$\int_{\mathcal{F}} \mathbf{u} \cdot \mathbf{v} \, dl = (\mathbf{u}, \mathbf{v})_{\mathcal{F}} \tag{3.4}$$

for the edgewise line integrals, where dS is the area differential and dl is the line path differential in (x, y). The line integrals are numerically obtained using Gaussian quadrature, while the area ones are performed with the quadrature rules from [55].

In [69, 71, 77], the approximation of equation (2.1) in a finite element space with the symmetric IPDG discrete formulation is given. The formulations from these works are used to solve the cavity problem, which is inherently different to the waveguide one. Then, the eigenvalue is k_0^2. If $\mathbf{\Phi}$ are the test functions, then find $(\mathbf{H}, k_0^2)$ such that for all $\mathbf{\Phi}$:

$$\begin{aligned} &(\nabla \times \mathbf{\Phi}, [\epsilon_r]^{-1} \nabla \times \mathbf{H}) \; - \; k_0^2 (\mathbf{\Phi}, [\mu_r] \mathbf{H}) \\ &- (\{[\epsilon_r]^{-1} \nabla \times \mathbf{\Phi}\}, [\![\mathbf{H}]\!])_{\mathcal{F}} \; - \; ([\![\mathbf{\Phi}]\!], \{[\epsilon_r]^{-1} \nabla \times \mathbf{H}\})_{\mathcal{F}} \; + \; \mathsf{a}_T([\![\mathbf{\Phi}]\!], [\![\mathbf{H}]\!])_{\mathcal{F}} = 0 \end{aligned} \tag{3.5}$$

where $k_0 = \frac{2\pi}{\lambda_0}$, λ_0 is the air vacuum wavelength, a_T is the penalty function. Below this formulation is adapted for the guided mode analysis problems.

Before proceeding, it is important to focus on the physical aspects of the problem of interest here: the 2D waveguide analysis. It is known that the non-physical solutions in mode analysis are avoided if edge elements are used in the tangential component h_t. Yet, to better handle material discontinuities and singularities a non-conforming method, for instance the IPDG method, is more appropriate. For the waveguide modal analysis, the inhomogeneity lies in the tangential component. Due to this, here the h_z field is solved with the classical FEM, while h_t is solved with an adapted version of the IPDG method (equation (3.5)). It is also prudent to use the DG method only at h_t, since the DG method introduces more degrees of freedom in comparison to the conventional FEM. To solve h_z with a Continuous Galerkin FEM implies in:

$$\begin{aligned} [\![\mathbf{h_z}]\!] &= 0 \\ \{\mathbf{h_z}\} &= 0 \end{aligned} \tag{3.6}$$

Specifically, this means that the hybrid edge/nodal functions were adopted to calculate the unknown field in the novel IPDG/FEM modal analysis scheme. With the LT/LN or LT/QN elements detailed in the Sub-Section 2.2.4 the $\boldsymbol{H}$(curl;Ω) vectorial space is approximated, while with the conventional nodal quadratic or cubic Lagrange elements the $H^1(\Omega)$ scalar space is approximated. Note that different to the standard FEM, here the $\mathbf{h}_t$ field is solved with a DG method, and hence the edge shape functions are local to each element. This allows the proposed method to catch strong field variations at material interfaces more appropriately.

Now, the spaces definition are updated appropriately:

$$\begin{aligned} \mathbf{V}^h &:= \{\mathbf{u} \in L^2(\Omega)^2\,, \forall K \in \Omega,\, \mathbf{u_K} \in \mathcal{S}(K)\}\} \\ Q^h &:= \{u \in L^2(\Omega)\,, \forall K \in \Omega,\, u_K \in \mathcal{P}(K)\} \end{aligned} \tag{3.7}$$

$L^2(\Omega)$ being the Lebesgue space, $\mathcal{P}(K)$ being the space of Lagrangian polynomials defined on K and $\mathcal{S}(K)$ being the vectorial space of polynomials $\mathcal{P}(K)^2$ defined on K. Now $\mathbf{V}^h$ is a discontinuous vector space since the degrees of freedom are local to each $K \in \Omega$ in the IPDG. Observe that the scalar space Q^h is kept the same as in the standard FEM.

Now, again the field expansion from equations (2.4) and (2.11) were applied in both $\mathbf{H}$, ∇ and at $\mathbf{\Phi}$ in the equation (3.5). Then the original equation (3.5) can be particularized to the 2D problem. For the tangential jump and average (recall the

equations (3.6)):

$$\{[\epsilon_r]^{-1}\nabla \times \boldsymbol{\Phi}\} = (j\beta)\{[\epsilon_r]^{-1}\boldsymbol{\phi_t} \times \hat{z}\} + \{[\epsilon_r]^{-1}\nabla_t \times \boldsymbol{\phi_t}\} \tag{3.8}$$

$$\{[\epsilon_r]^{-1}\nabla \times \mathbf{H}\} = (j\beta)\{[\epsilon_r]^{-1}\mathbf{h_t} \times \hat{z}\} + \{[\epsilon_r]^{-1}\nabla_t \times \mathbf{h_t}\} \tag{3.9}$$

$$[\![[\epsilon_r]^{-1}\mathbf{H}]\!] = [\![[\epsilon_r]^{-1}\mathbf{h_t}]\!] \tag{3.10}$$

$$[\![\boldsymbol{\Phi}]\!] = [\![\boldsymbol{\phi_t}]\!] \tag{3.11}$$

note that both $[\![[\epsilon_r]^{-1}\mathbf{h_t}]\!]$ and $[\![\boldsymbol{\phi_t}]\!]$ are vectors in $\hat{z}$.

Then, by inserting the above equations in the equation (3.5), the inner product of the flux terms are particularized as:

$$\int_{\mathcal{F}}\{[\epsilon_r]^{-1}\nabla \times \boldsymbol{\Phi}\} \cdot [\![\mathbf{H}]\!]dl = \int_{\mathcal{F}}\{[\epsilon_r]^{-1}\nabla_t \times \boldsymbol{\phi_t}\} \cdot [\![\mathbf{h_t}]\!]dl \tag{3.12}$$

$$\int_{\mathcal{F}}[\![\boldsymbol{\Phi}]\!] \cdot \{[\epsilon_r]^{-1}\nabla \times \mathbf{H}\}dl = \int_{\mathcal{F}}[\![\boldsymbol{\phi_t}]\!] \cdot \{[\epsilon_r]^{-1}\nabla_t \times \mathbf{h_t}\}dl \tag{3.13}$$

$$\mathsf{a}_T \int_{\mathcal{F}}[\![\boldsymbol{\Phi}]\!] \cdot [\![[\epsilon_r]^{-1}\mathbf{H}]\!]dl = \mathsf{a}_T \int_{\mathcal{F}}[\![\boldsymbol{\phi_t}]\!] \cdot [\![\mathbf{h_t}]\!]dl \tag{3.14}$$

Finally, in the following the formulation of the novel IPDG/FEM modal analysis scheme is defined. If $\boldsymbol{\phi_t}$ and $\boldsymbol{\phi_z}$ are the test functions for $\mathbf{h_t}$ and $\mathbf{h_z}$, respectively, find $(\mathbf{h_t}, h_z, \beta^2) \in (\mathbf{V}^h, Q^h, \mathbb{C})$ such that for all $(\boldsymbol{\phi_t}, \phi_z) \in (\mathbf{V}^h, Q^h)$:

$$\begin{gathered}
(\nabla_t \times \boldsymbol{\phi_t}, [\epsilon_r]^{-1}\nabla_t \times \mathbf{h_t}) \; - \; k_0^2(\boldsymbol{\phi_t}, [\mu_r]\mathbf{h_t}) \\
- (\{[\epsilon_r]^{-1}\nabla_t \times \boldsymbol{\phi_t}\}, [\![\mathbf{h_t}]\!])_{\mathcal{F}} \; - \; ([\![\boldsymbol{\phi_t}]\!], \{[\epsilon_r]^{-1}\nabla \times \mathbf{h_t}\})_{\mathcal{F}} \\
+ \mathsf{a}_T([\![\boldsymbol{\phi_t}]\!], [\![\mathbf{h_t}]\!])_{\mathcal{F}} \\
= \\
\beta^2\Big[(\nabla_t \times \boldsymbol{\phi_z}, [\epsilon_r]^{-1}\nabla_t \times \mathbf{h_z}) \; + \; (\boldsymbol{\phi_t} \times \hat{z}, [\epsilon_r]^{-1}\nabla_t \times \mathbf{h_z}) \\
+ (\nabla_t \times \boldsymbol{\phi_z}, [\epsilon_r]^{-1}\mathbf{h_t} \times \hat{z}) \; + \; (\boldsymbol{\phi_t} \times \hat{z}, [\epsilon_r]^{-1}\mathbf{h_t} \times \hat{z}) \\
- k_0^2(\boldsymbol{\phi_z}, [\mu_r]\mathbf{h_z})\Big]
\end{gathered} \tag{3.15}$$

If one removes the flux terms from the equation (3.15) and setup the problem with a classical FEM approach, *i.e.* with shared degrees of freedom between elements, a conventional Continuous Galerkin FEM (CGFEM) problem is obtained.

Either the PEC or PMC walls can be incorporated into the equation (3.15) in the same manner as in the classical FEM.

The flux related terms in the equation (3.15) can be expanded to better understand its implementation. With the equations (3.1) and checking the Fig. 3.1, it is easy to see that each flux related term comprises a permutation of the adjacent elements L and R

contributions. For instance, the first flux related integration term in equation (3.15) is:

$$\begin{aligned}\{[\epsilon_r]^{-1}\nabla_t \times \boldsymbol{\phi_t}\} \cdot [\![\mathbf{h_t}]\!] = 0.5\Big(\\ ([\epsilon_L]^{-1}\nabla_t \times \boldsymbol{\phi_{t}}_L) \cdot (\mathbf{n}_L \times \mathbf{h_t}_L) + \\ ([\epsilon_L]^{-1}\nabla_t \times \boldsymbol{\phi_{t}}_L) \cdot (\mathbf{n}_R \times \mathbf{h_t}_R) + \\ ([\epsilon_R]^{-1}\nabla_t \times \boldsymbol{\phi_{t}}_R) \cdot (\mathbf{n}_L \times \mathbf{h_t}_L) + \\ ([\epsilon_R]^{-1}\nabla_t \times \boldsymbol{\phi_{t}}_R) \cdot (\mathbf{n}_R \times \mathbf{h_t}_R)\Big)\end{aligned} \tag{3.16}$$

where ϵ_L and ϵ_R are the ϵ_r of elements L and R, respectively. Similar equations will arise from the other flux terms.

The assembly of the contributions from all K elements and all edges in $\mathcal{F}$ will culminate in an eigenvalue problem for β^2, given by:

$$[A]\mathbf{v} = \beta^2[B]\mathbf{v} \tag{3.17}$$

where $\mathbf{v}$ are the eigenvectors - the modal fields h_t and h_z, β^2 is the eigenvalue - the modal propagation constants, A is the matrix obtained from the right hand side of (3.15) and B is the matrix obtained from the left hand side of (3.15). Then, by solving this eigenvalue problem a full-wave waveguide analysis can be performed. This formulation is free of non-physical solutions in the sense of [34] for a large penalty parameter.

Notice that the dual electric field formulation is easily obtained following the same approach, except that the starting equation is for $\mathbf{E}$.

3.4 The Penalty Function

The value of a_T is dependent on the dimensions, polynomial order and materials of the adjacent elements. This value is problem dependent, however from [68] it is known that when $\mathsf{a}_T \to \infty$ the spurious eigensolutions are removed from the solution spectrum. However, using such a large value is impractical when solving an eigenvalue problem. Instead, a function for each face in the domain should be defined to handle each element interface differently.

Although the actual value for the penalty term is somewhat arbitrary, some hints on its chosen value are given in [77] and [78]. Inspired by these works and after performing an empirical analysis the penalty function is chosen as:

$$\mathsf{a}_T = \alpha_T\Big(\frac{1}{\sqrt{l_e}}\Big)\Big(\frac{1}{A(K_L)} + \frac{1}{A(K_R)}\Big)(min(|\epsilon_L|, |\epsilon_R|))^{-1} \tag{3.18}$$

for edges in $\mathcal{F}_i$, and:

$$\mathsf{a}_T = \alpha_T \Big(\frac{1}{\sqrt{l_e}}\Big)\Big(\frac{2}{A(K_L)}\Big)(|\epsilon_L|)^{-1} \tag{3.19}$$

for edges in $\mathcal{F}_b$. The α_T is a global, positive and user defined value independent of the mesh, l_e is the edge length, and $A(K)$ is the area of one of the adjacent elements sharing an edge. It was observed that a penalty function leaning towards the above definitions is indeed free of non-physical solutions. Moreover, the α_T is useful to increase the accuracy and to avoid badly scaled matrices. Note that a_T is an edge-local parameter.

3.4.1 Recipe to attain high accuracy

For the problems tackled with the IPDG/FEM method, it is apparent that $\alpha_T \approx 10^2$ guarantees a high accuracy solution for microwave waveguides. On the other hand, on intricate optical waveguides, the α_T value ranges from 10^{-4} to 10^{-3}. This parameter depends on the smallest elements of the mesh: for optical waveguides with reduced element sides of about 10 nm it was observed that by setting $\alpha_T \approx 10^{-4}$ accurate solutions are achieved. While for sides of about 40 nm set $\alpha_T \approx 10^{-3}$. Setting α_T closer to these values is appropriate to avoid a badly scaled eigenvalue problem, since the elements are extremely small for optical waveguides. Indeed, a spurious free mode solver with high accuracy is ensured even when setting α_T below these recommended values. Further discussions on this parameter are presented below in practical applications.

Overall, a subtle better performance of the IPDG/FEM was observed over the CGFEM in all of the waveguides analyzed so far. And this is directly associated with the α_T parameter value, as shown in the numerical examples in the following chapter. Indeed, the values above described for α_T are just like a recipe that until now is proven to be very good to analyze any waveguide with unprecedented high accuracy (in comparison to prior FEM-like approaches). Following the recipe for this parameter it is expected that any user will be able to solve the waveguides with high accuracy and without any spurious solutions. The role of the penalty function and its mathematical aspects are deeply discussed in the paper [68].

3.5 Method Validation and investigation of the α_T parameter

In this chapter a novel scheme to perform a full-wave analysis of arbitrarily shaped waveguides was demonstrated by means of a discretization of the Maxwell's vector wave equation with an IPDG combined with a standard FEM, named as IPDG/FEM. Prior to solving intricate waveguides, a careful validation of the proposed method must be

performed. Here, the validation was done on a quite simple structure: the rectangular waveguide operating at the microwave spectrum.

In all of the examples reported in this section a classical X-band homogeneous rectangular waveguide bounded by PMC walls was considered. Although this is a simple structure, its analytical solutions facilitate the evaluation of the method and the investigation of the the penalty parameter α_T effects in the equations (3.18) and (3.19). This waveguide has a cross-section of $10.16\,\text{mm} \times 22.86\,\text{mm}$. This structure was solved with the proposed combined IPDG/FEM for several α_T values in different frequencies.

3.5.1 Global Matrices Structure

Before proceeding on the method validation, the shape of the global matrices of the IPDG/FEM and the CGFEM for the rectangular waveguide problem on a fixed mesh are illustrated in Fig. 3.3. It is interesting to see that the IPDG results in an almost diagonal matrix for B. Note that although the number of degrees of freedom is increased in the DG method, the number of non-zero values (nz in the figure) in the global matrices is only 14.89% bigger than that of the CGFEM.

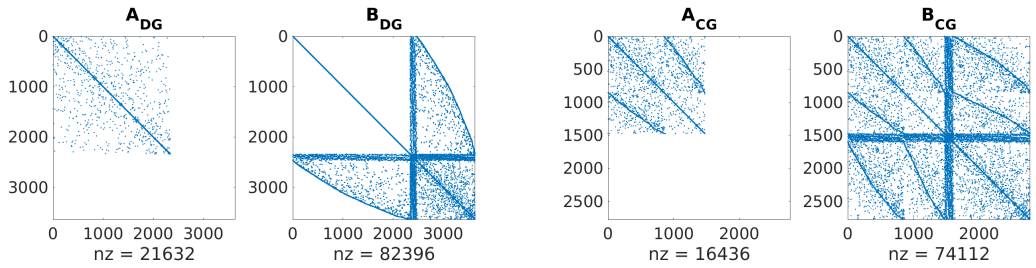

(a) (b)

Figure 3.3: Global matrices comparison for the rectangular waveguide: (a) IPDG/FEM, (b) CGFEM.

3.5.2 Dispersion of the Rectangular Waveguide

The dispersion study from the Sub-Section 2.3.1 of the aforementioned waveguide was repeated for four α_T values: 0, 10^{-4}, 10^{-2} and 1. In this study the mesh used in the Sub-Section 2.3.1 (304 triangles) with the LT/QN/C elements was repeated. This mesh has triangles with the mean $l_e = 1.5\,\text{mm}$. The results are shown in Fig. 3.4. Note that spurious solutions were only found for $\alpha_T = 0$. However, for $\alpha_T < 1$ the accuracy is clearly low.

The dispersion results validated the proposed method. However, some important insights on the α_T effect can be delineated:

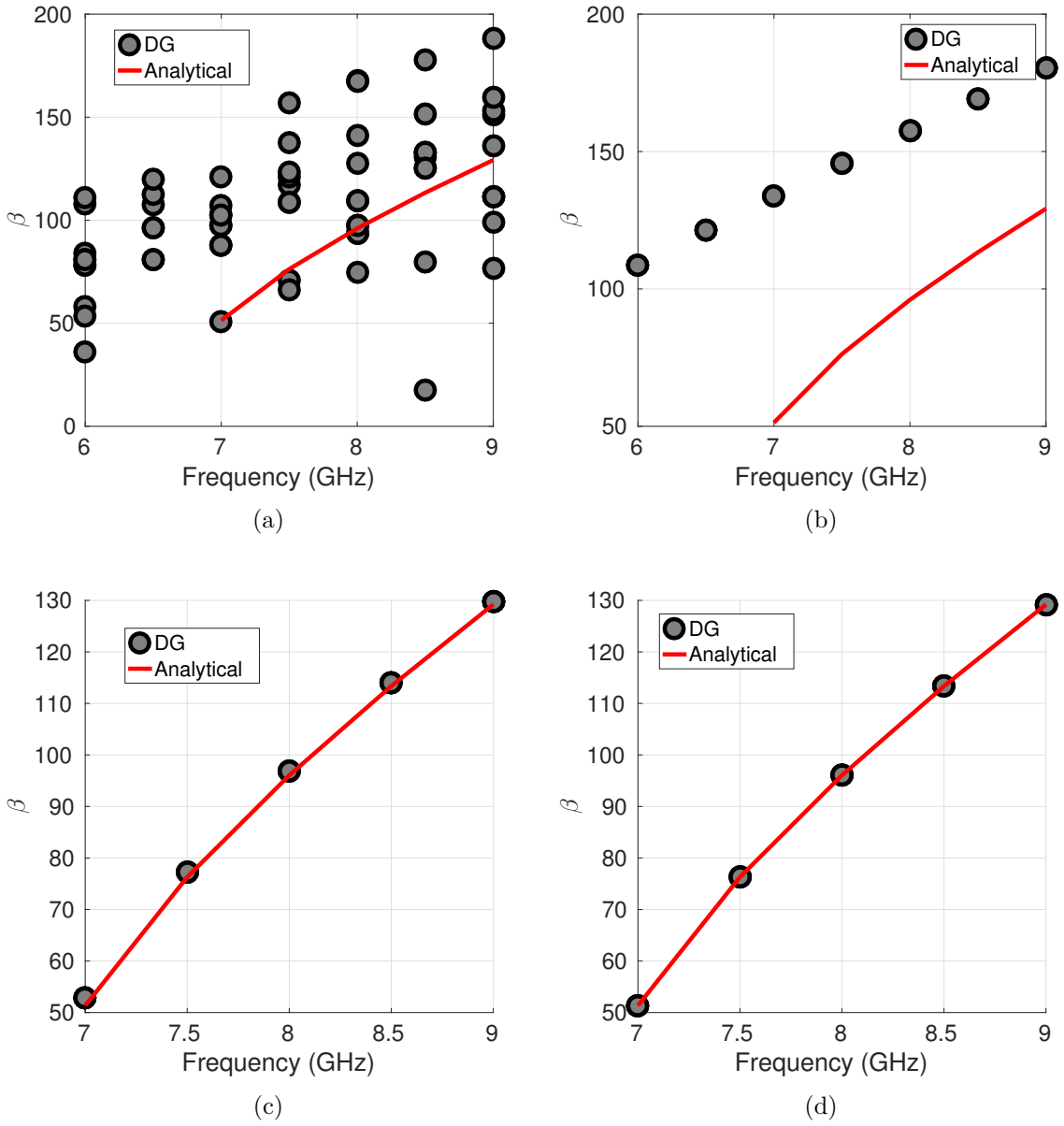

Figure 3.4: Dispersion analysis of the standard X-band rectangular waveguide with the IPDG/FEM for several α_T values. (a) $\alpha_T = 0$, (b) $\alpha_T 10^{-4}$, (c) $\alpha_T = 10^{-2}$ and (d) $\alpha_T = 1$.

- Apparently the proposed penalty function is effective to shift the spurious eigenvalues out of the solution spectrum;
- The penalty function by itself is not enough to guarantee a highly accurate solution;
- The penalty parameter α_T should be scaled for a given domain and mesh, such that it compensates the penalty function in a convenient manner;

Although the above observations are important, a more precise definition of α_T is needed. For this in the following some insightful empirical analysis obtained from numerical simulations are presented.

3.5.3 α_T effect on the accuracy

To better estimate the effect of α_T on the accuracy of the present method several simulations with different penalty parameter values and using either the LT/QN/C or the LT/LN/Q elements were performed. In this study the 304 triangles mesh was repeated. The results are summarized in Fig. 3.5(a), where the error plot is shown for the dominant mode propagation constant. The error is the normalized difference between the IPDG/FEM (β) and the reference one obtained analytically (β_{Ref}). Closer to the cut-off frequency the error is increased, but this effect is less prominent for $\alpha_t \geq 1$. And, in Fig. 3.5(b) a detailed view of the error for $\alpha_t \geq 1$ is shown. In both figures the error of the corresponding conventional CGFEM is given. For LT/QN/C, when $\alpha_t = 10000$ the IPDG/FEM error is slightly smaller than that of the CGFEM, but at the cost of using more degrees of freedom for the h_t component. In the inset of Fig. 3.5(b) this error reduction can be observed.

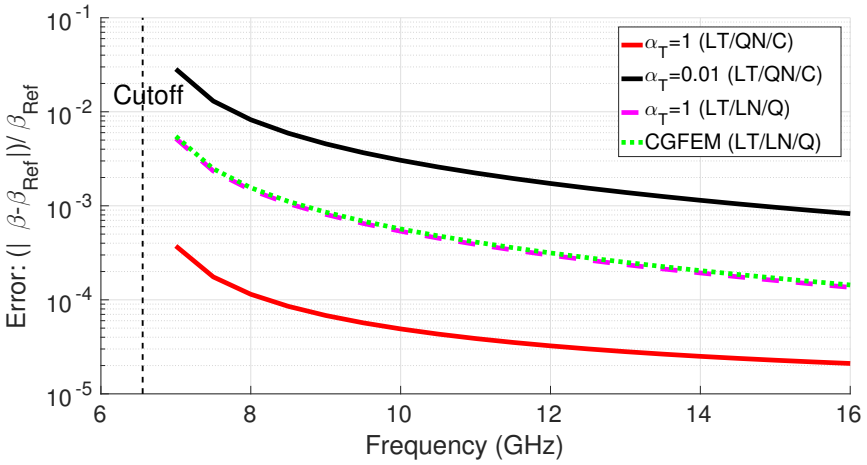

(a)

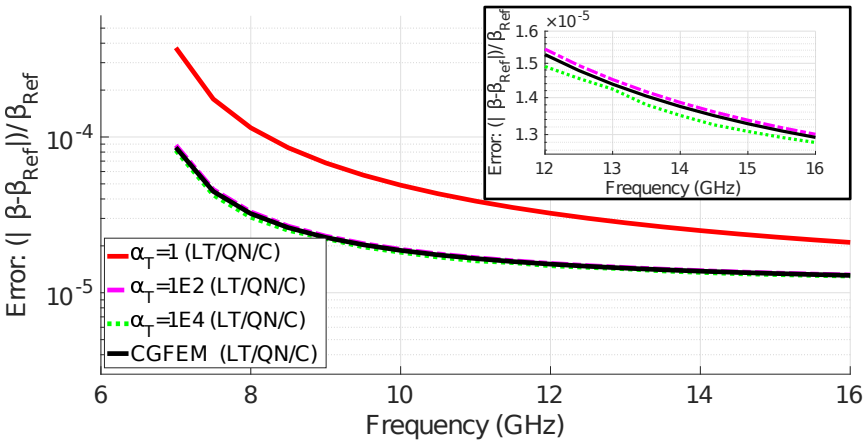

(b)

Figure 3.5: Dominant mode β error for the Rectangular waveguide, the relative error is presented in a logarithmic scale. (a) IPDG/FEM for several α_t values. (b) IPDG/FEM with large α_t values in comparison with the CGFEM.

Overall, it was observed that the precision of the IPDG/FEM is superior to that of the CGFEM for a suitable α_T, both in terms of the mesh size and the number of degrees of freedom. This can be appreciated in Fig. 3.6 for this homogeneous waveguide. In this plot the α_T parameter was linearly varied between 500 and 5000, while the mean edge length l_e is also linearly swept between 0.5 mm and 2.5 mm. One can see that as the number of DoF is increased, the IPDG/FEM tend to outperform the CGFEM with slightly more accurate solutions. An impressive result appears: for highly refined meshes the IPDG/FEM outperforms the CGFEM significantly.

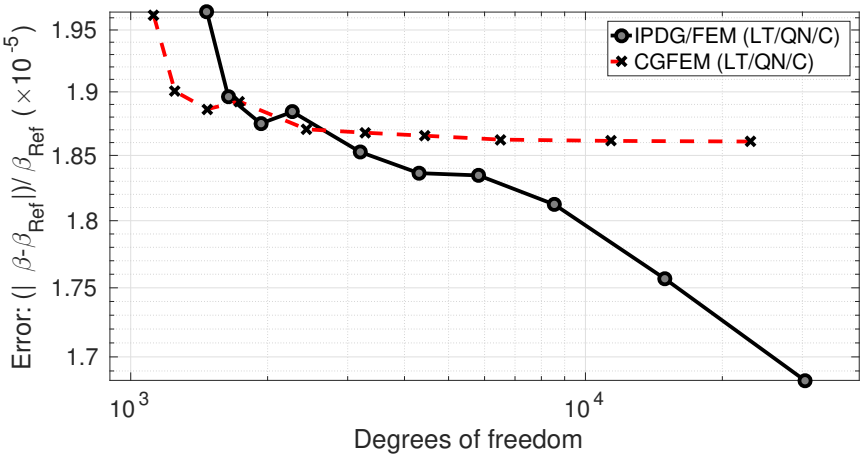

Figure 3.6: Comparative relative error convergence for the Rectangular Waveguide as the number of degrees of freedom is increased when $f = 10$ GHz. The superior performance of the IPDG/FEM over the CGFEM is impressive and more significant for refined meshes.

Chapter 4

Results with the IPDG/FEM

In this chapter the novel modal analysis scheme presented in this dissertation is finally tested and compared to other FEM approaches discussed in the Section 2.2. The tests include standard microwave and optical waveguides, waveguides with lossy dielectrics, leaky optical waveguides and also plasmonic waveguides. Noteworthy is the analysis of some benchmark waveguides that are quite challenging. Again, several results that are shown here are also given in [1].

4.1 Microwave waveguides

This section is focused on results for waveguides operating at microwave frequencies, namely the rectangular waveguide with a hole and another rectangular waveguide with a lossy dielectric. In the first case, the holed waveguide, it is shown that the IPDG/FEM is capable of dealing with non-convex domains, which is expected since in this method the $\boldsymbol{H}(\text{curl};\Omega)$ vectorial space is truly approximated with the edge elements. And for the waveguide with a lossy dielectric the efficiency of the method to analyze inhomogeneous structures is proven. Moreover, this inhomogeneous waveguide was analyzed with a lossy dielectric, proving that the proposed method can calculate the complex propagation constant appropriately.

4.1.1 Non-convex domain

The simulation of the Rectangular waveguide with a hole from the Sub-Section 2.3.2 was repeated using the IPDG/FEM (setting $\alpha_T = 500$ and with the same 1104 LT/QN/C elements at $f = 12\,\text{GHz}$). This setup yields $\beta = 198.49$. This value is consistent with the convergence analysis performed with the adaptive mesh refinement process from the Ansys HFSS and the previous results from the CGFEM. The Fig. 4.1 shows the absolute field solution from the IPDG/FEM in comparison with the CGFEM (repeated to ease the comparison).

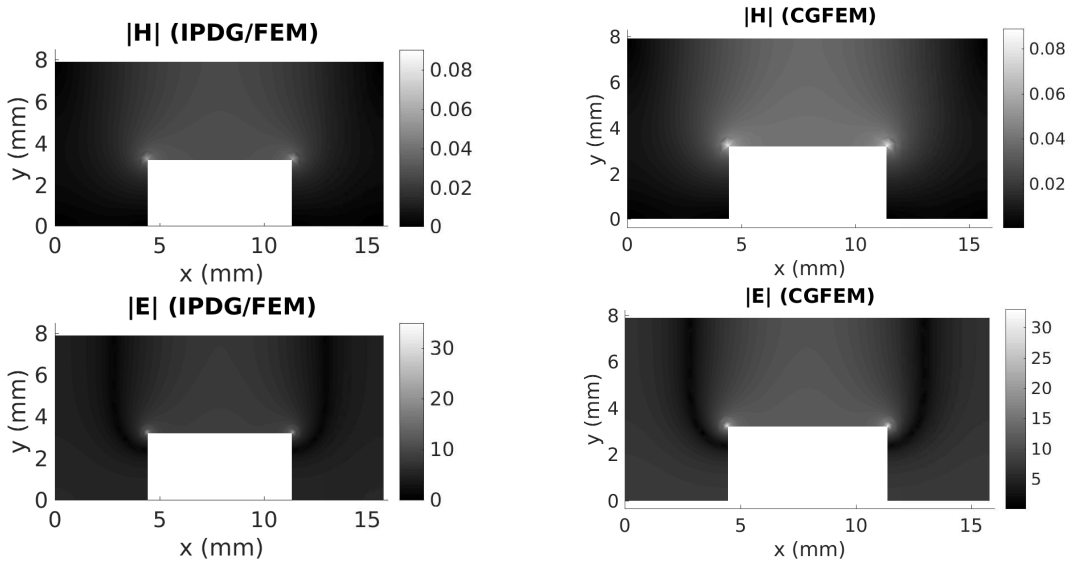

(a) IPDG/FEM (b) CGFEM

Figure 4.1: Absolute electric and magnetic fields of rectangular waveguide with a hole (non-convex domain) operating at 12 GHz. (a) the solution with the IPDG/FEM (a) the solution with the CGFEM (repeated).

In the Fig. 4.2 the dispersion of this waveguide in a wide frequency range is presented also in comparison with the CGFEM. The results are under a nice agreement and a first higher order mode is seen for $f \geq 16\,\mathrm{GHz}$.

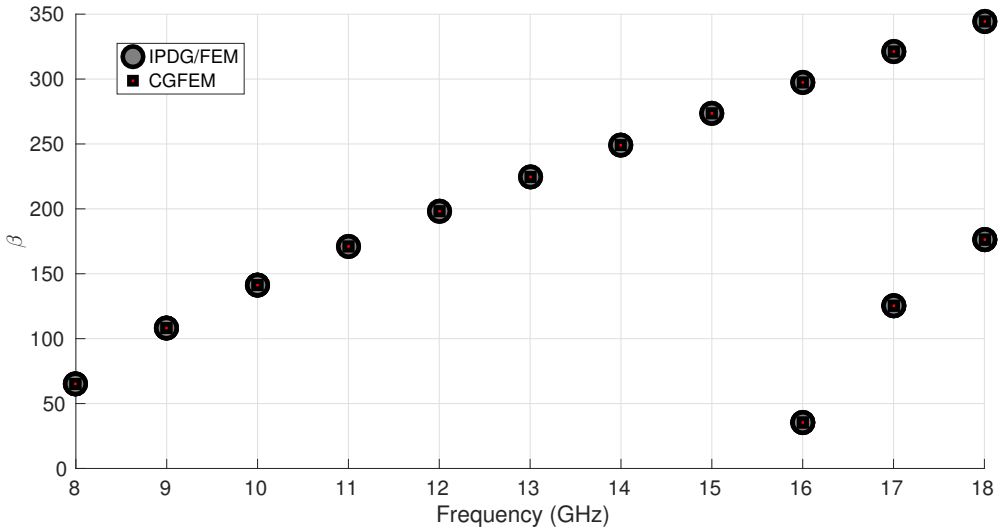

Figure 4.2: Dispersion relation in a wide frequency range for the rectangular waveguide with a hole obtained from the IPDG/FEM and the CGFEM.

4.1.2 Inhomogeneous and lossy waveguide

An inhomogeneous structure is built with the same Rectangular waveguide under test, but now the hole was replaced by a dielectric with a permittivity of $\epsilon_r = 9 - j0.01$. The IPDG/FEM was used with $\alpha_T = 100$ and a mesh of 968 LT/QN/C elements at $f = 12\,\text{GHz}$. For this case the fundamental mode was found to have $\beta = 515.13 - j0.5201$. In the HFSS [63] the dominant mode propagation constant was found to be $\beta = 514.32 - j0.4976$. The magnetic field obtained from both solvers is presented in Fig. 4.3.

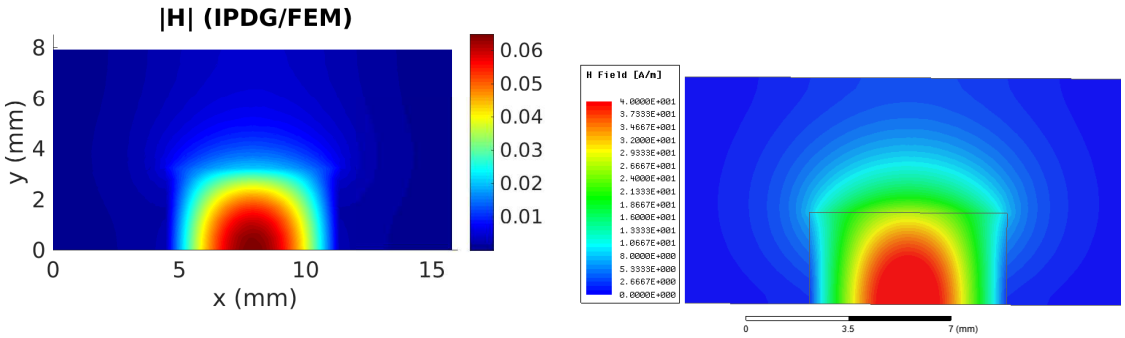

(a) IPDG/FEM (b) HFSS

Figure 4.3: Absolute magnetic fields of the loaded rectangular waveguide with a lossy dielectric operating at 12 GHz. (a) the solution with the IPDG/FEM (a) the solution with the HFSS commercial software.

A difference can be seen in the modal field from the IPDG/FEM and the port field from the HFSS, which is probably due to the non-converged port solution from the commercial solver. The HFSS was configured to perform an adaptive mesh refinement with 19 passes and a Delta S value of 10^{-6} while using a second order basis. However, as shown in Fig. 4.4, the port solution did not converged in the adaptive refinement.

4.2 Optical Waveguides

In this section a discussion on the analysis of some challenging optical waveguides is given. Usually these waveguides required a lot of effort from the electromagnetics community. There are several seminal works on waveguide analysis that were developed to solve the optical waveguides, for instance [39, 41, 43, 45, 46, 48, 56, 60]. In the introduction (Section 1.2) some points on the importance of the analysis of optical waveguides were presented.

The main problems in optical waveguides are the open-space condition and the high index contrast due to the adopted materials. In this high index contrast the light is usually strongly confined and the fields can assume unique profiles. In the IPDG/FEM this contrast is not a problem due to the discontinuous approximation.

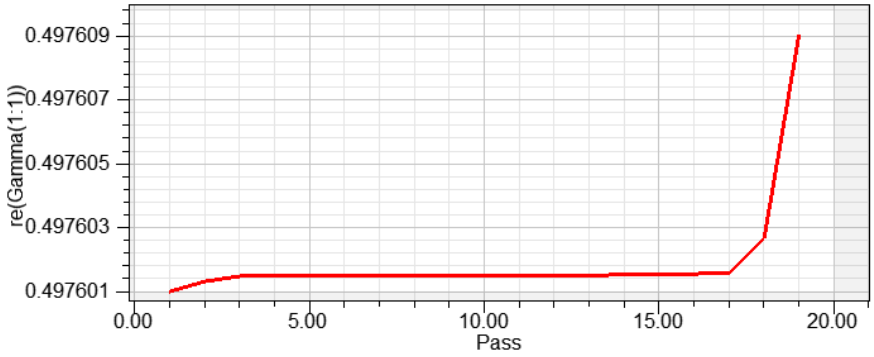

(a)

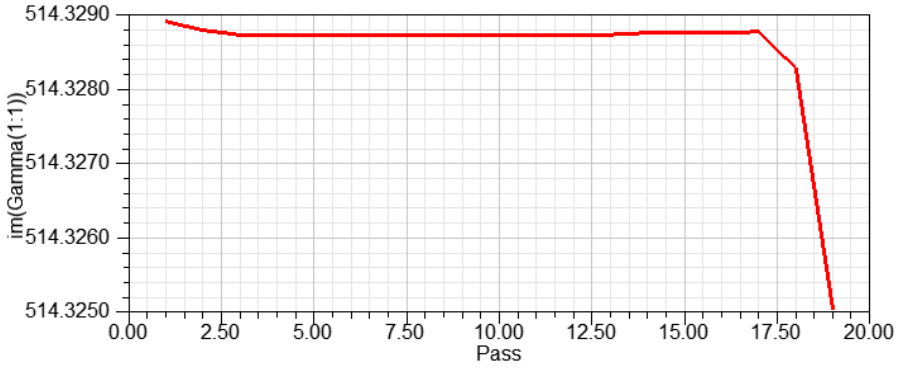

(b)

Figure 4.4: Propagation constant from the HFSS during the adaptive mesh refinement process. (a) the imaginary part of β and (b) the real part of β.

With regards to the first problem, the open-space, a special treatment is mandatory. In the optical regime, a correct modeling of a waveguide requires the computational domain to emulate the open-space boundary, as the optical waveguides are not closed by conductors. This problem has driven a lot of development in the computational electromagnetics. For instance, in [79] the supervisor of this dissertation tackled this issue with a non-linear eigenvalue problem. On the other hand, a consolidated solution in the literature is the use of the PML materials at the outer domain of the waveguide problem [59,60]. This last solution, described in the Sub-Section 2.2.5, was directly applied to the IPDG/FEM scheme.

In the not-so-numerous examples provided here, the efficiency of the present method is shown for this hard and practical problem. For this some practical waveguides were analyzed. Also, some benchmarks that the optical community usually use to validate the computational methods were studied.

4.2.1 Rib Waveguide

The classical rib waveguide, an important benchmark case studied in the works [42,45,64,80], is used as a first test problem here. This device is shown in Fig. 4.5 and

it was analyzed with both the proposed IPDG/FEM and the CGFEM. The wavelength operation was set to $\lambda_0 = 1.15\,\mu$m. The material indexes are $n_{air} = 1$, $n_c = 3.44$, $n_b = 3.44$, and $n_s = 3.4$. The dimensions were set to $w = 3\,\mu$m, $h_1 = 0.5\,\mu$m, $h_2 = 0.5\,\mu$m and $S = D = R = 2\,\mu$m. A PML with $\sigma_{max} = 10^8$, a length of λ_0 and bounded by PMC's was included in the domain, which is visible in the waveguide figure.

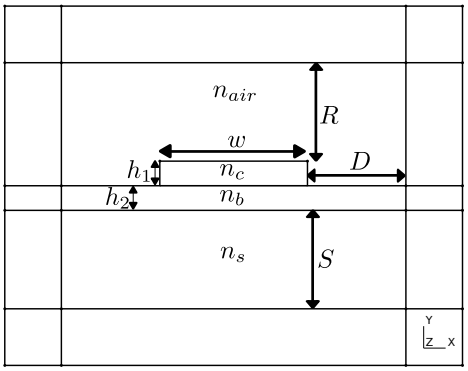

Figure 4.5: Rib waveguide cross-section with its dimensions. The outer rectangles are the PML layers.

A mesh of 8582 LT/QN/C elements with minimum element sides of about 75 nm was used. Then, three modes were found and the obtained $n_{eff} = \beta/k_0$ for a set of α_t values are detailed in the Table 4.1. For all of the α_t values no spurious solutions were found. The table also presents the error ($|n_{eff} - n_{effRef.}|/n_{eff}$) in comparison to the reliable reference values ($n_{effRef.}$) of the Quasi-TE (Mode 1) and Quasi-TM (Mode 2) modes from [64]. The results agree very well with the reference values for at least 6 digits for the n_{eff}. As α_T is increased the error is slightly reduced and is smaller than that of the CGFEM, as expected from our investigation on α_T detailed in the Sub-Section 3.5.3. Since the mesh is quite coarse, setting $\alpha_T = 1$ is still acceptable and does not introduce problems in the eigenvalue problem solution.

Table 4.1: $n_{eff} = \beta/k_0$ for the Rib Waveguide with $w = 3\,\mu m$, $h_1 = 0.5\,\mu m$, $h_2 = 0.5\,\mu m$ and $R = 2\,\mu m$

	Mode 1 (Relative Error)	Mode 2 (Relative Error)	Mode 3
IPDG α_t =1E-3	3.413136006 + 1.04E-12i (1.131E-6)	3.411607870 + 7.51E-13i (9.131E-8)	3.402368789 - 1.46E-12i
IPDG α_t =1E-2	3.413136008 + 1.60E-14i (1.132E-6)	3.411607895 - 3.58E-14i (8.412E-8)	3.402368811 - 6.74E-13i
IPDG α_t =1	3.413135019 + 3.77E-14i (8.424E-7)	3.411608201 - 3.32E-14i (5.65E-9)	3.402367774 - 7.00E-13i
CGFEM	3.413136016 + 1.38E-14i (1.134E-6)	3.411607881 - 3.89E-14i (8.814E-8)	3.402368796 - 6.74E-13i
Ref. [64]	3.413132144 (-)	3.411608182 (-)	-

The calculated electric fields for the Quasi-TE mode are given in Fig. 4.6. One can compare the Fig. 4.6(a) with the one reported in [42] to see that the field solution similarity is good. By looking at the imaginary part of the solutions (the imaginary part of the indexes are leaning towards zero) one can see that this waveguide is not of a leaky kind, this is confirmed in the field solution.

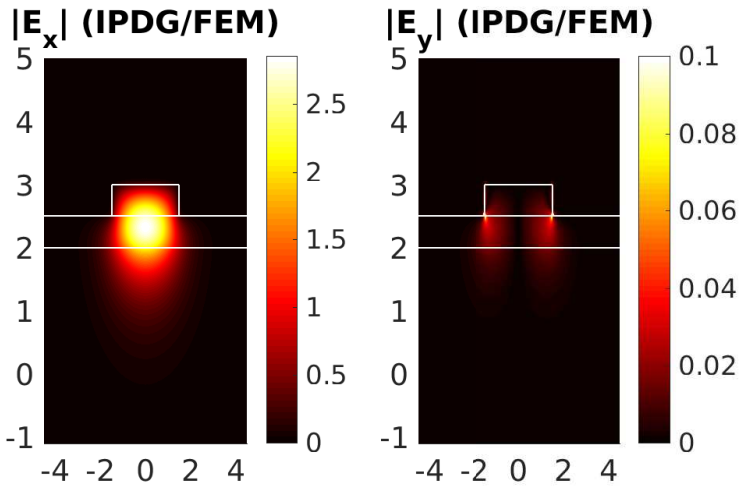

(a)

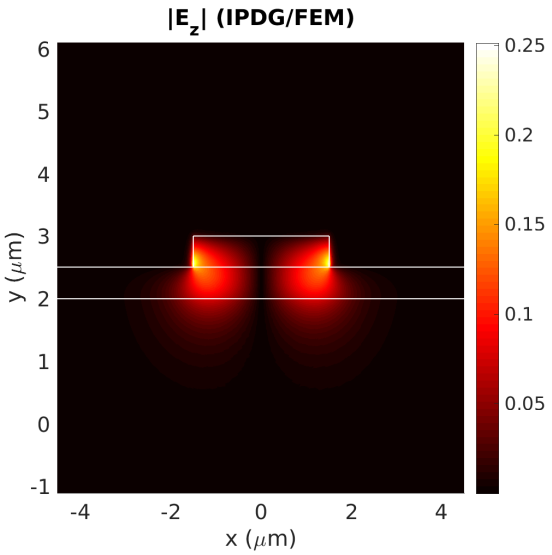

(b)

Figure 4.6: Transverse electric fields 2D distributions for the Quasi-TE mode of the rib waveguide solved with the IPDG/FEM. (a) transverse fields and (b) axial field.

4.2.2 Strip Waveguide (Leaky Mode)

The analysis of the conventional strip waveguide (photonic wire) operating at $\lambda_0 = 1.55\,\mu$m from the Sub-Section 2.3.3 under a leaky mode condition was repeated with the IPDG/FEM. This waveguide can also be illustrated by the Fig. 4.5, but now the layer of height h_1 and width w is made of silicon ($n_c = 3.5$) mounted on a SiO_2 ($n_b = 1.45$) buffer of height h_2, both above an underlying layer of height S also made of silicon ($n_s = 3.5$), in which the air cladding is kept. When the underlying silicon layer is included in the modal analysis, it is known that the fundamental mode is leaky and the correct calculation of n_{eff} is cumbersome due to its tiny imaginary part. This waveguide is a nice benchmark to evaluate leaky modes and it was rigorously studied in [64–66]. In the analysis presented

here, the dimensions were set to $S = 2\,\mu$m, $D = R = h_2 = 1\,\mu$m, $w = 500\,$nm, $h_1 = 220\,$nm, in order to aim for the same leaky mode as in those references.

To catch the leaky condition an analysis of the convergence of the imaginary part of the n_{eff} in relation to the PML parameter σ_{max} was performed. For this this absorbing layer thickness was set to λ_0 and used a coarse mesh of 9964 LT/QN/C elements, which is shown in Fig. 4.7(a). The convergence of Imag$\{n_{eff}\}$ is shown in Fig. 4.7(b), and following the convergence its parameters were set to $\sigma_{max} = 5 \times 10^{16}$ with a cubic conductivity profile ($m = 3$).

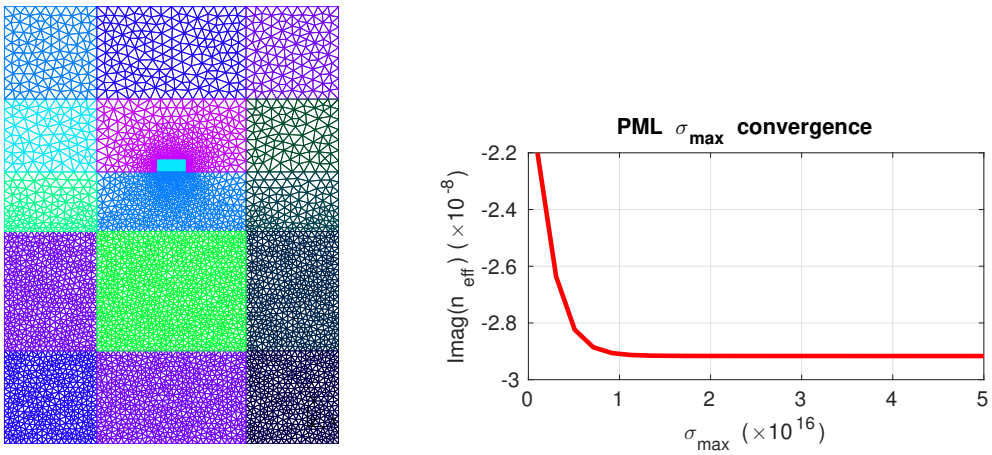

(a) (b)

Figure 4.7: Convergence of the Imag$\{n_{eff}\}$ in relation to the parameter σ_{max}. (a) mesh used for this analysis, (b) convergence.

In addition, another convergence study for the PML in this waveguide was conducted to assess how much the height of the silicon buffer layer modifies the Imag$\{n_{eff}\}$. In the references [64–66] this height was set to $S = 2\,\mu$m, however in the IPDG/FEM it is important to check the effect of the PML distance from to the waveguide core. For doing so the dimension S was swept from $0.42\,\mu$m to $2.5\,\mu$m and the Imag$\{n_{eff}\}$ was evaluated. In this study the mesh inside the waveguide core was built with elements sides of about 60 nm to use a coarse mesh and therefore α_T was set to 5×10^{-2}. The convergence study is shown in Fig. 4.8(b) and the used mesh when $S = 1\,\mu$m is depicted in Fig. 4.8(a). From the convergence it can be concluded that setting $S = 2\,\mu$m is adequate to account for the leakage in this waveguide with the PML, as expected from the aforementioned references.

Then, the mesh was updated to 17392 LT/QN/C elements with minimum element sides of 30 nm at the core silicon layer. In this case α_T was set to 10^{-3}. The fundamental Quasi-TE mode was then found to have an effective index of $2.41234170 - j2.9155475 \times 10^{-8}$. This value is quite consistent with the reliable ones reported in [64–66]. Specifically, the Imag$\{n_{eff}\}$ is close to the values reported in these references. On the other hand, the real part of n_{eff} agrees in 5 digits with the results from [66].

Finally, the analysis was repeated for different meshes (measured by the edge

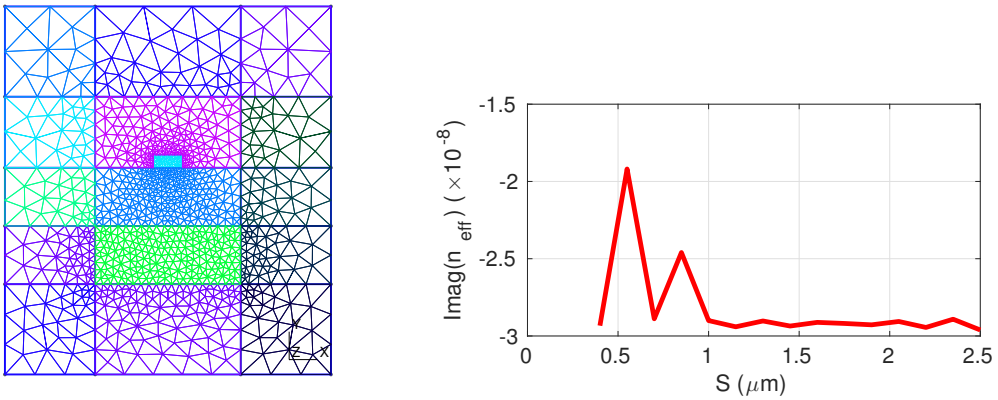

(a) (b)

Figure 4.8: Convergence of the Imag$\{n_{eff}\}$ in relation to the silicon buffer layer height S. (a) the mesh used for this analysis, (b) the actual convergence.

sizes at the silicon core) and α_T values. The results are shown in the Table 4.2. The results are oscillating around a mean index of $n_{eff} = 2.41234746 - j2.91534078 \times 10^{-8}$. The results here are in a great compliance with the reference ones, but a more refined mesh is too time consuming to achieve the perfect matching with the well accepted value from the CAMFR free-software from [65].

Table 4.2: n_{eff} for the Strip Waveguide with $S = 2\,\mu m$, $D = R = h_2 = 1\,\mu m$, $w = 500\,nm$, $h_1 = 220\,nm$

l_e at core	α_T	n_{eff} (Quasi-TE)
40 nm	1.45×10^{-3}	$2.41235185 - j2.9167883 \times 10^{-8}$
35 nm	1.225×10^{-3}	$2.41234711 - j2.9149351 \times 10^{-8}$
30 nm	10^{-3}	$2.41234170 - j2.9155475 \times 10^{-8}$
25 nm	7.75×10^{-4}	$2.41234462 - j2.9148570 \times 10^{-8}$
20 nm	5.5×10^{-4}	$2.41235199 - j2.9145758 \times 10^{-8}$

In Fig. 4.9 the 1D profile of the dominant field E_x along the middle of the waveguide is depicted for the fundamental Quasi-TE mode for the $l_e = 30\,\text{nm}$ case. The PML layer is at the $y < 0$ region, and the field absorption due to the PML is visible in this figure. The underlying silicon layer is at the $0 < y < 2$ region. The oscillatory leaky field behavior is well captured with the present IPDG/FEM. The oscillation frequency matches with the same plot presented in [66]. Additionally, the 2D profile for the E field are given in Fig. 4.10 for the $l_e = 30\,\text{nm}$ simulation.

4.2.3 Trapezoidal Waveguide

Finally, as a last example the trapezoidal waveguide was analyzed, which is another challenging device that was only solved with accurate methods in [50] and in [81]. This structure is shown in Fig. 4.11, it comprises a dielectric/magnetic core embedded in

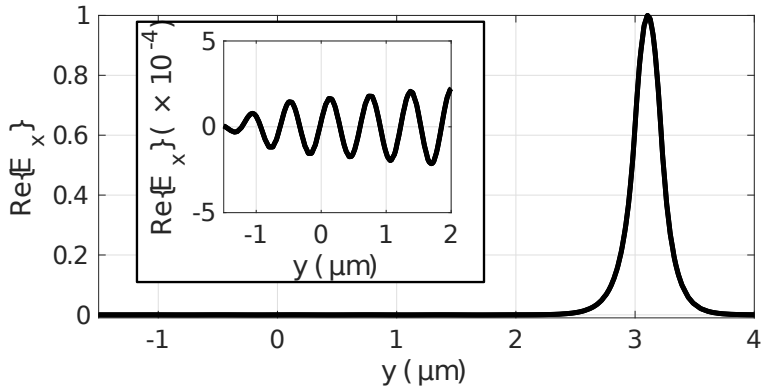

Figure 4.9: Photonic wire E_x 1D field profile at the middle of the waveguide. The leaky mode characteristics is detailed in the zoomed plot inside the figure.

an air layer. In this figure the outer boxes are the PMLs. To increase the field jumps at the interfaces, the analyzed waveguide was the one with the core material having $\epsilon_r = \sqrt{8}$ and $\mu_r = \sqrt{8}$.

The analysis was performed at $\lambda_0 = 1.5\,\mu$m with the dimensions from [81], *i.e.* $a = 1\,\mu$m, $b = a/\sin(5\pi/9)$ and $c = a(1 + 2\tan(\pi/18))$, and with an added PML of $0.7\lambda_0$ thickness. Using LT/QN/C elements and without any special treatment excellent results were obtained. Again comparative results are presented between the IPDG/FEM and the CGFEM with relative errors from the reference values reported in [81]. See the Table 4.3 with the results for the fundamental mode (the imaginary part was below 10^{-14} for all cases and it is not shown in the table) for some values of mean core edge length (l_e) and α_T. The α_T in the three IPDG/FEM simulations was: 5×10^{-4} ($l_e = 30\,$nm), 5.25×10^{-4} ($l_e = 35\,$nm) and 5.5×10^{-4} ($l_e = 40\,$nm). For all of these cases the IPDG/FEM relative error was smaller than that of the CGFEM.

Table 4.3: Comparative n_{eff} for the Trapezoidal Waveguide operating at $\lambda_0 = 1.5\,\mu m$ with $a = 1\,\mu m$, $b = a/\sin(5\pi/9)$ and $c = a(1 + 2\tan(\pi/18))$. Core material: $\epsilon_r = \mu_r = \sqrt{8}$

l_e at core	IPDG/FEM (Relative Error)	CGFEM (Relative Error)
30 nm	2.6707582959 (4.15E-8)	2.6707585002 (1.18E-7)
35 nm	2.6707584759 (1.09E-7)	2.6707587157 (1.99E-7)
40 nm	2.6707587916 (2.27E-7)	2.6707589431 (2.84E-7)

In this waveguide the advantage of the IPDG/FEM over the CGFEM is relevant and a better field solution was observed with the IPDG/FEM when the mesh mean edge length at the core was set to 30 nm. In the Fig. 4.12 the transverse magnetic field of the IPDG/FEM and the CGFEM are plotted. While the main field H_y is apparently the same on both methods, the H_x field is better captured with the IPDG/FEM. This explains the slightly greater index for the CGFEM. For more refined meshes this field difference was not observed.

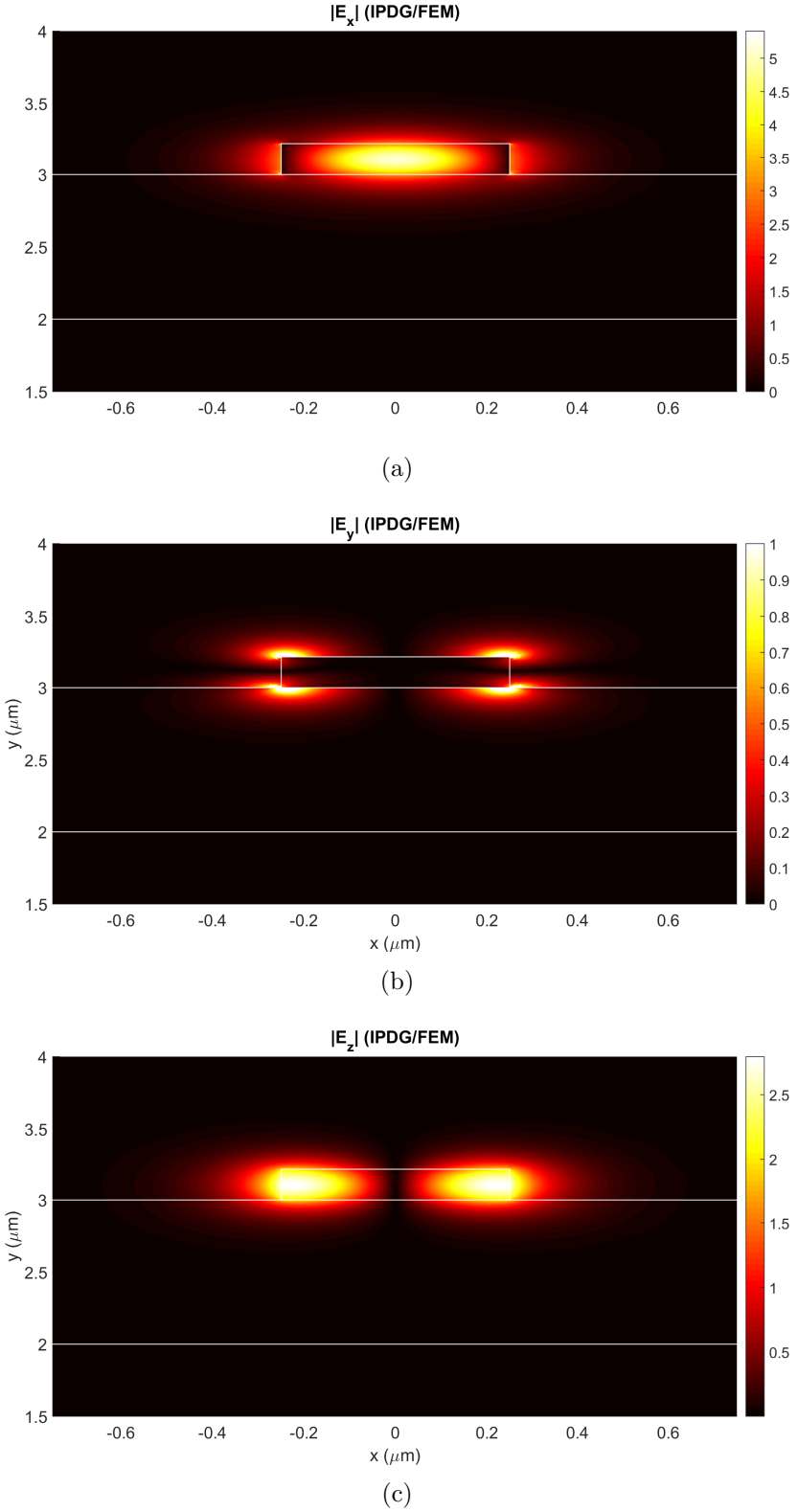

(a)

(b)

(c)

Figure 4.10: Photonic wire 2D E field profile: a) $|E_x|$, b) $|E_y|$, c) $|E_z|$.

4.3 Plasmonic Waveguides

In this section the analysis of two plasmonic waveguides is discussed. If optical waveguides are cumbersome, dealing with plasmonics can be even harder. The plasmonic

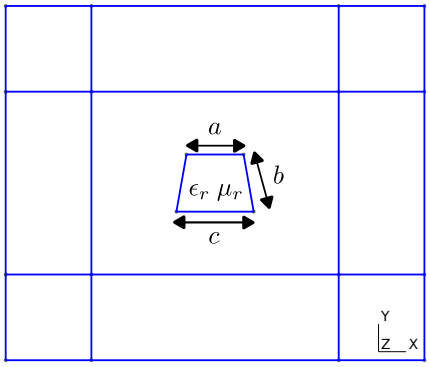

Figure 4.11: Geometry of the trapezoidal waveguide embedded in air and bounded by PMLs.

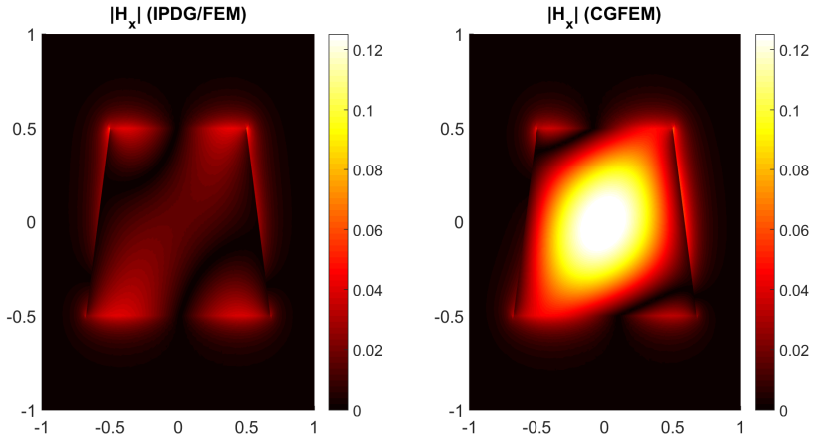

(a)

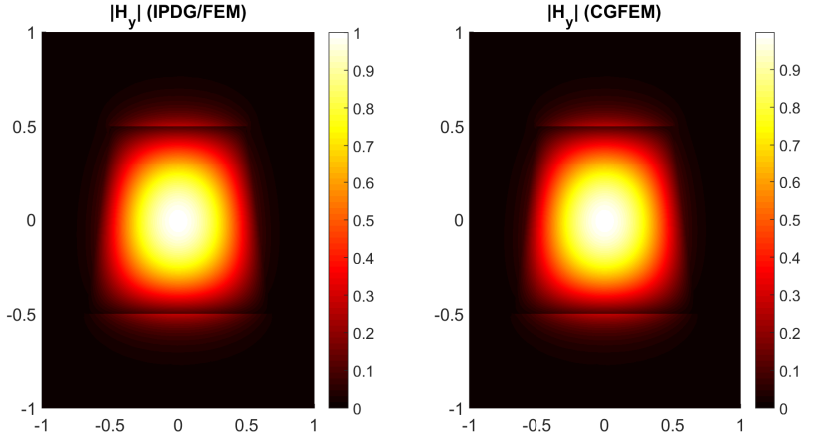

(b)

Figure 4.12: Comparison between the IPDG/FEM and the CGFEM transverse magnetic field profiles for the trapezoidal waveguide. The core material have $\epsilon_r = \sqrt{8}$ and $\mu_r = \sqrt{8}$ and the mesh mean edge length at the core is set to 30 nm,. (a) H_x, (b) H_y.

waveguides rely on metal-dielectric interfaces, which results in fields with strong singularities that are hard to approximate. In addition, the intense fields on plasmonics implies in a

lossy propagation condition. The losses in the plasmonic modes are rather important and must be well calculated. For all of these issues the method proposed in this dissertation is quite appropriate due to its already mentioned advantages. In the following the analysis of two waveguides that supports plasmonic modes are presented.

4.3.1 DLSPP Waveguide

The dielectric-loaded surface plasmon-polariton (DLSPP) waveguide has been throughly studied in [25]. It comprises a dielectric ridge (polymer) above a thin gold layer with air cladding and a thick dielectric substrate. This structure supports a confined surface plasmon-polariton lossy wave at the metal-ridge interface. The waveguide is detailed in Fig. 4.13(a). The DLSPP with $d = 100\,\text{nm}$, $w = 600\,\text{nm}$ and $t = 600\,\text{nm}$, operating at $\lambda_0 = 1.55\,\mu\text{m}$, was analyzed with both the proposed IPDG/FEM and the CGFEM. The material properties are $n_{air} = 1$, $n_p = 1.535$, $n_s = 1.6$ and $n_{Au} = 0.55 - i11.5$ (lossy metal).

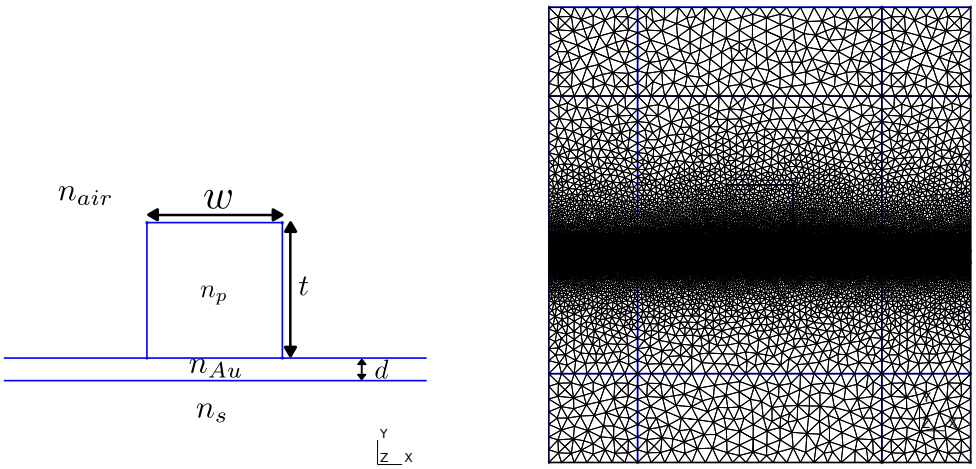

Figure 4.13: DLSPP waveguide cross-section with its (a) dimensions and (b) mesh.

An extremely refined mesh with 32100 LT/QN/C elements shown in Fig. 4.13(b) was used, in which the gold layer elements had sides of about 10 nm. Due to this small sized elements, for this problem the penalty parameter was set to $\alpha_t = 10^{-4}$. The PML thickness was set to $1\,\mu\text{m}$ and it was bounded by PMC. For the IPDG/FEM the fundamental TM_{00} mode had $\text{Re}\{n_{eff}\} = 1.2912$ and a propagation length $L = 1/(-2\text{Im}\{\beta\}) = 44.02\,\mu\text{m}$, while for the CGFEM the same values were found. The solution matches well with those ones reported in [25, 82]. In Fig. 4.14 the $|E|$ 2D field profiles from the IPDG/FEM method are depicted. Observe that the E_x is subjected to a less intense attenuation at the metal layer. Additionally, the plot from [25] is reproduced in Fig. 4.15, which presents the E_y field at the vertical profile of the waveguide obtained with the IPDG/FEM and the

CGFEM. Note the exponential field decay at the metal layer and the field fluctuation at the substrate, exposing the mode leakage.

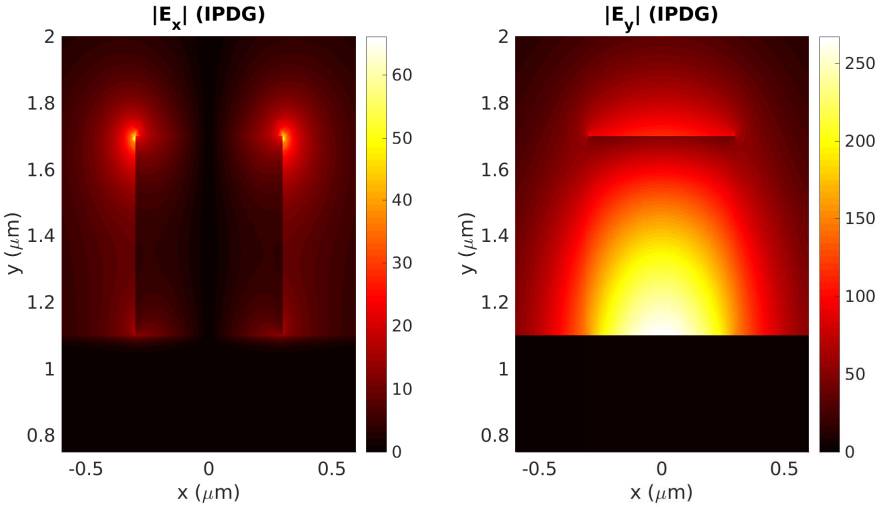

Figure 4.14: DLSPP $|E_x|$ and $|E_y|$ 2D field profiles calculated with the IPDG/FEM.

4.3.2 SPS Waveguide

And finally, to increase the proof of efficiency in plasmonics the surface plasmon stripe waveguide (SPSWG) was analyzed operating at $\lambda_0 = 1.15\,\mu$m, with the IPDG/FEM. This waveguide shows a unique leaky condition due to its metal-dielectric interface. This structure was thoroughly studied in [83]. Indeed, the structure of this waveguide is simple: it comprises a small metal strip of height h and width W above a dielectric substrate and with air cladding. For the plasmonic mode to exist, this metal strip is quite thin, *i.e.* $h = 55\,$nm and $W = 3.7\,\mu$m. This waveguide meshed with an extremely refined mesh is shown in Fig. 4.16.

The solution of this plasmonic waveguide was done with 13417 elements, which results in only 166536 unknowns (much less than the 638347 reported in [83]). The mean mesh edge length at the metal stripe is about 20 nm. Then it was found $n_{eff} = 1.01604 - 0.00338j$ for the Quasi-TM_1 mode. With this mesh the field and the n_{eff} were calculated with excellent precision. Both the index and the fields are matching well with the solution reported in [83]. The leaky field profile is depicted in Fig. 4.17. Note that in the H_x field five dips can be seen at the substrate right below the metal stripe. At the metal lateral edges, near the metal-air-dielectric points, the strong field singularities are the sources for the leaky fields.

An unconventional behavior of the SPSWG is how the first modes hold some local-overshoot due to the aforementioned field singularities and dips at the metal-dielectric interfaces. To reproduce this strange characteristics a highly accurate mode solver is required [42]. For doing so, it was performed a sweep on the stripe width W to see if

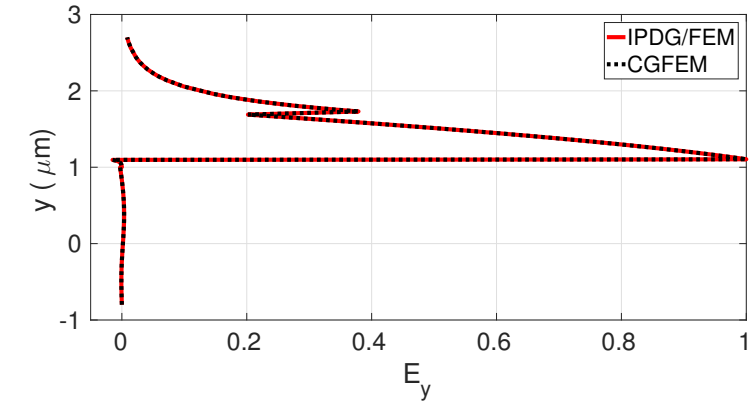

(a)

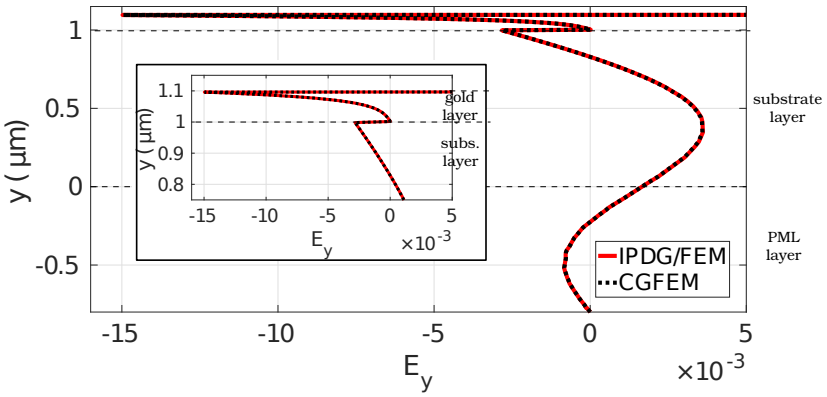

(b)

Figure 4.15: DLSPP Re$\{E_y\}$ field profile calculated with the IPDG/FEM along the middle of the waveguide. The dashed horizontal lines indicate the material interfaces. The gold-polymer interface is located at $y = 1.1\,\mu$m and the gold-substrate interface is at $y = 1\,\mu$m. (a) large plot, (b) detailed view at the main interfaces with a zoom at the gold-substrate interface field .

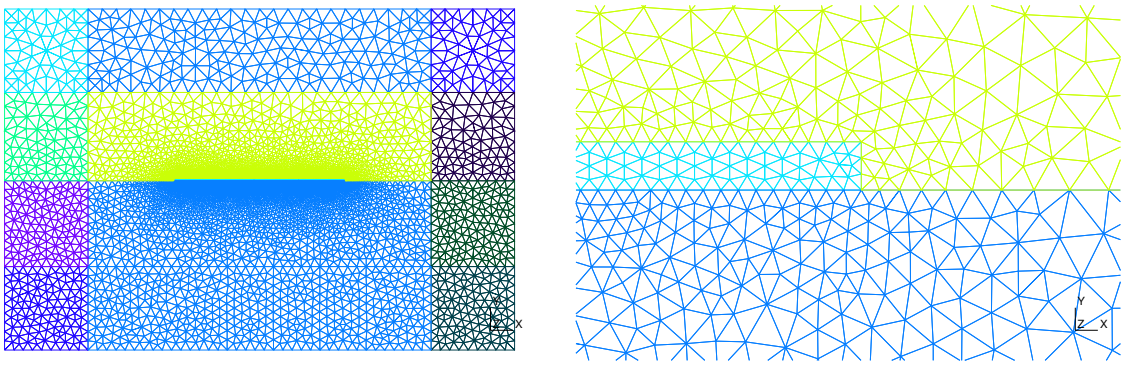

(a) (b)

Figure 4.16: SPSWG cross-section with a refined meshed of 13417 elements. (a) general view showing the PML boxes and (b) zoom at the metal dielectric interface.

the IPDG/FEM would be able to capture this on this relatively coarse mesh. The results

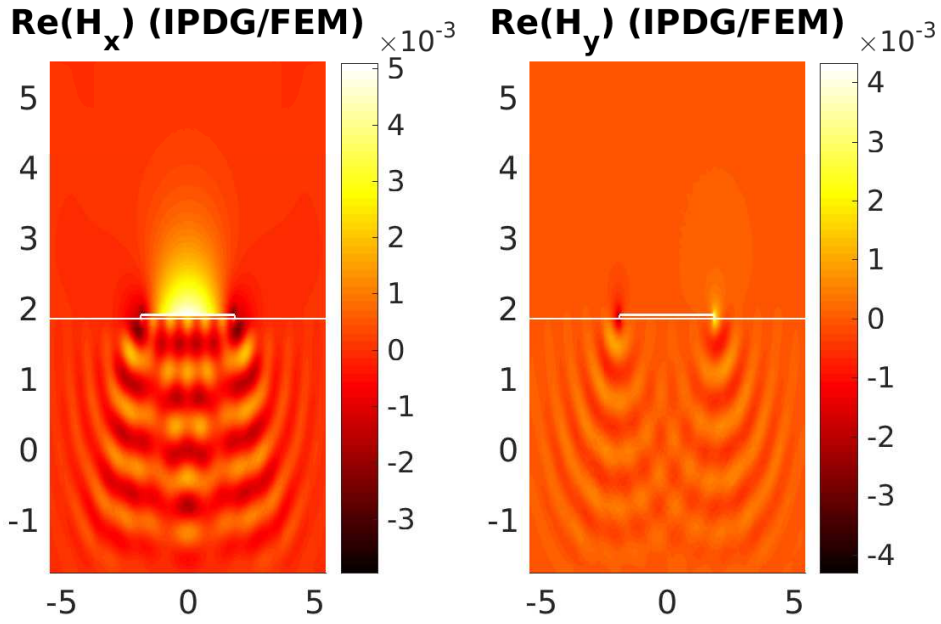

(a)

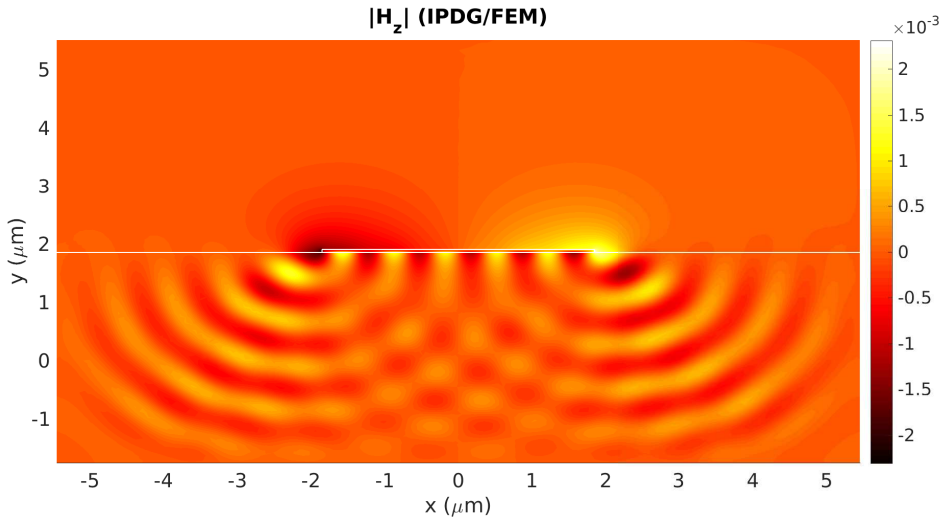

(b)

Figure 4.17: Quasi-TM_1 mode magnetic field 2D distributions for the SPSWG calculated with the IPDG/FEM: (a) the transverse fields (b) the axial field.

are presented in Fig. 4.18, where one can sees that capture this property was adequately captured.

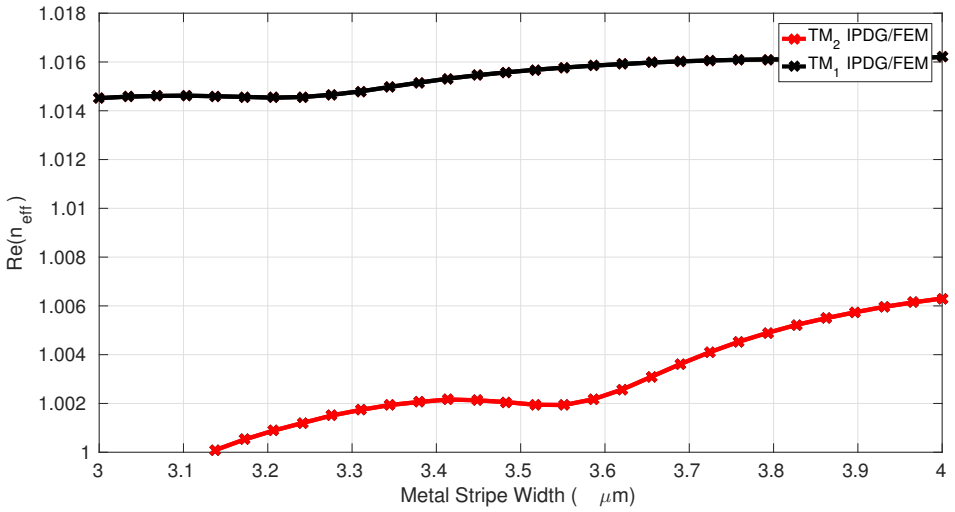

(a)

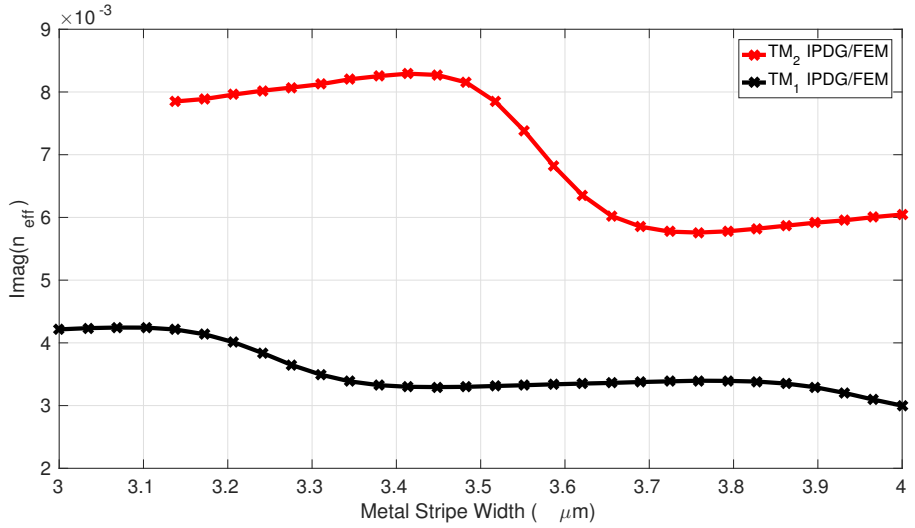

(b)

Figure 4.18: Quasi-TM_1 and Quasi-TM_2 modes indexes local-overshoots captured by the IPDG/FEM when the metal stripe width is varied: (a) Real$\{n_{eff}\}$ (b) Imag$\{n_{eff}\}$.

Chapter 5

Conclusion

The DG methods are promising since they incorporate the properties of the CGFEM while adding several advantages such as: handling of unstructured complex meshes which might comprise elements with distinct orders and shapes, appropriate modeling of material discontinuities and field singularities, and it can lead to diagonal matrices useful for time/space marching methods. Seeking to explore these advantages, in this dissertation a novel numerical approach was developed to analyze waveguides by combining the IPDG with the conventional FEM to solve the second order time-harmonic Maxwell's equation. The solution of open waveguides was accomplished with the help of PMLs. Albeit the computational problem is increased in the IPDG/FEM method when compared to the CGFEM, the computational cost increment is subtle and in all of the discussed examples a precision improvement was observed. The present method avoids spurious solution by setting an appropriate value for the penalty function, while the null ones ($\beta = 0$) can be easily identified.

Several waveguides under distinct conditions were successfully analyzed to prove the efficiency and accuracy of the proposed method. These tests included lossy, leaky and plasmonic waveguides. The main contributions of this work are: a robust application of the IPDG method for waveguide analysis, the proposal of a new penalty function and an investigation of its associated penalty parameter. The proposed novel approach results in a combined IPDG/FEM scheme, including PMLs, for the accurate modal analysis of open or shielded waveguides.

This dissertation is focused on introducing this new method and evaluating its accuracy for intricate waveguides. Many of the advantages of the of the IPDG, such as different elements handling, were kept unexplored. However, they will be investigated in detail in future works. In addition, it is expected that the present research can lead to robust explicit time/space marching schemes, which is currently being studied and will be presented in a future work.

References

[1] L. Andrade-Fonseca and H. E. Hernandez-Figueroa, "Full-wave interior penalty discontinuous galerkin method for waveguide analysis," *Journal of Lightwave Technology*, vol. 36, pp. 5168–5176, Nov 2018.

[2] J. C. Maxwell, *A treatise on electricity and magnetism*, vol. 1. Clarendon press, 1881.

[3] J.-M. Jin, *The finite element method in electromagnetics*. John Wiley & Sons, 2002.

[4] J. L. Volakis, A. Chatterjee, and L. C. Kempel, *Finite element method electromagnetics: antennas, microwave circuits, and scattering applications*, vol. 6. John Wiley & Sons, 1998.

[5] A. Taflove and S. C. Hagness, *Computational electrodynamics*. Artech house, 2005.

[6] S. Descombes, C. Durochat, S. Lanteri, L. Moya, C. Scheid, and J. Viquerat, "Recent advances on a dgtd method for time-domain electromagnetics," *Photonics and Nanostructures-Fundamentals and Applications*, vol. 11, no. 4, pp. 291–302, 2013.

[7] J. Viquerat, *Simulation of electromagnetic waves propagation in nano-optics with a high-order discontinuous Galerkin time-domain method*. PhD thesis, Université Nice Sophia Antipolis, 2015.

[8] M. C. König, *Discontinuous Galerkin Methods in Nanophotonics*. PhD thesis, KIT-Bibliothek, 2011.

[9] K. Busch, M. König, and J. Niegemann, "Discontinuous galerkin methods in nanophotonics," *Laser & Photonics Reviews*, vol. 5, no. 6, pp. 773–809, 2011.

[10] S. Dosopoulos and J.-F. Lee, "Interior penalty discontinuous galerkin finite element method for the time-dependent first order maxwell's equations," *IEEE Transactions on Antennas and Propagation*, vol. 58, no. 12, pp. 4085–4090, 2010.

[11] G. Chen, L. Zhao, W. Yu, S. Yan, K. Zhang, and J.-M. Jin, "A general scheme for the discontinuous galerkin time-domain modeling and s-parameter extraction of inhomogeneous waveports," *IEEE Transactions on Microwave Theory and Techniques*, vol. 66, no. 4, pp. 1701–1712, 2018.

[12] J. Alvarez, L. Angulo, A. R. Bretones, and S. G. Garcia, "A spurious-free discontinuous galerkin time-domain method for the accurate modeling of microwave filters," *IEEE Transactions on Microwave Theory and Techniques*, vol. 60, no. 8, pp. 2359–2369, 2012.

[13] J. S. Hesthaven and T. Warburton, *Nodal discontinuous Galerkin methods: algorithms, analysis, and applications*. Springer Science & Business Media, 2007.

[14] W. Zhang, S. Serna, X. Le Roux, L. Vivien, and E. Cassan, "Silicon nanobeam cavity for ultra-localized light-matter interaction," *Optics letters*, vol. 42, no. 17, pp. 3323–3326, 2017.

[15] P. Genevet, F. Capasso, F. Aieta, M. Khorasaninejad, and R. Devlin, "Recent advances in planar optics: from plasmonic to dielectric metasurfaces," *Optica*, vol. 4, no. 1, pp. 139–152, 2017.

[16] R. E. Rubio-Noriega and H. E. Hernández-Figueroa, "Compact low loss vertical coupling for optical transmitters with polymer modulators," *Journal of Lightwave Technology*, vol. 35, no. 24, pp. 5440–5447, 2017.

[17] D. Pérez-Galacho, C. Alonso-Ramos, F. Mazeas, X. Le Roux, D. Oser, W. Zhang, D. Marris-Morini, L. Labonté, S. Tanzilli, É. Cassan, *et al.*, "Optical pump-rejection filter based on silicon sub-wavelength engineered photonic structures," *Optics Letters*, vol. 42, no. 8, pp. 1468–1471, 2017.

[18] P. J. Bock, P. Cheben, J. H. Schmid, J. Lapointe, A. Delâge, S. Janz, G. C. Aers, D.-X. Xu, A. Densmore, and T. J. Hall, "Subwavelength grating periodic structures in silicon-on-insulator: a new type of microphotonic waveguide," *Optics express*, vol. 18, no. 19, pp. 20251–20262, 2010.

[19] R. Halir, A. Ortega-Monux, J. H. Schmid, C. Alonso-Ramos, J. Lapointe, D.-X. Xu, J. G. Wanguemert-Perez, I. Molina-Fernandez, and S. Janz, "Recent advances in silicon waveguide devices using sub-wavelength gratings," *IEEE Journal of Selected Topics in Quantum Electronics*, vol. 20, no. 4, pp. 279–291, 2014.

[20] J. Leuthold, C. Koos, and W. Freude, "Nonlinear silicon photonics," *Nature Photonics*, vol. 4, no. 8, p. 535, 2010.

[21] J. L. Pita, I. Aldaya, P. Dainese, H. E. Hernandez-Figueroa, and L. H. Gabrielli, "Design of a compact cmos-compatible photonic antenna by topological optimization," *Optics express*, vol. 26, no. 3, pp. 2435–2442, 2018.

[22] L. F. Frellsen, Y. Ding, O. Sigmund, and L. H. Frandsen, "Topology optimized mode multiplexing in silicon-on-insulator photonic wire waveguides," *Optics express*, vol. 24, no. 15, pp. 16866–16873, 2016.

[23] J. Grandidier, S. Massenot, G. C. Des Francs, A. Bouhelier, J.-C. Weeber, L. Markey, A. Dereux, J. Renger, M. González, and R. Quidant, "Dielectric-loaded surface plasmon polariton waveguides: figures of merit and mode characterization by image and fourier plane leakage microscopy," *Physical Review B*, vol. 78, no. 24, p. 245419, 2008.

[24] L. Chen, J. Shakya, and M. Lipson, "Subwavelength confinement in an integrated metal slot waveguide on silicon," *Optics letters*, vol. 31, no. 14, pp. 2133–2135, 2006.

[25] T. Holmgaard and S. I. Bozhevolnyi, "Theoretical analysis of dielectric-loaded surface plasmon-polariton waveguides," *Physical Review B*, vol. 75, no. 24, p. 245405, 2007.

[26] G. Wiederhecker, C. M. d. B. Cordeiro, F. Couny, F. Benabid, S. Maier, J. Knight, C. Cruz, and H. Fragnito, "Field enhancement within an optical fibre with a subwavelength air core," *Nature photonics*, vol. 1, no. 2, p. 115, 2007.

[27] V. R. Almeida, Q. Xu, C. A. Barrios, and M. Lipson, "Guiding and confining light in void nanostructure," *Optics letters*, vol. 29, no. 11, pp. 1209–1211, 2004.

[28] M. J. Heck, J. F. Bauters, M. L. Davenport, D. T. Spencer, and J. E. Bowers, "Ultra-low loss waveguide platform and its integration with silicon photonics," *Laser & Photonics Reviews*, vol. 8, no. 5, pp. 667–686, 2014.

[29] L. A. Fonseca, H. E. Hernandez-Figueroa, G. T. Santos-Souza, and L. L. Bravo-Roger, "Dielectric properties characterization: A simple inverse problem approach," in *Numerical Electromagnetic and Multiphysics Modeling and Optimization for RF, Microwave, and Terahertz Applications (NEMO), 2017 IEEE MTT-S International Conference on*, pp. 22–24, IEEE, 2017.

[30] S. M. Saad, "Review of numerical methods for the analysis of arbitrarily-shaped microwave and optical dielectric waveguides," *IEEE transactions on microwave theory and techniques*, vol. 33, no. 10, pp. 894–899, 1985.

[31] K. Chiang, "Review of numerical and approximate methods for the modal analysis of general optical dielectric waveguides," *Optical and Quantum Electronics*, vol. 26, no. 3, pp. S113–S134, 1994.

[32] M. Koshiba, "Optical waveguide theory by the finite element method," *IEICE Transactions on Electronics*, vol. 97, no. 7, pp. 625–635, 2014.

[33] D. Sun, J. Manges, X. Yuan, and Z. Cendes, "Spurious modes in finite-element methods," *IEEE Antennas and Propagation Magazine*, vol. 37, no. 5, pp. 12–24, 1995.

[34] S. Caorsi, P. Fernandes, and M. Raffetto, "On the convergence of galerkin finite element approximations of electromagnetic eigenproblems," *SIAM Journal on Numerical Analysis*, vol. 38, no. 2, pp. 580–607, 2000.

[35] D. Boffi, P. Fernandes, L. Gastaldi, and I. Perugia, "Computational models of electromagnetic resonators: analysis of edge element approximation," *SIAM journal on numerical analysis*, vol. 36, no. 4, pp. 1264–1290, 1999.

[36] F. L. Teixeira, "Time-domain finite-difference and finite-element methods for maxwell equations in complex media," *IEEE Transactions on Antennas and Propagation*, vol. 56, no. 8, pp. 2150–2166, 2008.

[37] K. Saitoh and M. Koshiba, "Full-vectorial finite element beam propagation method with perfectly matched layers for anisotropic optical waveguides," *Journal of lightwave technology*, vol. 19, no. 3, p. 405, 2001.

[38] J. P. da Silva, H. E. Hernández-Figueroa, and A. M. F. Frasson, "Improved vectorial finite-element bpm analysis for transverse anisotropic media," *Journal of Lightwave Technology*, vol. 21, no. 2, p. 567, 2003.

[39] B. Rahman and J. Davies, "Finite-element solution of integrated optical waveguides," *Journal of Lightwave Technology*, vol. 2, no. 5, pp. 682–688, 1984.

[40] K. Hayata, M. Koshiba, M. Eguchi, and M. Suzuki, "Novel finite-element formulation without any spurious solutions for dielectric waveguides," *Electronics Letters*, vol. 22, no. 6, pp. 295–296, 1986.

[41] H. Hernández-Figueroa, F. Fernández, Y. Lu, and J. Davies, "Vectorial finite element modelling of 2d leaky waveguides," *IEEE transactions on magnetics*, vol. 31, no. 3, pp. 1710–1713, 1995.

[42] N. Liu, G. Cai, C. Zhu, Y. Huang, and Q. H. Liu, "The mixed finite-element method with mass lumping for computing optical waveguide modes," *IEEE Journal of Selected Topics in Quantum Electronics*, vol. 22, no. 2, pp. 187–195, 2016.

[43] J.-F. Lee, D.-K. Sun, and Z. J. Cendes, "Full-wave analysis of dielectric waveguides using tangential vector finite elements," *IEEE Transactions on Microwave Theory and Techniques*, vol. 39, no. 8, pp. 1262–1271, 1991.

[44] C.-C. Huang, C.-C. Huang, and J.-Y. Yang, "An efficient method for computing optical waveguides with discontinuous refractive index profiles using spectral collocation

method with domain decomposition," *Journal of lightwave technology*, vol. 21, no. 10, p. 2284, 2003.

[45] G. R. Hadley, "High-accuracy finite-difference equations for dielectric waveguide analysis ii: Dielectric corners," *Journal of lightwave technology*, vol. 20, no. 7, pp. 1219–1231, 2002.

[46] C.-P. Yu and H.-C. Chang, "Yee-mesh-based finite difference eigenmode solver with pml absorbing boundary conditions for optical waveguides and photonic crystal fibers," *Optics Express*, vol. 12, no. 25, pp. 6165–6177, 2004.

[47] A. B. Fallahkhair, K. S. Li, and T. E. Murphy, "Vector finite difference modesolver for anisotropic dielectric waveguides," *Journal of Lightwave Technology*, vol. 26, no. 11, pp. 1423–1431, 2008.

[48] T. Lu and D. Yevick, "A vectorial boundary element method analysis of integrated optical waveguides," *Journal of lightwave technology*, vol. 21, no. 8, p. 1793, 2003.

[49] H. Cheng, W. Crutchfield, M. Doery, and L. Greengard, "Fast, accurate integral equation methods for the analysis of photonic crystal fibers i: Theory," *Optics Express*, vol. 12, no. 16, pp. 3791–3805, 2004.

[50] W. Lu and Y. Y. Lu, "Waveguide mode solver based on neumann-to-dirichlet operators and boundary integral equations," *Journal of Computational Physics*, vol. 231, no. 4, pp. 1360–1371, 2012.

[51] B. C. Correa, E. J. Silva, A. R. Fonseca, D. B. Oliveira, and R. C. Mesquita, "Meshless local petrov-galerkin approach in solving microwave guide problems," *IEEE Transactions on Magnetics*, vol. 47, no. 5, pp. 1526–1529, 2011.

[52] E. Silva, R. Mesquita, R. Saldanha, and P. Palmeira, "An object-oriented finite-element program for electromagnetic field computation," *IEEE transactions on magnetics*, vol. 30, no. 5, pp. 3618–3621, 1994.

[53] C. Geuzaine and J.-F. Remacle, "Gmsh: A 3-d finite element mesh generator with built-in pre-and post-processing facilities," *International journal for numerical methods in engineering*, vol. 79, no. 11, pp. 1309–1331, 2009.

[54] A. Nicolet, S. Guenneau, C. Geuzaine, and F. Zolla, "Modelling of electromagnetic waves in periodic media with finite elements," *Journal of Computational and Applied Mathematics*, vol. 168, no. 1-2, pp. 321–329, 2004.

[55] G. Cowper, "Gaussian quadrature formulas for triangles," *International Journal for Numerical Methods in Engineering*, vol. 7, no. 3, pp. 405–408, 1973.

[56] M. Koshiba and K. Inoue, "Simple and efficient finite-element analysis of microwave and optical waveguides," *IEEE Transactions on Microwave Theory and Techniques*, vol. 40, no. 2, pp. 371–377, 1992.

[57] A. F. Peterson, "Vector finite element formulation for scattering from two-dimensional heterogeneous bodies," *IEEE transactions on antennas and propagation*, vol. 42, no. 3, pp. 357–365, 1994.

[58] J.-C. Nédélec, "Mixed finite elements in r^3," *Numerische Mathematik*, vol. 35, no. 3, pp. 315–341, 1980.

[59] J.-P. Berenger, "A perfectly matched layer for the absorption of electromagnetic waves," *Journal of computational physics*, vol. 114, no. 2, pp. 185–200, 1994.

[60] S. Selleri, L. Vincetti, A. Cucinotta, and M. Zoboli, "Complex fem modal solver of optical waveguides with pml boundary conditions," *Optical and Quantum Electronics*, vol. 33, no. 4-5, pp. 359–371, 2001.

[61] H. Rogier and D. De Zutter, "Berenger and leaky modes in optical fibers terminated with a perfectly matched layer," *Journal of Lightwave Technology*, vol. 20, no. 7, pp. 1141–1148, 2002.

[62] MATLAB. Natick, Massachusetts: The MathWorks Inc.

[63] *Ansys HFSS simulator version 15.*

[64] D. Song and Y. Y. Lu, "Analyzing leaky waveguide modes by pseudospectral modal method," *IEEE Photonics Technology Letters*, vol. 27, no. 9, pp. 955–958, 2015.

[65] P. Bienstman, S. Selleri, L. Rosa, H. Uranus, W. Hopman, R. Costa, A. Melloni, L. Andreani, J. Hugonin, P. Lalanne, *et al.*, "Modelling leaky photonic wires: A mode solver comparison," *Optical and quantum electronics*, vol. 38, no. 9-11, pp. 731–759, 2006.

[66] C.-Y. Wang, H.-H. Liu, S.-Y. Chung, C.-H. Teng, C.-P. Chen, and H.-c. Chang, "High-accuracy waveguide leaky-mode analysis using a multidomain pseudospectral frequency-domain method incorporated with stretched coordinate pml," *Journal of Lightwave Technology*, vol. 31, no. 14, pp. 2347–2360, 2013.

[67] J. S. Hesthaven and T. Warburton, "High–order nodal discontinuous galerkin methods for the maxwell eigenvalue problem," *Philosophical Transactions of the Royal Society of London A: Mathematical, Physical and Engineering Sciences*, vol. 362, no. 1816, pp. 493–524, 2004.

[68] T. Warburton and M. Embree, "The role of the penalty in the local discontinuous galerkin method for maxwell's eigenvalue problem," *Computer methods in applied mechanics and engineering*, vol. 195, no. 25-28, pp. 3205–3223, 2006.

[69] P. Houston, I. Perugia, A. Schneebeli, and D. Schötzau, "Interior penalty method for the indefinite time-harmonic maxwell equations," *Numerische Mathematik*, vol. 100, no. 3, pp. 485–518, 2005.

[70] M. J. Grote, A. Schneebeli, and D. Schötzau, "Interior penalty discontinuous galerkin method for maxwell's equations: Energy norm error estimates," *Journal of Computational and Applied Mathematics*, vol. 204, no. 2, pp. 375–386, 2007.

[71] A. Buffa and I. Perugia, "Discontinuous galerkin approximation of the maxwell eigenproblem," *SIAM Journal on Numerical Analysis*, vol. 44, no. 5, pp. 2198–2226, 2006.

[72] M. El Bouajaji and S. Lanteri, "High order discontinuous galerkin method for the solution of 2d time-harmonic maxwell's equations," *Applied Mathematics and Computation*, vol. 219, no. 13, pp. 7241–7251, 2013.

[73] M. J. Grote, A. Schneebeli, and D. Schötzau, "Interior penalty discontinuous galerkin method for maxwell's equations: optimal l 2-norm error estimates," *IMA journal of numerical analysis*, vol. 28, no. 3, pp. 440–468, 2007.

[74] D. Sármány, M. A. Botchev, and J. J. van der Vegt, "Time-integration methods for finite element discretisations of the second-order maxwell equation," *Computers & Mathematics with Applications*, vol. 65, no. 3, pp. 528–543, 2013.

[75] B. Donderici and F. L. Teixeira, "Mixed finite-element time-domain method for transient maxwell equations in doubly dispersive media," *IEEE Transactions on Microwave Theory and Techniques*, vol. 56, no. 1, pp. 113–120, 2008.

[76] L. Fezoui, S. Lanteri, S. Lohrengel, and S. Piperno, "Convergence and stability of a discontinuous galerkin time-domain method for the 3d heterogeneous maxwell equations on unstructured meshes," *ESAIM: Mathematical Modelling and Numerical Analysis*, vol. 39, no. 6, pp. 1149–1176, 2005.

[77] D. Sármány, F. Izsák, and J. J. van der Vegt, "Optimal penalty parameters for symmetric discontinuous galerkin discretisations of the time-harmonic maxwell equations," *Journal of scientific computing*, vol. 44, no. 3, pp. 219–254, 2010.

[78] I. Perugia and D. Schötzau, "The -local discontinuous galerkin method for low-frequency time-harmonic maxwell equations," *Mathematics of Computation*, vol. 72, no. 243, pp. 1179–1214, 2003.

[79] H. Hernandez-Figueroa, F. Fernandez, and J. Davies, "Finite element approach for the modal analysis of open-boundary waveguides," *Electronics Letters*, vol. 30, no. 24, pp. 2031–2032, 1994.

[80] D. Song and Y. Y. Lu, "Pseudospectral modal method for computing optical waveguide modes," *Journal of Lightwave Technology*, vol. 32, no. 8, pp. 1624–1630, 2014.

[81] M. Lucido, C. Santomassimo, and G. Panariello, "The method of analytical preconditioning in the analysis of the propagation in dielectric waveguides with wedges," *Journal of Lightwave Technology*, vol. 36, no. 14, pp. 2925–2932, 2018.

[82] C.-C. Huang, "Numerical investigation of mode characteristics of nanoscale surface plasmon-polaritons using a pseudospectral scheme," *Optics Express*, vol. 18, no. 23, pp. 23711–23726, 2010.

[83] H.-H. Liu and H.-c. Chang, "High-resolution analysis of leaky modes in surface plasmon stripe waveguides," *Journal of Lightwave Technology*, vol. 34, no. 11, pp. 2752–2757, 2016.

[84] L. Chrostowski and M. Hochberg, *Silicon photonics design: from devices to systems*. Cambridge University Press, 2015.

[85] K. Okamoto, *Fundamentals of optical waveguides*. Academic press, 2006.

[86] A. Mekis, J. Chen, I. Kurland, S. Fan, P. R. Villeneuve, and J. Joannopoulos, "High transmission through sharp bends in photonic crystal waveguides," *Physical Review Letters*, vol. 77, no. 18, p. 3787, 1996.

[87] V. Rodríguez-Esquerre and H. Hernández-Figueroa, "Novel time-domain step-by-step scheme for integrated optical applications," *IEEE Photonics Technology Letters*, vol. 13, no. 4, pp. 311–313, 2001.

[88] J. W. Wallace and M. A. Jensen, "Analysis of optical waveguide structures by use of a combined finite-difference/finite-difference time-domain method," *JOSA A*, vol. 19, no. 3, pp. 610–619, 2002.

[89] S. Makino, T. Sato, Y. Ishizaka, T. Fujisawa, and K. Saitoh, "Three-dimensional finite-element time-domain beam propagation method and its application to 1-d photonic crystal-coupled resonator optical waveguide," *Journal of Lightwave Technology*, vol. 33, no. 18, pp. 3836–3842, 2015.

[90] A. Taflove, A. Oskooi, and S. G. Johnson, *Advances in FDTD computational electrodynamics: photonics and nanotechnology*. Artech House, 2013.

[91] W. K. Gwarek and M. Celuch-Marcysiak, "Wide-band s-parameter extraction from fd-td simulations for propagating and evanescent modes in inhomogeneous guides," *IEEE Transactions on Microwave Theory and Techniques*, vol. 51, no. 8, pp. 1920–1928, 2003.

[92] "Overlap in lumerical." https://kb.lumerical.com/en/ref_scripts_overlap.html.

[93] X. Wang, *Silicon photonic waveguide Bragg gratings*. PhD thesis, University of British Columbia, 2013.

Appendix A

Mode Propagation Simulations in Bragg Gratings on SOI

This appendix is a brief report of what was done during a Research Internship with the Nachos Team at the Inria *Sophia Antipolis - Méditerranée* Research Centre from June 2017 till December 2017. This work was developed in collaboration with Dr. Stéphane Lanteri, Dr. Jonathan Viquerat and Dr. Laurent Labonté.

The scope of this Internship was to be able to simulate conventional photonic grating structures with good accuracy. For this a Discontinuous Galerking Time Domain (DGTD) program (the Diogenes, developed by the Nachos team at Inria [7]) coupled to a Vectorial Finite Element Method Eigenmode Solver (the NPCGFEM, developed by Leandro) was employed. A set of new functionalities were proposed by the intern to be implemented in the Diogenes solver by the Diogenes Engineer (Jonathan Viquerat). Here, a brief description of how the simulations were performed and analyzed is presented. To perform the simulations many high performance computing techniques were used, and the main simulations were performed in the Inria cluster, the NEF.

A.1 Bragg gratings

A fundamental optical component adopted in photonic circuits is the Bragg grating. It comprises a waveguide structure with a given periodic perturbation that changes the effective index in a controlled manner. The perturbation is designed to build up a distributed interference pattern at a particular wavelength, the Bragg wavelength. These grating devices are a major focus of this Appendix. An interesting application of Bragg filters is presented in [17], where a novel sub-wavelength photonic SOI Bragg filter structure is proposed. The filter shows outstanding characteristics while ensuring relaxed fabrication constraints. The filters in [17] are implemented in 300 nm×220 nm strip waveguides, and the perturbations are in the order of 150 nm. These perturbations,

shown in the Fig. A.1 (figure from [17]), requires a single-etch process and are remarkably bigger when compared to conventional Bragg gratings [84], simplifying the fabrication considerably. The length of the reported filters ranges from 100 μm up to 1000 μm.

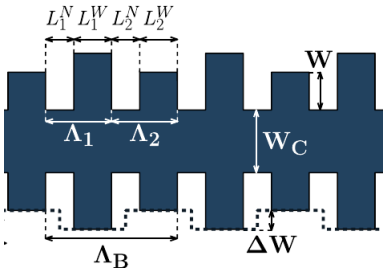

Figure A.1: Sub-wavelength grating.

The design of Bragg Gratings and other waveguide based devices in SOI platforms requires challenging 3D electromagnetic simulations due to its dimensions, high-index contrast and wavelength dependent characteristics. Specifically, for gratings the perturbations are intrinsically small when compared to the underlying waveguide dimensions, this hinders the structure numeric modeling since dense meshes are necessary. For instance, in the Fig. A.1 the gratings differential corrugation ΔW could be of only 5 nm. This small differential corrugation requires a refined mesh in the perturbation region, which implies in an extremely big computational problem.

A.2 Optical Waveguide Mode Analysis

A key step on the research reported here was the modal analysis of optical waveguides. For this the NPCGFEM described in the Section 2.2 of this dissertation was employed. The NPCGFEM code is object oriented and has several features related to mode analysis. It is possible to use linear, quadratic or cubic elements. And to take into account the open radiation boundary of optical waveguides the PML is also programmed and can be introduced in the domain. With this solver very precise eigenmode solutions can be calculated for arbitrary geometries and materials. This eigenmode solver at the time of the internship was validated in several scenarios and its results successfully match those ones from commercial solvers (CST, Lumerical, Comsol).

Additionally, the author of this document also developed a Coupled Mode Theory (CMT) framework linked with the NPCGFEM. The CMT is widely adopted by the optics community as a powerful analytical tool. This framework can be used to design and predict the behavior of conventional grating structures, for instance. For the sake of clarity and brevity, the CMT is not described here, details can be found in the reference [85].

A.2.1 Strip Waveguide

The results here presented are for gratings built on strip waveguides, and in this sub-section a brief description of its modal analysis is given. The NPCGFEM modal solver was used to calculate the modes of a Strip Waveguide (see sub-section 2.3.3) in which the silicon core has $W = 500\,\text{nm}$ and a height of 220 nm. The waveguide is embedded in a thick silica layer ($3\,\mu$m from the cladding until the underlying silicon layer). In this case, the silicon layer below the substrate can be neglected as its effects on the eigenmodes are negligible for the simulation purposes here. The PMLs were added to the outer borders of the domain and second order elements were used. A sample of a mesh used to calculate the modes is shown in the Fig. A.2. The refractive index of each material was fixed as $n_{Si} = 3.47$ and $n_{SiO_2} = 1.5$, since the simulations are performed for a narrow bandwidth around an air wavelength of $\lambda_0 = 1550\,\text{nm}$.

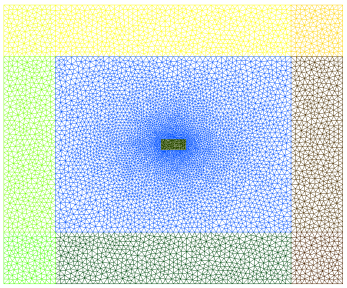

Figure A.2: Strip Waveguide mesh with PML elements for the eigenmode solver.

The calculated Quasi-TE mode solution fields distribution at 1550 nm are depicted in the Fig. A.3. The longitudinal fields were separated intentionally to enhance the difference with real TE and TM modes found in closed waveguides. And in the Fig. A.4 the mode effective index n_{eff} is shown. The effective index is directly obtained from the propagation constant: $n_{eff} = \beta/k_0$. For this bandwidth $\frac{dn_{eff}}{dw}$ is small and $\frac{d^2n_{eff}}{dw^2} \sim 0$.

A.3 Waveguide Mode Source

A major step to simulate photonic devices in a full wave 3D electromagnetic solver is to be able to propagate a given mode properly. In the literature there is a great discussion on options to perform mode propagation in photonic and microwave devices. The following works are highlighted: [86], [87], [88], [89], [90], [91].

Overall, a generic and reliable way to characterize waveguide based devices (either single-mode, higher-order mode, or multi-mode) is to excite the waveguide structure with a set of the desired eigenmode solutions (as in [87–91]). However, with an increased simulation domain and additional simulation steps it is also possible to evaluate the propagation of a given mode using point sources [86, 90]. Still, with an eigenmode-like source it is easier to guarantee a reliable analysis of the propagation characteristics.

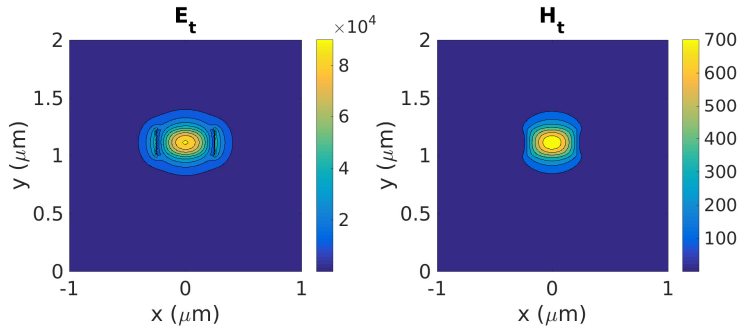

(a)

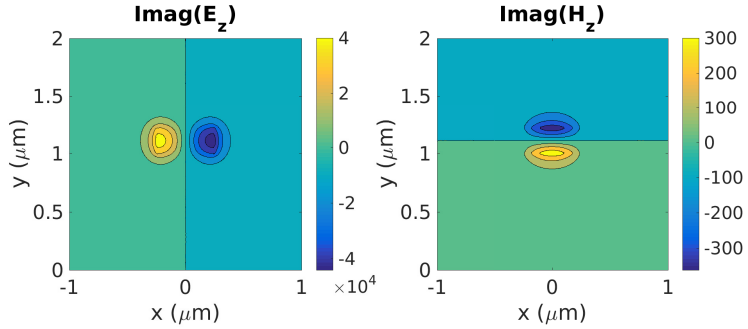

(b)

Figure A.3: Field distributions at $\lambda_0 = 1500\,\text{nm}$. (a) transverse fields, (b) longitudinal fields.

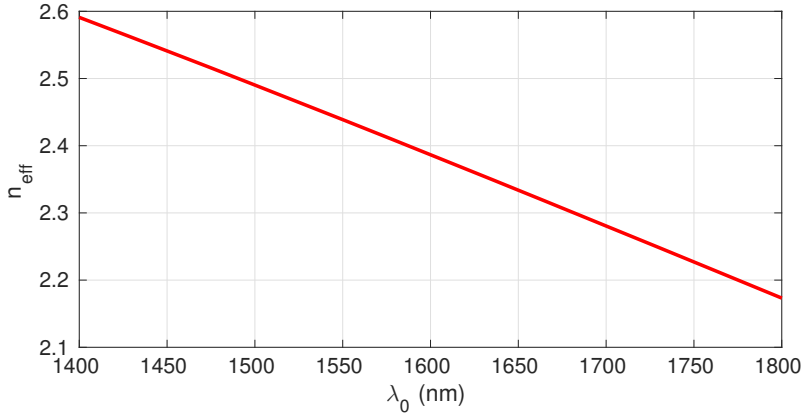

Figure A.4: n_{eff} dispersion.

In this work the excitation of photonic devices was based on eigenmode sources. The adopted eigenmode source scheme can be summarized in the following steps:

1. Impose the eigenmode solution in an unperturbed waveguide close to the device under simulation.

2. At the source region, the reflected wave from the device and the imposed mode source must be separated to compute the reflection coefficient.

3. At the output, after the mode propagate throughout the device, the fields are registered in an output face where any relevant observables can be computed.

4. With overlap integrals the mode content of interest can be separated both at the input source and at the output face.

The adopted method to excite modes in the aforementioned DGTD method is described below.

A.3.1 Time Domain Excitation: Gaussian Wave Packet

Independent of the method, when simulating a structure in the time-domain one can apply a pulse $p(t)$ (a Gaussian shaped pulse, for instance) function covering the frequency content of interest into the source. Then, the wavelength dependence characteristics in a limited bandwidth can be evaluated by means of the Fourier Transform. Hence, several time steps are required since the pulse must travel throughout the simulation domain. On the other hand, if a frequency domain solver is chosen, a number of 3D simulations are necessary to cover the desired spectrum.

First, an expression for a Gaussian Pulse for a given eigenmode solution needs to be defined. A single eigensolution of a given waveguide is fully defined by its field distribution and its propagation constant, both form the so-called mode solution. Then, consider an eigenmode field distribution ϕ, which is either the electric or magnetic field distribution and a frequency dependent propagation constant $\beta(w)$. Considering that the field distribution frequency-dependency is negligible (if the pulse is covering a sufficiently narrow bandwidth), one can apply a Fourier transform to obtain the time domain function $\Phi(t, x, y, z)$ of this Gaussian wave-packet covering a given frequency range of interest:

$$\Phi(t, x, y, z) = \frac{1}{\sqrt{2\pi\sigma^2}} \int_{-\infty}^{\infty} \phi(x, y) e^{-(\frac{w-w_0}{\sqrt{2}\sigma})^2} e^{-j\beta(w)z} e^{jwt} dw \tag{A.1}$$

w_0 is the center frequency of the Gaussian packet, $\frac{1}{\sqrt{2\pi\sigma^2}} e^{-(\frac{w-w_0}{\sqrt{2}\sigma})^2}$ is a Gaussian distribution. With $\Phi(t, x, y, z)$ the related eigenmode source can be imposed in the time domain simulation. For example, the Quasi-TE mode solution of the Strip Waveguide from Subsection A.2.1 could be used to generate both the electric and magnetic Gaussian wave-packet distributions in the time domain.

It is relevant to consider how much the intrinsic geometric dispersion ($\beta(w)$, as in the Fig. A.4) affects the Gaussian packet in the time domain. To analytically evaluate this a Taylor series expansion was used, with β in (A.1) being expanded centered at w_0 to

ease the process:

$$\beta(w) = \beta(w_0) + \frac{d\beta}{dw}|_{w_0}(w - w_0) + \frac{1}{2}\frac{d^2\beta}{d^2w}|_{w_0}(w - w_0)^2 + ... \tag{A.2}$$

By means of applying (A.2) until the second order term, the Fourier transform (A.1) is updated as:

$$\Phi(t, x, y, z) = \frac{1}{2\pi}\int_{-\infty}^{\infty} \phi(x, y) e^{-(\frac{w'}{\sqrt{2}\sigma})^2} e^{-jz[\beta(w_0) + \frac{d\beta}{dw}|_{w_0}(w') + \frac{1}{2}\frac{d^2\beta}{d^2w}|_{w_0}(w')^2]} e^{j(w'+w_0)t} dw' \tag{A.3}$$

$$w' = w - w_0 \tag{A.4}$$

If the Gaussian packet is covering a linear dispersion frequency range:

1. $\frac{d\beta}{dw}|_{w_0} \sim$ constant
2. $\frac{1}{2}\frac{d^2\beta}{d^2w}|_{w_0} \sim 0$

By analyzing the equation (A.3) for the linear dispersion case (low loss system can be considered too), it is clear that the dispersion will only add a constant phase term to the Gaussian packet. This is obviously due to the packet group velocity distribution, and in terms of simulation it shouldn't be a problem, since it will be taken into account directly as the packet propagates in a given waveguide. Therefore, as the wave packet propagates throughout the device in the 3D simulation, the eigenmode dispersion will be taken into account appropriately and the power spectrum at its input/output will be affected by the geometric dispersion of the device.

So, in the time domain method, when an eigenmode solution source is applied with a Gaussian pulse certain aspects should be considered [86–91]:

- Wideband excitation is not possible, since the eigenmodes are wavelength dependent.
- The Gaussian pulse bandwidth should be carefully chosen by analyzing the frequency/geometric dispersion of the waveguide. One way to do this is to check if the second derivative of the propagation constant $\frac{d^2\beta}{dw^2}$ is flat. The pulse should cover a spectrum with an almost flat $\frac{d^2\beta}{dw^2}$ region, since this means that its geometrical dispersion is roughly linear.
- For a not-too-large pulse bandwidth the mode geometric dispersion will inherently be taken into account in the 3D full wave simulation.
- The material dispersion should be taken into account equally in the eigenmode solver and in the 3D simulation.
- If present in the eigenspace of the device, some higher-order or radiative modes might be excited during propagation.

A.3.2 Diogenes mode source

In the context of the 3D simulation with the Diogenes DGTD solver, the mode excitation is performed with a Total-Field-Scattered-Field (TF/SF) interface [7]. With this interface a complete separation of the input and reflect waves at the source region can be achieved. Then, the calculation of the reflection coefficients becomes rather simple. On the other hand, to be able to perform generic simulations, an output face can be defined in the domain to perform transmission coefficients measurements. Finally, in order to be able to separate the input modal contents from other modes naturally excited in the simulation domain, it is recommended to use an overlap integral both at the source interface and the output face. The overlap operation is described in the following subsection.

The Fig. A.5(a) illustrates the simulation setup. In an unperturbed waveguide the Gaussian packet source is imposed, and after its propagation throughout a grating the transmission (and related observables) is measured at an output face also located in an output unperturbed waveguide. In the Fig. A.5(b) the shape of the Gaussian packet in time domain can be viewed. In this figure separated points register the field data in the time domain.

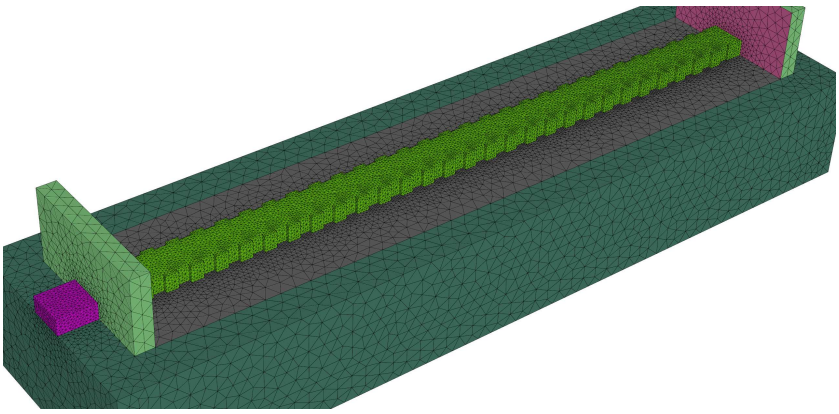

(a)

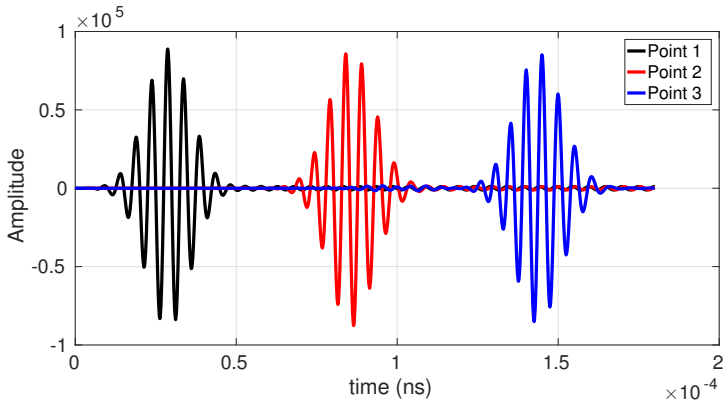

(b)

Figure A.5: (a) mode propagation simulation setup in a grating, (b) typical Gaussian wave-packets propagation.

Overlap for computing mode coefficients

As described above, several modes can arise in the 3D simulation. Hence, the separation of the input modal content is important to accurately characterize a given structure. In this work, the mode content separation is performed with overlap integrals, which under certain assumptions is a reasonable way to avoid the pollution of the observables spectrum. The overlap can be understood as a mode content measurement of a given field distribution in relation to a reference mode. It can be defined in different manners depending on the analysis context, here it is defined as [92]:

$$\text{overlap} = \Re\Big\{\frac{(\int_\Omega \vec{E}_1 \times \vec{H}_2 d\Omega)(\int_\Omega \vec{E}_2 \times \vec{H}_1 d\Omega)}{\int_\Omega \vec{E}_1 \times \vec{H}_1 d\Omega}\Big\} \frac{1}{\Re\Big\{\int_\Omega \vec{E}_2 \times \vec{H}_2 d\Omega\Big\}} \tag{A.5}$$

where Ω is the 2D domain where a calculated field distribution is being compared to a known mode distribution, the pairs (E_1, H_1) and (E_2, H_2) are the fields distributions of either the known mode or the calculated field distribution.

Simulation time

The time required for the pulse propagation in a waveguide can be calculated from the β dispersion relationship. Then, a good estimative for the total simulation time in a grating can be obtained. In the Fig. A.6 an example of the time of a pulse propagation which covers the spectrum between 150 THz and 250 THz is shown.

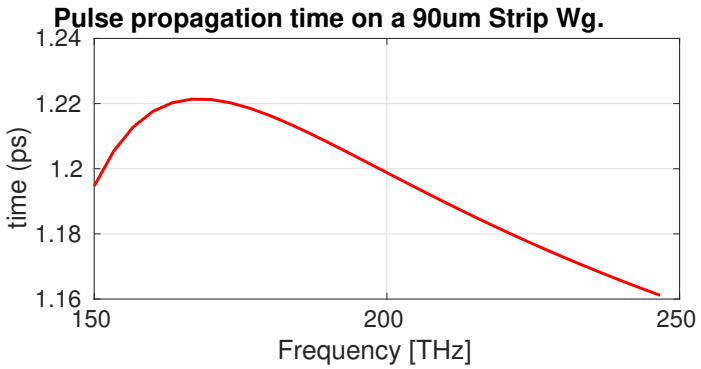

Figure A.6: Propagation time from group velocity.

A.4 Grating Model

To perform the grating simulations the intern designed a parameterized computation model of gratings. This fully parameterized model of a generic purpose grating device in Strip Waveguides was built with the Gmsh software [53] with its novel CAD tool. In the Fig. A.7 this model is depicted. The model includes PML and the aforementioned

TF/SF regions. This model enables the simulation of asymmetric gratings of any kind. The source interface and output face are located before and after the grating structures, respectively, on unperturbed waveguides. The Gmsh also is used to build the mesh from the grating model. In the Fig. A.8 the mesh of a small length grating is shown in different perspectives, including a detailed view of the silicon core region. If necessary, adiabatic transitions can be included in the model.

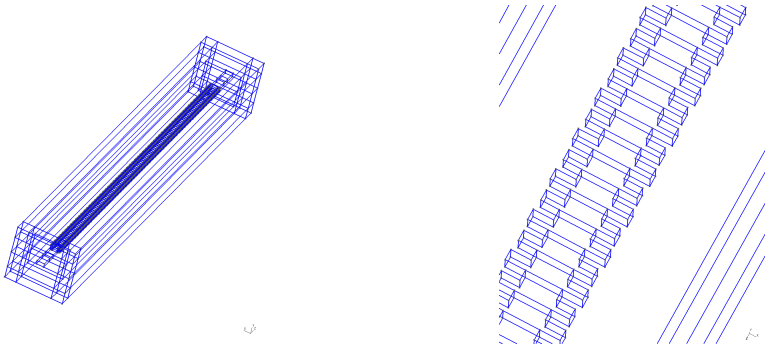

(a) (b)

Figure A.7: Grating 3D model. (a) full model, (b) zoom at grating region.

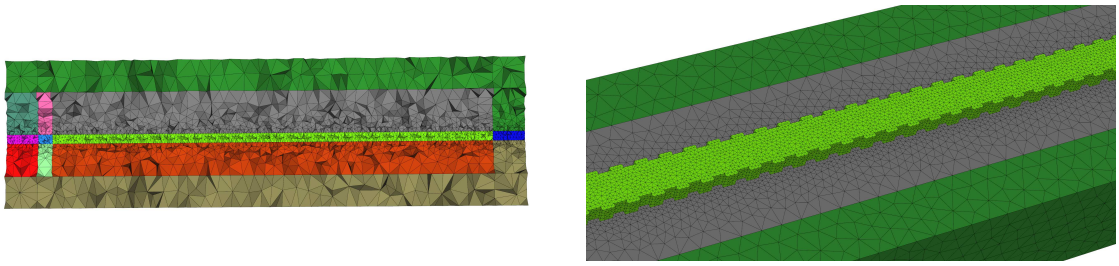

(a) (b)

Figure A.8: Grating model mesh. (a) full model, (b) zoom at silicon core region.

A.5 Simulations

With the eigenmode source described in Section A.3, incorporated into the Diogenes DGTD solver, it became possible to simulate photonic waveguides-based devices. The NPCGFEM mode solver from Section A.2 outputs a set of formatted files to be directly send to the Diogenes solver source. Throughout the internship a huge set of testing runs were necessary to validate the mode source and observables calculation with the overlap integral. Nonetheless, some relevant simulations were performed to show that it is possible to simulate gratings with the Diogenes solver coupled to the NPCGFEM solver. In this section only the physically relevant results are presented.

The intern was also responsible for the gratings design. For this, the CMT was employed. The developed NPCGFEM solver has a framework to design periodic structures with the CMT, which eases the process. In this work, all of the simulated gratings were designed to reflect the Quasi-TE mode around 1550 nm. They were built on a strip waveguide with simple rectangular corrugations of width ΔW, a fixed period of Λ and a number of periods N. The general geometry is depicted in the Fig. A.9 (figure from [93]). In all simulations the strip waveguide has $W = 500$ nm and a height of 220 nm, and it is embedded in a SiO_2 layer of 2 μm. The underlying silicon layer was neglected in the present analysis. The Quasi-TE mode solution for this waveguide is presented in Subsection A.2.1.

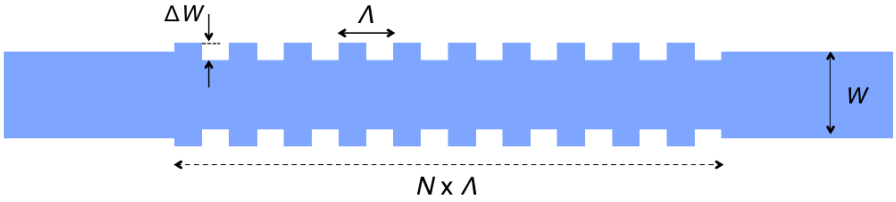

Figure A.9: General grating structure.

The main simulation results are presented for two gratings with the following parameters:

1. $\Delta W = 50$ nm, $\Lambda = 324$ nm, $N = 28$;
2. $\Delta W = 50$ nm, $\Lambda = 324$ nm, $N = 280$;

It is important to state that at the moment very big gratings simulations are troublesome since both the mesh is huge and the number of time steps is enormous to perform the full pulse propagation. The total simulation time is defined by the dimensions of the device and also by the pulse size (how large or narrow is the Gaussian bandwidth). Additionally, the time step size is bounded by the mesh sizes in the DGTD solver, the more the mesh is refined the smaller the time step will be. Furthermore, the of higher order elements can also be used to decrease the time step.

A.5.1 Grating 1: $\Delta W = 50$ nm, $\Lambda = 324$ nm, $N = 28$

Although this grating has a small length, its Bragg effect is explicit due to the large corrugation. The results presented in this subsection includes the overlap at the source interface, which is the setup explained at the section Subsection A.3.

The results for this grating are presented in comparison with the CST commercial solver and the CMT. The results are presented in the Fig. A.10.

Apart from a minor frequency shift, the level and shape of the curves from the Diogenes+NPCGFEM (called Diogenes+VecEigFEM in the figures) solver are quite similar to the CST and CMT, which indicates a reliable simulation. The frequency shift between

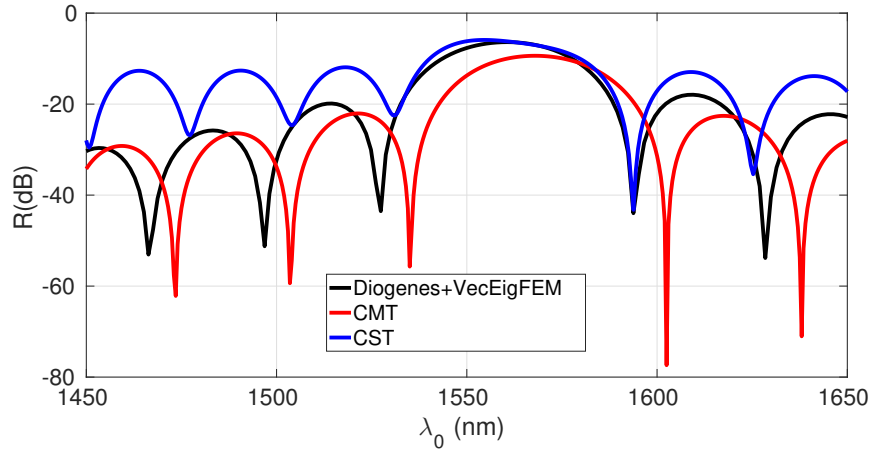

(a)

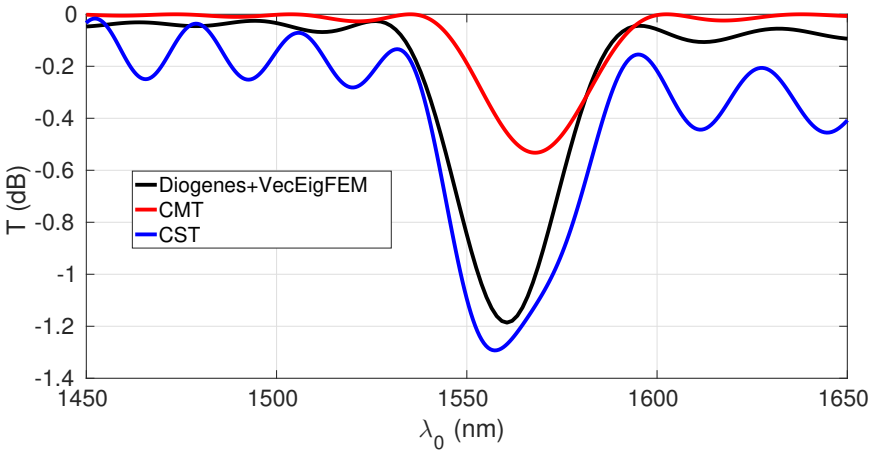

(b)

Figure A.10: Grating 1 comparison between the present method, the CST commercial solver, and the Coupled Mode Theory analysis . (a) reflectivity, (b) transmission.

the CMT and the other methods is expected since this is an analytical approach that does not account for the radiative modes as in a 3D simulation. The radiative modes losses are responsible for the huge difference in the transmission spectrum between the CMT and the other 3D simulations.

When compared to the CST simulation, the solution around the Bragg wavelength is remarkably similar, and supposedly accurate. However, for wavelengths more distant to the resonance a significant difference can be seen. The CST solver is employing a wide bandwidth excitation, so probably the reflection solution at the borders of the wavelength range analyzed includes other modes contribution. Instead, with the proposed Diogenes+NPCGFEM simulation setup the dominant Quasi-TE mode is evaluated completely separated due to the overlap integral.

In the Fig. A.11 two plots with the E_x field distribution are shown in the time domain and in the frequency domain. The fields are shown in a cut inside the waveguide

at the grating region. The wavelength in the frequency domain plot is of 1553 nm, which is the Bragg wavelength.

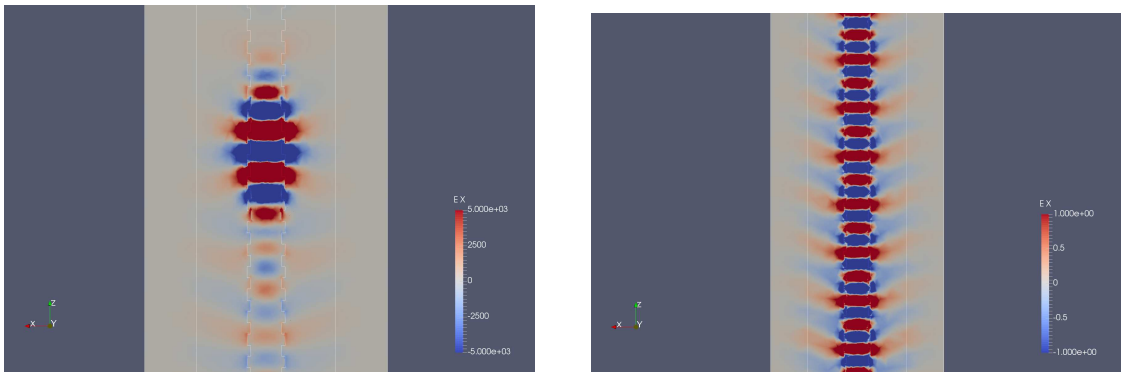

(a) (b)

Figure A.11: E_x field plots at the Grating 1. (a) time domain, (b) frequency domain ($\lambda_0 = 1553\,\text{nm}$).

A.5.2 Grating 2: $\Delta W = 50\,\text{nm}$, $\Lambda = 324\,\text{nm}$, $N = 280$

The last result to be presented is a set of simulations on a large grating, which is a physically relevant and could actually be used in practical applications, since a high reflectivity is achieved. The same 50 nm corrugation is used, however with 280 periods.

This grating was simulated in a coarse mesh, due to its enormous sizes. In the Fig. A.12 the grating characteristics are presented again in comparison with the CST and the CMT. The CST solution here presented was performed with dispersive silicon materials. Therefore a huge wavelength shift can be seen. But, as seen in the figures it seems that the bandwidth of the device is well captured with the Diogenes+NPCGFEM simulation scheme.

Again, the shift in the CMT is quite reasonable and expected, along with its lower rejection level at the Bragg wavelength. Nonetheless, the Diogenes simulation here is using a poor mesh.

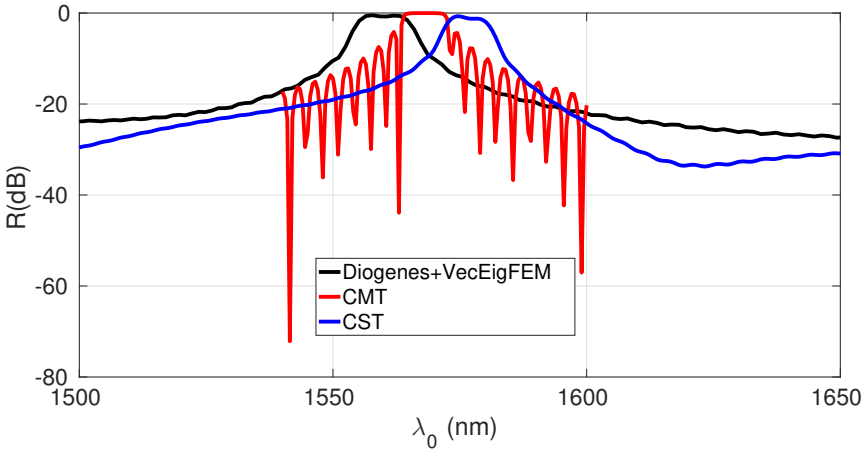

(a)

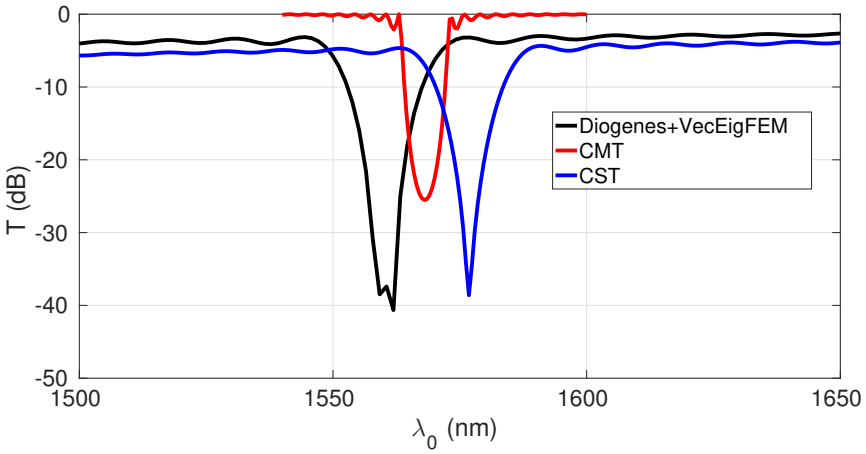

(b)

Figure A.12: Grating 2 comparison between the present method, the CST commercial solver, and the Coupled Mode Theory analysis . (a) reflectivity, (b) transmission.